PNNL-17134

Pacific Northwest National Laboratory
Operated by Battelle for the U.S. Department of Energy

Geotechnical, Hydrogeologic, and Vegetation Data Package for 200-UW-1 Waste Site Engineered Surface Barrier Design

A.L. Ward

November 2007

Prepared for the U.S. Department of Energy
under Contract DE-AC05-76RL01830

DISCLAIMER

PACIFIC NORTHWEST NATIONAL LABORATORY
operated by
BATTELLE
for the
UNITED STATES DEPARTMENT OF ENERGY
under Contract DE-ACO5-76RL01830

Printed in the United States of America

Available to DOE and DOE contractors from the
Office of Scientific and Technical Information,
P.O. Box 62, Oak Ridge, TN 37831-0062;
ph: (865) 576-8401
fax: (865) 576 5728
email: reports@adonis.osti.gov

Available to the public from the National Technical Information Service,
U.S. Department of Commerce, 5285 Port Royal Rd., Springfield, VA 22161
ph: (800) 553-6847
fax: (703) 605-6900
email: orders@nits.fedworld.gov
online ordering: http://www.ntis.gov/ordering.htm


This document was printed on recycled paper.
(8/00)

PNNL-17134

Geotechnical, Hydrogeologic and Vegetation Data Package for 200-UW-1 Waste Site Engineered Surface Barrier Design

A. L. Ward

November 2007

Prepared for
the U.S. Department of Energy
under Contract DE-AC05-76RL01830

Pacific Northwest National Laboratory
Richland, Washington 99352

Summary

Fluor Hanford (FH) is designing and assessing the performance of engineered barriers for final closure of U-plant waste sites. The ideal barrier will minimize recharge and plant intrusion into the underlying waste, thereby providing protection for human health and the environment. FH is using the Pacific Northwest National Laboratory (PNNL) Subsurface Transport over Multiple Phases (STOMP) simulator as the primary design optimization tool for simulating surface barrier performance. PNNL is supporting FH barrier design activities. One of PNNL's responsibilities is to provide parameter values for the geotechnical, physical, hydraulic, and thermal properties of the materials comprising the barrier and the structural fill on which it will be constructed as well as parameters to allow simulation of plant effects. This report provides the required data package as well as the technical basis, rationale, and methodology used to obtain the parameter values.

Best-estimate values for the hydraulic parameters of the soil and geotechnical materials to be used in the performance assessment analyses of the candidate barriers were developed. Hydraulic properties were directly measured for the Environmental Restoration and Disposal Facility spoil pile soils and the silt loam borrow-source soils. Hydraulic properties for the admixture of silt loam and pea gravel and for the silt admixture and quarry spalls were estimated by adjusting the silt-loam parameters for amount of the coarse material. Geotextile hydraulic properties, which were compiled from data reported in the literature. However, properties of the biointrusion layer were derived from the specified particle-size distribution. A summary of Brooks-Corey and van Genuchten parameters along with saturated hydraulic conductivity are presented for each material.

Thermal properties also play a critical role in the water and energy balance. These properties were estimated using pedotransfer functions that take into account the mineralogy and water-retention relationships for the porous materials. Predicted properties compared well with literature values, but were generally higher than those reported for Hanford sediments.

Plants play an important role in the function of engineered barriers, and accounting for the effects of plants on barrier performance requires a variety of input parameters. Owing to the number of species that may be used to revegetate engineered barriers, plant parameters were grouped on the basis of plant growth forms, e.g., forbs, grasses, and shrubs. Parameters are provided to allow an evaluation of the effects of canopy structure and color, rooting depth, and growth cycle on energy and water balance and ultimately barrier performance.

Acronyms

ASTM	American Society of Testing and Materials
CASTNET	Clean Air Status and Trends Network
DAAC	Distributed Active Archive Center (Oak Ridge National Laboratory)
DBS	Daniel B. Stevens and Associates Incorporated
DOY	day of year
EPA	U.S. Environmental Protection Agency
ERDF	Environmental Restoration and Disposal Facility
FEIS	Fire Effects Information Service
FH	Fluor Hanford
FLTF	Field Lysimeter Test Facility
GEO	GeoEngineers
ILAW	immobilized low-activity waste
MAP	mean annual precipitation
MSD	measured settled density
PET	mean annual evapotranspiration
PNNL	Pacific Northwest National Laboratory
STOMP	Subsurface Transport Over Multiple Phases
SW	Shannon and Wilson, Inc.
USCS	United Soil Classification System
USDA	U.S. Department of Agriculture
WAE-B	Water-Air-Energy w/Barrier Module
WDOT	Washington State Department of Transportation

Contents

Figures

Tables

1.0 Introduction

Fluor Hanford (FH) is assessing the performance of candidate engineered barriers for final closure of Hanford's U-plant waste sites. These barriers are intended to meet a reasonable expectation that subsurface waste is protected from the general public, surface and groundwater resources, air resources, and inadvertent intruders. FH is using the Pacific Northwest National Laboratory (PNNL)-developed Subsurface Transport Over Multiple Phases (STOMP) simulator as the primary design optimization tool for assessing surface barrier performance and for identifying the most robust design. PNNL is providing technical support to FH in barrier-design activities, particularly in the application of the STOMP code. The applicable operation mode of STOMP is the barrier extension of the water-air-energy (WAE-B) of the simulator. This operational mode accounts for non-isothermal, multi-fluid, subsurface flow and transport processes. These processes are fully coupled to a modified nonlinear sparse-vegetation evapotranspiration module to mechanistically predict the components of the water balance, including evaporation, transpiration, storage, drainage, and surface runoff. A brief overview of these processes and how they may impact barrier performance is provided below.

The hydrologic performance of engineered barriers is influenced by several interactive and dynamic processes that control the near-surface dynamics of mass and energy and ultimately the water balance of the system (Ward and Gee 1997). The physical system is best conceptualized as a soil-vegetation-atmosphere continuum in which the flow of mass and energy is multidimensional. Water impacting the surface can evaporate from soil and plant surfaces, be routed over the surface as runoff, or enter the soil as infiltration. Infiltrating water is stored in the fine-soil layer until it is removed by evaporation or plant uptake, or it can redistribute deeper into the profile (Ward and Gee 1997). In a well-designed surface barrier, the amount of water exiting the barrier layers can be quite small (Ward et al. 2005b,c,d). Water that does not run off the surface is not recycled to the atmosphere by evapotranspiration or is not diverted by lateral drainage enters the barrier and may begin to percolate. At high enough rates, percolation may mobilize contaminants in the underlying native sediments, transporting these contaminants to groundwater. Predicting the hydrologic performance of engineered barriers therefore requires consideration for variably saturated flow processes, including runoff, water storage, evaporation, transpiration, lateral diversion along sloped layers, and, ultimately, deep percolation through a multilayered system in response to meteorological forcings.

Figure 1.1 shows a schematic cross section of a mono-fill barrier proposed for closure of 216-U-1/2 and 216-U-8 at the 60% complete stage. This design includes a surface admixture layer of silt loam and pea gravel underlain by a layer of silt loam of comparable thickness. Although not shown in Figure 1.1, the proposed design also includes a bio-barrier layer intended to mitigate the penetration of roots and burrowing animals into the native sediment and underlying wastes. This layer, which is composed of coarse rock, is overlain by a graded filter to minimize migration of the finer textured compacted grading fill into the coarse rock. Owing to the proximity of contamination to the soil surface, the cover will be constructed above grade. As a result, the design includes a protective side slope (Figure 1.1). The side slope is designed on the basis of a rock-supported binary mixture of sediments. In this design, fine-grained sediment will occupy the voids created by a rock matrix, thereby increasing the water-storage capacity above that of the typical rock slope. This design will also serve to create a favorable rooting environment for vegetation. In this design, the rock matrix is composed of quarry spalls whereas the fine-textured component is comprised of silt loam.

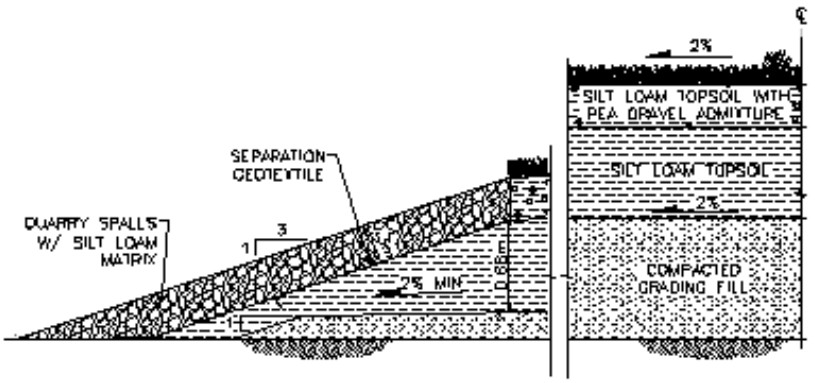

Figure 1.1. Schematic of Mono-fill U-Plant Surface Barrier Cross Section Showing Layering Detail

Successful performance of the barrier requires that all the winter precipitation be stored in the upper soil layers until it can be recycled to the atmosphere by evaporation from soil and plant surfaces and by transpiration from vegetated surfaces. All of the layers comprising the barrier, except for the bio-barrier, are designed with a 2-percent slope to promote lateral movement of water towards the edges of the barrier. Infiltration and redistribution of water in the barrier is a multiphase flow and heat transport problem that occurs in response to forcing meteorology. The forcing meteorology causes spatiotemporal changes in solar radiation, precipitation, air temperature, relative humidity, wind speed, and barometric pressure, all of which affect barrier performance. The sparse vegetation evapotranspiration operational mode of STOMP, STOMP-WAE-B, is used to simulate this system with two options for describing the surface boundary: 1) bare surface, and 2) single-plant temperature (Ward et al. 2005d; White and Ward 2005).

The bare-surface option considers water, air, and thermal energy exchange between the atmosphere and subsurface without plants on the surface. In this mode, conservation equations for water mass, air mass, and thermal energy are solved at the ground surface. The air-mass conservation equation is implicit, yielding a two-equation system for water mass and thermal energy. The single-plant-temperature option considers water, air, and thermal energy exchange between the atmosphere and subsurface, assuming a single temperature on leaf surfaces within the plant canopy and a single water-vapor density within the canopy. This option requires the solution of five coupled nonlinear equations including water mass and thermal energy at the ground surface, thermal energy at leaf surfaces, and water mass and thermal energy within the canopy (White and Ward 2005; Ward et al. 2005d). The multiple-plant-temperature option considers water, air, and thermal energy exchange between the atmosphere and subsurface, assuming a unique temperature within the canopy, and a unique water-vapor density within the canopy of each plant species. This option requires the solution of coupled nonlinear equations for water mass and thermal energy at the ground surface, thermal energy at the plant leaves for each plant species, and water mass and thermal energy at the canopy for each plant species. Consequently, simulating biotic and hydrological responses to natural climatic variation requires solution of the coupled equations.

Solving the coupled equations requires specification of parameter values for the different plant species as well as physical, hydraulic, and thermal properties of the natural and geotechnical materials comprising

the barrier and its immediate surroundings. However, not all of the required input parameters are readily available for the site of interest, resulting in a need to estimate these parameters from available data. One of PNNL's responsibilities in the design process was to provide a data package of parameter values for the physical, hydraulic, and thermal properties of the materials comprising the barrier and the structural fill on which it would be constructed. A number of laboratory and field methods have been developed to determine hydraulic properties, but none of these methods perform well over the wide range of conditions or sediment types typical of heterogeneous deposits at the typical waste management sites. As a result, researchers have sought methods to estimate the required properties from readily available or easily obtained data using pedotransfer functions (Arya and Paris 1981; Rawls et al. 1992; Schaap et al. 1997; Mbonimpa et al. 2002). A similar problem exists for thermal properties, and this is compounded by a general lack of thermal property data for most of the materials of interest. Nevertheless, pedotransfer functions for thermal properties, based on physical, mineralogical, and hydraulic properties, have also been developed (Johansen 1975; Farouki 1981; Fredlund 1999).

The pedotranfer-function approach was adopted for estimating parameters for materials and sediments for which no data were available and those on which no laboratory measurements were made. These properties are expressed as parameters of the constitutive models used in STOMP-WAE. In addition to the best-estimate parameter values for geologic and geotechnical materials, the data package also includes parameter values used to describe the phenology, morphology, and physiological characteristics of the native plants expected to be used to vegetate the barriers. These data are the subject of this report. This report provides the technical basis, rationale, and methodology used to obtain the estimated and measured parameter values as well as the required data package.

1.1 Scope and Objectives

The scope of this work was to provide expert knowledge and guidance on the application of STOMP-WAE-B to barrier design, particularly the identification and interpretation of sources of input parameters, and the development of a matrix of input variables to allow assessment of sensitivities and to optimize hydraulic performance. The specific objective was to obtain defensible estimates of parameter values and inputs including physical, hydraulic, and thermal properties for natural and synthetic porous materials as well as plant properties. These parameters are needed for input to the STOMP simulator (Ward et al. 2005a,d).

Required physical properties include particle density, bulk density, grain-size distribution, and compaction characteristics. The required hydraulic properties include porosity, soil water-retention characteristics, and the saturated and unsaturated hydraulic conductivities. Required thermal properties include the saturation-dependent thermal conductivity and specific heat capacity. Estimates of the hydraulic and thermal properties are required for at least two different compaction densities. Data are required for the silt loam soil and sandy soils from the borrow source areas and the geotechnical materials to be used in construction to derive the information necessary for geotechnical calculations and model parameterization. Required plant properties include the parameters needed to describe the morphology and physiology of the native plant species to be used in vegetating the engineered cover. For hydraulic and thermal characterization, our analyses focused on two sites, 1) a sub-area of the silt-loam borrow source for use in construction of the fine soil layer and 2) the Environmental Restoration and Disposal Facility (ERDF) spoil pile to be used as a structural fill. In the specification of the plant parameters, a plant composition similar to that used on the prototype Hanford barrier at the 200-BP-1 site was assumed.

This report presents a summary of the data collection and parameterization methods used, including literature reviews for those parameters that were not measured, methods of analysis and interpretation for those that were measured, and the translation of these data into input parameters for Version 2.0 of the sparse vegetation evapotranspiration model of STOMP-WAE-B. In an earlier report, Ward et al. (2005) published a hydrology and vegetation data package based on the requirements of the Version 1.0 of the sparse vegetation evapotranspiration model for the water-air-energy operational mode of STOMP.

2.0 Required Properties and Parameters

This section provides a brief description of the properties and parameters required to simulate non-isothermal unsaturated flow with plant water uptake using the STOMP-WAE-B operational mode. The required parameters were obtained from 1) literature reviews, 2) measurement, or 3) estimation by pedotransfer functions using available data or using a combination of these methods. In some cases, particularly in the estimation of soil thermal properties, we relied solely on the use of pedotransfer functions to assist in parameter estimation. In the following sections, we describe the methods used to obtain the various parameter sets for the porous materials and plant species.

2.1 Particle-Size Distributions

Particle-size distribution is not a direct input into the STOMP simulator but is used to estimate important input parameters based on the soil composition. Particle-size distribution and gradation are known to influence not only the hydraulic properties of soils and sediments, but also the engineering properties. Particle-size distributions can be used to estimate hydraulic and thermal properties by applying pedotransfer functions. Size distributions and the related coefficients, e.g., coefficient of uniformity, C_u, and coefficient of curvature, C_c, are used help in the classification of soils and in engineering design. For example, the design of graded filters used to minimize the migration of fines with multilayered barriers and to protect foundation soils from seepage-induced piping failure relies on the d_{85} and d_{15} values of the gradation curve. Here, d_{85} and d_{15} are the diameters at which 85% and 15% of the sample weight is smaller than the corresponding diameters read on the x-axis of the particle-size distribution curve.

Particle-size distributions of the ERDF samples were determined using the wet-sieve technique described in PNL-MA-567, procedure SA-2. For each sample, a subsample was placed on a set of sieves corresponding to the U.S. Department of Agriculture (USDA) sand classification system (see PNL-MA-567, procedure SA-3). The smallest sieve was the 270 sieve, with a mesh opening of 0.053 mm. For particles passing the number 10 (2-mm) sieve, hydrometer analysis was performed in accordance with American Society of Testing and Materials (ASTM) 422-63 (ASTM 1985) and Gee and Bauder (1986).

Sample-size fractions by weight were converted into size-fraction percent by weight, and the percent by weight, passing each sieve plotted as a curve on a semi-logarithmic scale to describe the size distribution. The resulting data represent the percentage of particles retained and passing through each sieve. The percentage of each size fraction was used to determine texture according to the USDA classification and the Unified Soil Classification System (USCS) specified by ASTM D 2487 (ASTM 2000). Grain-size statistics were calculated from the grain-size distributions using the methods described by Folk (1980).

Since grain-size diameters typically span many orders of magnitude for natural sediments, a convenient way to describe wide-ranging data sets and simplify the computation of grain-size statistics is the ϕ (phi) scale. Logarithmic ϕ values (in base two) are calculated from particle diameters in millimeters as follows:

$$\phi = -\log_2 d = -\left(\frac{\log_{10} d}{\log_{10} 2}\right) \tag{2.1}$$

where:

ϕ = particle size in ϕ units

d = diameter of particle in mm.

Gradation coefficients are typically calculated using the ϕ transformation but in these can be converted to units of mm by d (mm) = $2^{-\phi}$.

2.1.1 Mean Diameter

The mean diameter is identical to the graphic mean reported by Folk (1980) and is calculated with the following equation:

$$M_z = \frac{\phi_{16} + \phi_{50} + \phi_{84}}{3} \tag{2.2}$$

This statistic has been shown to correspond very closely with the mean derived from the method of moments and is useful for describing the effects of texture on hydraulic properties. In general, hydraulic conductivity increases with increasing mean diameter whereas the water-holding capacity and bubbling pressure decrease with increasing mean diameter.

2.1.2 Sorting Index

The sorting index is inferred from the inclusive graphic standard deviation. σ_I is the best measure of grain sorting and is computed as

$$\sigma_I = \frac{\phi_{84} - \phi_{16}}{4} + \frac{\phi_{95} - \phi_5}{6.6} \tag{2.3}$$

Because the standard deviation is the measure of the spread in phi (ϕ) units of the sample, the symbol ϕ must always be attached to the value for σ_I. An analysis of sorting values for a large number of sediments suggests the following classification scheme for sorting:

$\sigma_I < 0.35\phi$	very well sorted
$0.35\phi - 0.50\phi$	well sorted
$0.50\phi - 0.71\phi$	moderately well sorted
$0.71\phi - 1.0\phi$	moderately sorted
$1.0\phi - 2.0\phi$	poorly sorted
$2.0\phi - 4.0\phi$	very poorly sorted
$> 4.0\phi$	extremely poorly sorted.

The best sorting attained in natural sediments is about 0.20ϕ to 0.25ϕ. The most poorly sorted are sediments like glacial tills and mudflows, which tend to have σ_I values between 5ϕ and 8ϕ and may reach as high as 10ϕ. The sorting index is critical in describing the effects of texture on hydraulic properties. Although hydraulic conductivity increases with increasing mean diameter, increasing the sorting index can result in a decrease in hydraulic conductivity. Similarly, the expected decreases in water-holding

capacity and bubbling pressure with increasing mean diameter can be offset by increases in the sorting index.

2.1.3 Coefficient of Uniformity

The coefficient of uniformity, C_u, is a non-statistical measure of the size range of the particle-size distribution and is equivalent to the slope of the gradation curve. It is similar to the standard deviation of a distribution but is typically used for samples whose size distribution is not normally distributed. This parameter is calculated as

$$C_u = \frac{d_{60}}{d_{10}} \tag{2.4}$$

The terms d_{60} and d_{10} in Eq. (2.4) represent the grain diameter in mm indicated by the gradation curve at the 60 and 10% levels, respectively. For example, d_{60} means that 60% of the sample weight is smaller than the appropriate particle size read on the x-axis of the particle-size distribution curve. The larger the value of C_u, the larger the range of particle-size classes. A C_u of 1 is indicative of a uniform soil in which all grains are the same size (e.g., dune sand). For most natural soils, uniform samples typically show a C_u less than 2. On the other extreme is the glacial till, for which the C_u can reach 30. For gravels, the value of C_u separating well graded from poorly graded distributions is 4. A $C_u < 4$ is indicative of a poor gradation whereas $C_u > 4$ is well graded, provided the gradation curve is monotonic and relatively symmetrical. For sands, the value of C_u separating well graded from poorly graded distributions is 6. A $C_u > 6$ is indicative of a well graded sand whereas a $C_u < 6$ is poorly graded.

2.1.4 Coefficient of Curvature

The coefficient of curvature, C_c, is a non-statistical measure of the *shape* and symmetry of a given particle-size distribution curve. It is sometimes referred to as the coefficient of gradation and is often used to confirm conclusions about the gradation inferred from the C_u. This parameter is calculated as

$$C_c = \frac{(d_{30})^2}{d_{10} \cdot d_{60}} \tag{2.5}$$

The term d_{30} in the equation represents the grain diameter in mm, indicated by the gradation curve at the 30% level. Both sands and gravels are considered to be well graded if C_c is between 1 and 3. For sands, C_u must be greater than 6 whereas it must be greater than 4 for gravels. In borderline cases where there may be conflicting interpretations from C_u and C_c, the values of C_u generally take precedence.

2.2 Particle Density

Particle density, ρ_s, is widely used for establishing the density-volume relationship of soil materials. It is used in the calculation of porosity and in estimating optimum moisture in compaction tests. Particle density is defined as the mass of solids in a sample divided by the volume of the solids. Particle density is commonly assumed to be 2.65 Mg/m^3, which corresponds to the specific gravity of quartz. However, many silicate and nonsilicate minerals such as feldspars, granites, micas, and kaolinite exhibit densities between 2.3 and 3.0 whereas the density of iron-containing minerals like hematite and goethite often exceeds 3.3. The particle of a soil therefore depends on the mineral composition and is calculated using a

weighted mean. For example, the mean particle density of a soil composed of three minerals with weight fractions x_1, x_2, and x_3 may be calculated as:

$$\rho_s = \left(\frac{x_1}{\rho_{s_1}} + \frac{x_2}{\rho_{s_2}} + \frac{x_3}{\rho_{s_3}} \right)^{-1} \tag{2.6}$$

The size fraction less than 2 mm is typically used to measure particle density (Blake and Hartge 1986a). For ρ_s determinations, the particle-density test was performed on three replicate samples using the pycnometer method (Blake and Hartge 1986b; ASTM 2002).

2.3 Bulk Density

Dry bulk density, ρ_b, is also used to establish the density-volume relationship of soil materials. It is typically used to calculate porosity and estimate optimum moisture in compaction tests. Dry bulk density is defined as the mass of solids in a sample divided by the total (bulk) volume of the dry sample. The total volume includes the volume occupied by the solids and air. Wet bulk density includes the volume occupied by the solids, water (or other liquid), and air. The choice of bulk-density measurement often depends on the nature of the sample. Dry and wet bulk density measurements were made using the method described by Blake and Hartge (1986b).

Soil compaction is important for predicting porosity, permeability, and stability attributes. Compactability depends on both intrinsic and transient properties like texture and soil moisture. In general, the higher the degree of compaction, the higher will be the shear strength and the lower the compressibility. The degree of compaction of a soil is measured in terms of the dry density, which varies with the water content and compactive effort. The Procter test is used widely to characterize soil compactability and was used in this study. For this test, laboratory-compaction curves were developed and the maximum dry density, ρ_{bmax}, values interpolated using the SoilVision® software. The Procter test was performed according to D698-00, the ASTM method for the laboratory compaction characteristics of soil using the standard effort.

2.4 Porosity

Porosity (ϕ) is the volume of voids in a sample (the air- and liquid-filled volume) divided by the total volume of the sample. The porosity can be measured directly (Danielson and Sutherland, 1986). However, it is typically calculated using measured values of particle and dry bulk densities according to

$$\phi = 1 - \rho_b / \rho_s \tag{2.7}$$

The particle density is generally time invariant, so any changes in the porosity are typically due to changes in ρ_b.

2.5 Water Retention

Water retention refers to the retention of water by porous materials at various matric potentials. Water-retention measurements were made on select samples using a combination of hanging water column,

pressure-plate extraction, and vapor equilibrium methods. These procedures conform to ASTM (1985) standards (D6836-02, D 2325). The hanging-water-column measurement was used to obtain retention data for pressures between 0 and 100 mbar according to ASTM D6836-02. The pressure-plate extraction method was used to obtain retention data at pressures over 100 mbar according to ASTM D2325-68 (ASTM 2000), an approach consistent with Klute (1986). The vapor equilibrium method was used to obtain the water retention around $2.5 \cdot 10^6$ cm of suction according to ASTM D6836-02 (ASTM 2000). On completion of water-retention tests, the sediment was oven dried and weighed. Bulk density was calculated as the ratio of the dry weight to the volume of the core. Porosity was calculated from the measured particle density and the bulk density as $\phi = 1 - \rho_b/\rho_s$.

Mathematical functions were fit to the retention data, and the resulting parameters are used directly in computer models for predicting water and contaminant movement. Numerous functions are available, but the van Genuchten (1980) function is most commonly used:

$$\theta = \theta_r + \frac{(\theta_s - \theta_r)}{\left[(1 + (\alpha h)^n\right]^{1-\frac{1}{n}}} \tag{2.8}$$

where θ_s = saturated water content (cm^3/cm^3)
θ_r = residual water content (cm^3/cm^3)
h = matric potential (-cm)
α, n = parameters that determine the shape of the soil water retention curve. α has units of (1/cm) and is related to the bubbling pressure whereas n is dimensionless.

Another commonly used function is that of Brooks and Corey (1964):

$$\begin{aligned} \theta &= \theta_r + (\theta_s - \theta_r)\left[\frac{h_b}{h}\right]^{\lambda} \quad && h > h_b \\ \theta &= \theta_s && h \le h_b \end{aligned} \tag{2.9}$$

where h_b = empirical fitting parameter related to the matric potential at air entry, being equivalent to when desaturation begins (-cm)
λ = empirical fitting parameters related to the soil pore size distribution (dimensionless).

2.6 Hydraulic Conductivity

Hydraulic conductivity is known to vary with saturation, and functions describing the saturation dependence are needed as model input. The saturated hydraulic conductivity (K_s) is the proportionality constant in the Darcy equation that relates the flux density to a unit potential gradient. The unsaturated hydraulic conductivity, [$K = f(h)$], is the proportionality factor in the Richards' water-flow equation that relates the flux density to a unit potential gradient at a specific water content. Because the water content varies in unsaturated soils, the unsaturated conductivity also varies. Mathematical functions are commonly used to calculate the unsaturated conductivity from the water-retention function with knowledge of K_s. Several functions are available, but the Mualem conductivity function is most commonly used (in conjunction with the van Genuchten retention function):

$$K(h) = K_s \frac{\left\{1 - (\alpha h)^{mn}\left[1 + (\alpha h)^n\right]^{-m}\right\}^2}{\left[1 + (\alpha h)^n\right]^{\ell m}} \tag{2.10}$$

In Eq. (2.10), $m = 1 - 1/n$, and l is a pore-connectivity parameter, estimated to be about 0.5 as an average for many soils (Mualem 1976). However, more recent studies (e.g., Schuh and Cline 1990; Yates et al. 1992; Schaap and Leij 1998; Zhang et al. 2004; Ward et al. 2006) suggest that other values of l may represent the hydraulic behavior of many soils equally well or better. In layered soils, saturation-dependent anisotropy, which can lead to increased lateral flow in some layers, is best described by a pore connectivity tensor (Zhang et al. 2003, 2004; Raats et al. 2004; Ward et al. 2006).

There were no measurements of unsaturated hydraulic conductivity or pore connectivity. Unsaturated K was computed from the water retention and measured saturated hydraulic conductivity. Saturated hydraulic conductivity was measured on triplicate samples by a constant-head method according to procedure D2434-65 (ASTM 1986). Saturated hydraulic conductivities were measured at 90 and 95% of the maximum dry density determined from the compaction tests. Pore connectivity was assumed to be 0.5 or optimized from field-scale infiltration experiments (Zhang et al. 2004; Raats et al. 2004).

2.7 Maximum Ponding Height for Surface Runoff

In STOMP simulations of barrier hydrologic response, infiltration is a multistage process in which the boundary condition is initially one of specified flux. However, under intense precipitation events, the rainfall rate may exceed the soil infiltration capacity at a node. Under such conditions, water is allowed to accumulate on the surface up to a maximum ponding height, $h_0^{\max}$. If the allowable $h_0^{\max}$ is exceeded during a rainfall event, the difference between the rainfall rate and infiltration capacity becomes the rainfall excess that instantaneously forms runoff. This water is rerouted horizontally along the land surface of the simulation domain. Owing to the simulation time requirements in STOMP-WAE-B that arise for the use of hourly meteorological data, the complex interactions associated with simulating overland flow are avoided by using a somewhat simplified linear reservoir approach (Figure 2.1).

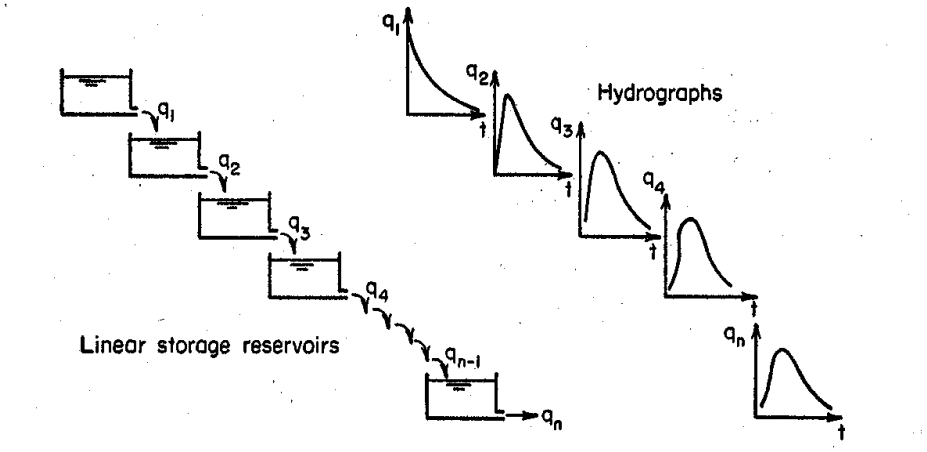

Figure 2.1. The Conceptual Model for Runoff in Which the Surface Boundary is Composed of *n* Linear Reservoirs in Series, where *n* is the Total Number of Surface Nodes (after Chow 1964)

To simulate runoff in STOMP, the maximum ponding height must be specified. The most appropriate value for h_0^{max} depends on topography and soil properties. For example, if the surface of the simulation domain is flat or uniformly sloping, then h_0^{max} is spatially uniform with a zero or positive value dictated by the expected height of accumulation for those conditions. If the surface includes a depression such as a furrow or channel, then water could move into the depression and accumulate to a height dictated by the depth of the depression. In this case, h_0^{max} is defined relative to the difference in elevation between the base of the depression and the highest point adjacent to the depression. There are no site-specific data to support the estimation of h_0^{max}. The required input values were determined from a literature search.

2.8 Thermal Properties

Knowledge of thermal properties is needed to simulate heat and fluid flow within the engineered barrier and to resolve the soil-plant-atmosphere energy balance. The movement of soil moisture in the aqueous and vapor phases is known to be influenced by thermal gradients. In unsaturated soils, thermal conductivity is a function of water content and may vary by a factor of about 4 for the typical range of field soil water contents. STOMP requires values to the thermal conductivity and specific heat capacity for each defined porous material type. Thermal properties are often determined through laboratory measurements on core or grab samples but are difficult to measure. However, they can be inferred directly from relationships between more easily measured properties, such as grain-size distributions, mineralogy, and water retention. For this data package, thermal properties were estimated by pedotransfer functions. Some properties were also derived from literature values measured on Hanford sediments (Cass et al. 1981; .Shannon and Wilson 1994).

2.8.1 Thermal Conductivity

The method developed by Johansen (1975) provides a basis for the relationship between thermal conductivity and soil suction as the soil desaturates. This method has been reported to give satisfactory results for saturations above 10 percent. At saturations below 10 percent, the function can be linearly approximated. The method is applicable to all soil types and enables the thermal conductivity to be calculated for various volume-mass combinations for a soil. The required input includes thermal conductivity at water saturation ($\theta = \theta_s$), quartz content, a fit of the soil water characteristic curve, soil state, and soil gradation. The fundamental relationship developed by Johansen (1975) is written as:

$$\lambda = \left(\lambda_{sat} - \lambda_{dry}\right)\lambda_e + \lambda_{dry} \tag{2.11}$$

where λ_{sat} is the thermal conductivity at saturation, λ_{dry} is the thermal conductivity of the soil matrix in the dry state, and λ_e is the Kersten number, defined as:

$$\lambda_e = 0.7 \log S + 1.0 \tag{2.12}$$

for coarse (<50% silt and clay) unfrozen soils while for fine (≥50% silt and clay) unfrozen soils, the Kersten number is defined as

$$\lambda_e = \log S + 1.0 \tag{2.13}$$

where S is the degree of saturation (θ/θ_s). Johansen (1975) also developed relationships to describe λ_{sat} and λ_{dry}:

$$\lambda_{sat} = 0.57^{\phi} \lambda_s^{(1-\phi)} \tag{2.14}$$

where ϕ is the soil porosity, and λ_s is the effective solids thermal conductivity. For soils in which the quartz content as a fraction of total solids present, q, is greater than 0.20, λ_s is defined as

$$\lambda_s = 7.7^{q} \cdot 2.0^{(1-q)} \tag{2.15}$$

For soils in which $q < 0.20$, λ_s is defined as

$$\lambda_s = 7.7^{q} \cdot 3.0^{(1-q)} \tag{2.16}$$

Use of these relationships therefore require an estimate of quartz content, q. There are few published data on quartz content as a function of soil type and there are none for Hanford soils. Nonetheless, it is known that sand usually contains a high percentage of quartz in crystalline form (Buckman and Brady 1969). Silt and clay may also contain silicates, but these are generally not in the form of crystals. Quartz crystals have a very high thermal conductivity, whereas the conductivity of quartz or silicate material bound inside clay or silt particles is similar to that of other soil materials (Farouki 1981). For the purposes of this data package, it was assumed that q for each soil type is related to the percentage of sand in the soil. The sand content was derived for particle-size analyses, and the average q content for a given soil was calculated by assuming that all the sand was composed of quartz.

The thermal conductivity of the soil matrix in the dry state is defined as:

$$\lambda_{dry} = \frac{0.137\rho_b + 64.7}{2700 - 0.947\rho_b} \tag{2.17}$$

where ρ_b is the dry bulk density of the soil.

To estimate the geotextile thermal conductivity, the geotextile was treated as a composite media containing polypropylene, water, and air. At saturation, the geotextile is assumed to be composed of only polypropylene and water while in the dry state, the geotextile consists of polypropylene and air. The composite thermal conductivity is described using the parallel-flow model expressed as:

$$\lambda = x_p\lambda_p + x_w\lambda_w + x_a\lambda_a \tag{2.18}$$

where λ is the thermal conductivity, x is the volume fraction, and p, w, and a are the geotextile components, being polypropylene, water, and air, respectively.

The thermal conductivity for the various components has been documented by Farouki (1981). The values for the components of interest are $\lambda_p = 0.12$ W m^{-1} °C^{-1}; $\lambda_w = 0.60$ W m^{-1} °C^{-1}; and $\lambda_a = 0.026$ W

m^{-1} °C^{-1}. The geotextile was assumed to be composed of a volume fraction of polypropylene equal to 0.112 cm^3 cm^{-3}. The polypropylene volume fraction was calculated using a geotextile porosity of 0.888 cm^3 cm^{-3}, determined by averaging the porosity values for the 14 geotextiles characterized by Iryo and Rowe (2003). A $\lambda(\theta)$ function was calculated by varying the volume fraction of water from zero to saturation.

The Johansen (1975) relationships have been implemented in the SoilVision software allowing the user, with prior knowledge of the soil water characteristics and quartz content, q, to calculate λ as a function of matric potential, h, or as a function of water content, θ. Using the Johansen (1975) relationships, $\lambda(\theta)$ were calculated for each porous material. For each soil type with unknown mineralogy, q was estimated using the grain-size distribution according to Peters-Lidard et al. (1998). Measured values of q were used for soils with known mineralogy. $\lambda(\theta)$ relationships were then predicted for each material. The final step in the process was to fit the resulting predictions for each material to the different thermal property functions used in the STOMP simulator.

The STOMP simulator offers several models for calculating thermal conductivity as a function of soil water content. These include the 1) *Constant* option in which the thermal conductivity is a constant value independent of temperature or saturation, 2) the *Parallel* option, which requires the thermal conductivity of the soil grains and models thermal conductivity with an equivalent parallel path model dependent on porosity, phase saturations, and temperature, 3) the *Linear* option, which scales the thermal conductivity between the unsaturated and saturated values depending on phase saturation, 4) the *Somerton* option, similar to the linear option, 5) the *Campbell* option, which describes the thermal conductivity as a function of saturation using a polynomial function, and 6) the *Cass* option, similar to the *Campbell* option but allows the additional specification of non-isothermal enhancement factors for vapor flow. The *Cass* option uses the model of Cass et al. (1984) to describe the thermal conductivity as a function of water content, $\lambda(\theta)$. The Cass model is the preferred option because of the ability to account for vapor diffusion enhancement factors. The thermal conductivity function is written as follows (Cass et al. 1984)

$$\lambda = A + B \cdot S - (A - D) \exp\left[- \left(C \cdot S \right)^E \right] \tag{2.19}$$

where λ (W m^{-1} $^oC^{-1}$)and S are previously defined, and A, B, C, D, and E are fitting coefficients.

The flow of water vapor in soils due to temperature gradients has been recognized since the early part of this century. It is also recognized that theories based on "simple" adaptations of Fick's Law of diffusion do not adequately describe thermally induced flow except for extremely dry soils (Cass et al.1984). In fact, it has been shown that at intermediate water contents, the vapor flux is enhanced, relative to that predicted by Fick's law, by factors of 1 to 15 (Gurr et al. 1952; Taylor and Cavazza 1954; Philip and de Vries 1957). Enhancement factors are used to account for the enhanced effects of thermal gradients on water vapor diffusion. Cass et al. (1984) reported a series of laboratory experiments designed to characterize the water vapor flow coefficients for two Hanford sediments, a lysimeter sand and Portneuf silt loam. Vapor-flow enhancement is also predicted using Equation 2.19 in which the five coefficients are replaced with five enhancement factors. STOMP allows specification of enhanced soil vapor diffusion as a function of clay fraction.

Measurements of thermal conductivity have been reported for a small number of samples collected in Hanford's 200 West Area (Shannon and Wilson 1994) and in the 300 Area (Cass et al. 1981). Data from these reports are used to verify the estimates.

2.8.2 Heat Capacity

Simulating water flow in a non-isothermal system also requires knowledge of specific heat for each porous material. The specific heat, c_s, of a porous material can be calculated by summing the product of c_s of all constituents and their respective volumetric fractions, x_j, as follows

$$c_s = \sum_{j=1}^{n} x_j \cdot c_{s,j} \tag{2.20}$$

where c_s = mass specific heat of solid phase (J g^{-1} C^{-1})
x_j = mass fraction of component j.

The volumetric heat capacity is related to the specific heat through the bulk density and is calculated within the model. Measurements of specific heat have been reported for a small number of samples collected in Hanford's 200 West Area (Shannon and Wilson 1994) and are used to verify the estimates.

2.8.3 Bare-Soil Albedo

Bare-soil albedo, defined at the ratio of reflected to incoming solar radiation, is known to be dependent on the moisture status of the soil surface (Idso et al. 1975). The albedo of surface of engineered barriers is an important parameter in predicting the effects of meteorological processes on hydrologic performance. On bare surfaces, i.e., barriers without a vegetative cover, soil properties determine the amount of solar radiation absorbed or reflected. As the albedo of a surface becomes higher, it absorbs less energy and maintains a cooler temperature. Thus, the energy balance is strongly influenced by values of bare-surface albedo used in the model. In STOMP, the downward short-wave radiation at the ground surface is obtained as input from the atmospheric data whereas the upward short-wave radiation at the ground surface is the reflected downward radiation. The net short-wave radiation into the ground surface is calculated from the incoming solar radiation as

$$R_s^{sn} = \left(1 - \alpha_g\right) R_s^{sd} \tag{2.21}$$

where R_s^{sn} is the net short-wave radiation into the ground surface (W/m^2), α_g is the bare-soil albedo, a measure of reflectivity or absorptivity of the bare surface, and R_s^{sd} is the downward short-wave radiation at the ground surface (W/m^2).

In the current version of STOMP, there are three options for describing the bare-surface albedo. In the default option, bare-soil albedo is assumed to be a function of soil color and soil moisture but independent of solar zenith angle, and surface roughness. Values of α_s for the different surface materials are specified based on soil texture and remain unchanged for the duration of the simulation. In reality, α_g is known to be a function of the solar altitude as well as aqueous water saturation, s_l. Thus, in the second option, α_g is allowed to vary with solar zenith angle and saturation according to Pleim and Xiu (1995),

$$\alpha_g = \alpha_z(\omega) + \alpha_s(s_l) \tag{2.22}$$

In Eq. (2.22) $\alpha_z(\omega)$ is defined as

$$\alpha_z(\omega) = 0.01[\exp(0.003286\,\omega^{1.5}) - 1] \tag{2.23}$$

Wang et al. (2005) proposed two approaches for calculating α_z based on their analysis of remote sensing data. They showed that bare-soil albedo, normalized to its value at a solar altitude $\omega=60^o$, could be adequately represented by the following function:

$$\alpha_z(\omega) = \alpha_r \cdot \{1 + B_1 \cdot [g_1(\omega) - g_1(60^o)] + B_2 \cdot [g_2(\omega) - g_2(60^o)]\} \tag{2.24}$$

where α_r is the albedo at $\omega=60^o$ and depends on season and location. The functions g_1 and g_2 are given by:

$$g_1(\omega) = -0.007574 - 0.070987\,\omega^2 + 0.307588\,\omega^3 \tag{2.25}$$

$$g_2(\omega) = -1.284909 - 0.166314\,\omega^2 + 0.04184\,\omega^3 \tag{2.26}$$

In Equation 2.24, $B_1 = 0.346$ and $B_2 = 0.063$. The third option makes use of a simpler formulation proposed by Wang et al. (2005) based on work of Briegleb et al. (1986). In this option, $\alpha_z(\omega)$ is defined as

$$\alpha_z(\omega) = \alpha_r \cdot \frac{1 + C}{1 + 2C \cdot \cos\omega} \tag{2.27}$$

where *C* is an empirical parameter that depends on the type of ground cover. In Eq. 2.22, α_s is the bare-soil albedo. The relationship between α_s and aqueous saturation is best described by a decreasing exponential function given by

$$\alpha_s(s_l) = \alpha_{wet} + (\alpha_{dry} - \alpha_{wet}) \cdot \exp(-\kappa \cdot s_l) \tag{2.28}$$

where α_{wet} is the soil albedo when the surface is near saturation (minimum albedo), α_{dry} is the dry soil albedo (maximum albedo), κ is the albedo attenuation factor that controls the rate of decrease albedo with moisture, and s_l is the moisture saturation at the surface given by θ/θ_s.

No measurements of bare-soil albedo have been reported in the literature for Hanford sediments. However, there is a large body of data for mineral soils in the remote sensing that was developed in efforts to predict soil moisture content from reflectance (Bowers and Hanks 1965; Idso et al. 1975; Graser and Van Bavel 1982). For example, Idso et al. (1975) reported a study of the bare-soil albedo for an Avondale loam and showed a direct relationship between albedo and soil moisture content. More recent studies in the agricultural sciences have focused on understanding the effects of tillage systems on the

albedo and have reported measurements under dry and moist surface conditions (e.g., Post et al. 2000; Oguntunde et al. 2006). The National Center for Atmospheric Research has also developed a generalized table of soil properties for use in circulation models of land-surface processes in which soil color and moisture are the two properties used to predict soil albedo (Dickinson et al. 1993). These sources were used to obtain best-estimate average values for the materials expected to be exposed on barrier surfaces.

2.9 Plant Properties

Plants have a major impact on the surface-energy partitioning that influences the balance of energy and water in an engineered barrier. In the canopy layer, part of the incident short-wave radiation is used for photosynthesis with the remainder being transmitted through the leaves or reflected by the canopy. Since short-wave radiation is the most important energy input, this has a strong impact on air and soil temperatures, humidity levels and evapotranspiration thereby controlling the microclimate and growing conditions. Knowledge of the canopy characteristics is also needed to allow the net rainfall reaching the surface of the barrier to be calculated. Information about the canopy and root distribution is therefore critical for simulating barrier performance and to understand changes in plant water uptake in response to changing atmospheric and soil conditions.

In the current model, vegetative growth is not implicit but is handled explicitly through temporal changes in plant parameters such as leaf area index and the plant area index. This information is then used to partition energy between plant canopy and soil as well as to parameterize functions for turbulent transport and evapotranspiration. The energy demand in the canopy determines the potential water loss by evapotranspiration, but it is the plant phenology or growth cycle and the root water stress function that dictate how much water the plant actually extracts from the soil. Plant parameters are therefore needed to describe the time-invariant characteristics that dictate how the canopy (leaves, twigs, and branches) microclimate is handled. The input parameters needed to describe plant distribution; canopy structure, and functions are described below.

2.9.1 Canopy Interception

Canopy interception is the depth of water that is retained on plant leaves and may constitute a significant portion of the incident precipitation in certain types of canopies (Calder 1977). Intercepted water may be absorbed by the plant surfaces, evaporated from the plant leaves, or eventually drip to the ground surface after the interception capacity is exceeded. Evaporation from the canopy can therefore have a significant impact on the energy and water balance of engineered covers, particularly in arid environments where precipitation amounts are low and canopy interception is high.

The interception capacity is the maximum volume of water that can be stored in the projected storage area of the vegetation (the area of leaves, twigs, and branches) that can retain water against gravity under still-air conditions (Ramirez and Senarth 2000). This is a measure of the efficiency of the vegetation in collecting and retaining precipitation as well as measuring rainfall intensity (Massman, 1980). A dependence of interception capacity on rainfall intensity has been reported by several authors (Massman 1980; Aston 1979; Ramirez and Senerath 2000). The interception submodel used in the STOMP simulator assumes an exponential decay of interception capacity with rainfall intensity and is written as,

$$h_0(i) = c_m e^{-ci}, \quad i \geq 0 \tag{2.29}$$

where h_0 = interception capacity (m)
i = precipitation rate (m s^{-1})
c_m = maximum condensate depth (m)
c = empirical constant.

Maximum condensate depth, c_m, is the maximum amount of water that can accumulate from interception or condensation within the canopy and depends on the vegetative characteristics of the canopy. The constant c depends on both vegetative and climatic conditions and characterizes the rate of decay of interception capacity with rainfall intensity (Ramirez and Senarath 2000).

There are no data for canopy interception on the Hanford site. A literature search revealed that there have been very few studies of canopy interception in rangelands and shrub-steppe ecosystems of semi-arid and arid areas. Nonetheless, sufficient data were found in a report by West and Gifford (1976) to provide estimates of canopy interception of precipitation in shrub-steppe ecosystems.

2.9.2 Plant Height

On a bare surface, the exponential wind-velocity profile approaches a zero velocity at a height z_m above the surface (Figure 2.2a). This height is known as the momentum roughness length, and it is a parameter used to account for the effect of surface roughness on wind flow. On a vegetated surface, the roughness length is displaced upward by a distance d_c, known as the zero-plane displacement. Zero-plane displacement is the height above the ground at which zero wind speed is achieved as a result of obstacles such as plants. A vegetated surface therefore has the effect of increasing the effective distance to the ground surface, and the wind velocity approaches zero at $z_m + d_c$. Plant water use is therefore influenced by the prevailing weather conditions, available water in the soil, and canopy characteristics. The plant height acts to increase the momentum roughness length, z_m, and the canopy zero-plane displacement, d_c (Figure 2.2b).

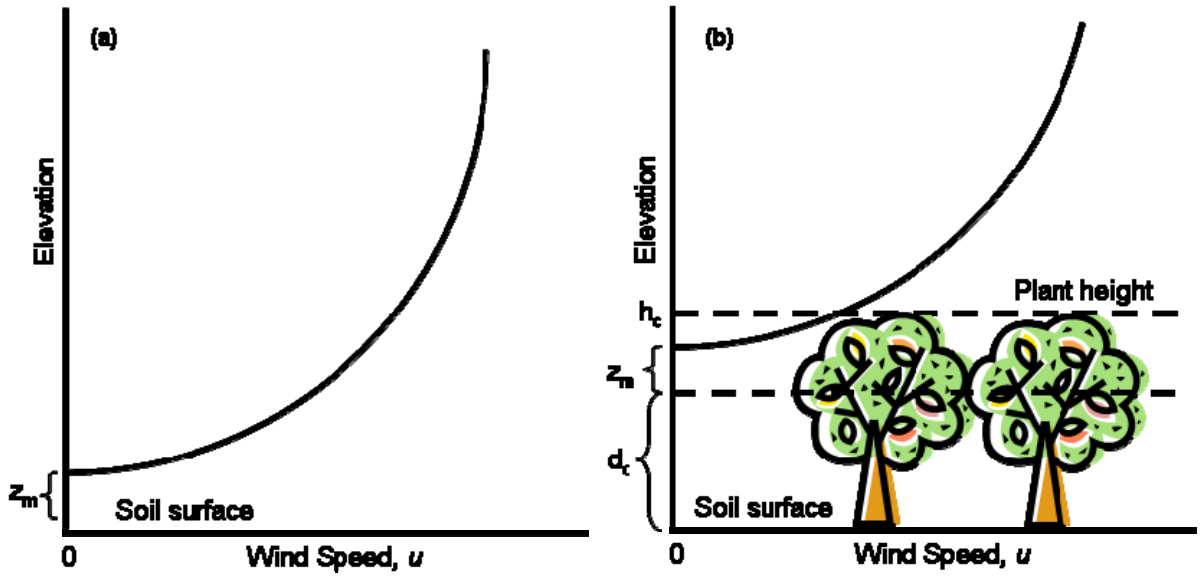

Figure 2.2. Roughness Length and Zero-Plane Displacement for (a) a Bare Surface, and (b) a Vegetated Surface.

Site data used to determine plant height input parameters include measurements from the 200-BP-1 prototype Hanford barrier (Ward et al. 1997) and from the published immobilized low-activity waste (ILAW) vegetation data summary (Downs and Khan 1999). Plant-height data are typically modeled using a sigmoid curve. Mathematically, the S-shaped curve is described by the continuous logistic growth curve, which is written as

$$h(t) = \frac{h_m}{1 + A e^{-k \cdot t}} \tag{2.30}$$

where $h(t)$ = plant height as a function of time, cm
h_m = maximum plant height, cm
A = constant related to the initial plant height, h(0)
t = time, years
k = rate of maximum plant growth, cm/yr.

Sigmoid curves are common in nature and represent a fairly good abstraction of the course of a self-limiting process such as the growth of an organism. Equation (2.21) was fitted to shrub-height data collected onsite. In the analysis, the maximum height, h_m, was fixed at the height recorded at the end of FY 2006 for the shrub species of interest. Sagebrush heights at the barrier are comparable to those reported for the older plants at the ILAW site by Downs and Khan (1999). There is a large body of data for z_m and d_c for a variety of bare and vegetated surfaces (e.g., Szeicz et al. 1969; Hansen et al. 1983; Monteith 1998).

2.9.3 Leaf-Area Index

The leaf area index of the i^{th} plant species, (L_{ai}^{i}) is the ratio of total upper leaf surface of the plant divided by the surface area of the ground occupied by the plant canopy. The plant canopy dominates the energy balance through its effect on soil and plant albedo, momentum and thermal roughness, and ultimately the water balance. The interplay between the plant canopy and the energy and water balance is through the control exerted by the areal distribution of vegetation. Because the canopy controls the partitioning of energy and the microclimate of the cover, L_{ai}^{i} is a key parameter for simulating the exchange of water vapor with the atmosphere.

While there is an abundance of L_{ai}^{i} data for crop plants, little information is available for the species of interest for the proposed engineered surface barriers. For site-specific information, measurements made at the 200-BP-1 prototype Hanford barrier over the last several years were used to develop a model for L_{ai}^{i}. First, the model derived by Ward et al. (1997) was applied using the measured heights of plants. This model is described with a polynomial equation written as

$$\begin{aligned} Y = {} & b_0 + b_1 \cdot d + b_2 \cdot h_c + b_3 \cdot w + p_w + b_5 \cdot trt \\ & + b_6 \cdot h_c^2 + b_7 \cdot w^2 + b_8 \cdot h_c \cdot w \cdot p_w + b_9 \cdot w \cdot trt \end{aligned} \tag{2.31}$$

where Y = Leaf area (cm^2)
b_i = i^{th} coefficient of polynomial
d = Day of year (1-365)
h_c = Plant height (cm)
w = Greatest projected canopy diameter (cm)
p_w = Diameter measured 90^o to w (cm)
trt = Treatment code (1=irrigated, 0=non-irrigated).

Canopy leaf areas are not used directly in the STOMP model so they must be converted to a value of L_a^i. The conversion uses the following equation

$$L_{ai}^i(d)=\frac{Y(d)\cdot N}{f\cdot A} \tag{2.32}$$

where L_{ai}^i = leaf area index ($m^2\ m^{-2}$)
Y = canopy leaf area (cm^2)
N = number of plants in each treatment
N =1977 in the non-irrigated treatment
N =1686 in the irrigated treatment
f = factor (10^4) to convert cm^2 to m^2
A = area in each half of the measured barrier surface =1296 m^2
d = day of year (1 to 365).

Estimates of L_{ai}^i covering the period 1932–2000 have been compiled at the Oak Ridge National Laboratory Distributed Active Archive Center (DAAC) into a single data set. This data set provides a benchmark of typical values and ranges of L_{ai}^i for a variety of biomes and land cover types in support of model development and validation of satellite-derived remote-sensing estimates of L_{ai}^i and other vegetation parameters. These data are linked to a bibliography of over 300 original-source references. In addition to these sources, a few others were found that focused on sagebrush and rabbitbrush (e.g., Caldwell 1979).

2.9.4 Plant Area Index

The plant area index is also a crucial plant input parameter when simulating mass and energy exchange between barrier surface and the atmosphere. Traditionally, the plant area index of species *i* (P_{ai}^i) refers to all of the light-blocking elements of a plant (stems, twigs, leaves) compared to the leaf area index (L_{ai}^i), which accounts only for leaves. Here, the meaning of P_{ai}^i is extended to that of a vegetation fractional cover, taking into account the spatial distribution of the vegetation, to provide a measure of vegetation density. Thus, the summation of P_{ai}^i over all plant species is ≤ 1.0. In a full canopy typical of agricultural crops, P_{ai}^i is close to 1.0, and a single species accounts for essentially all of the ground cover.

In the sparse canopies typical of arid environments and those expected on engineered barriers, there may be multiple species with various leaf area indices. However, P_a^i can be less than 1.0 as some of the surface will be bare soil, and some will be covered with litter and even soil cryptograms (Figure 2.3).

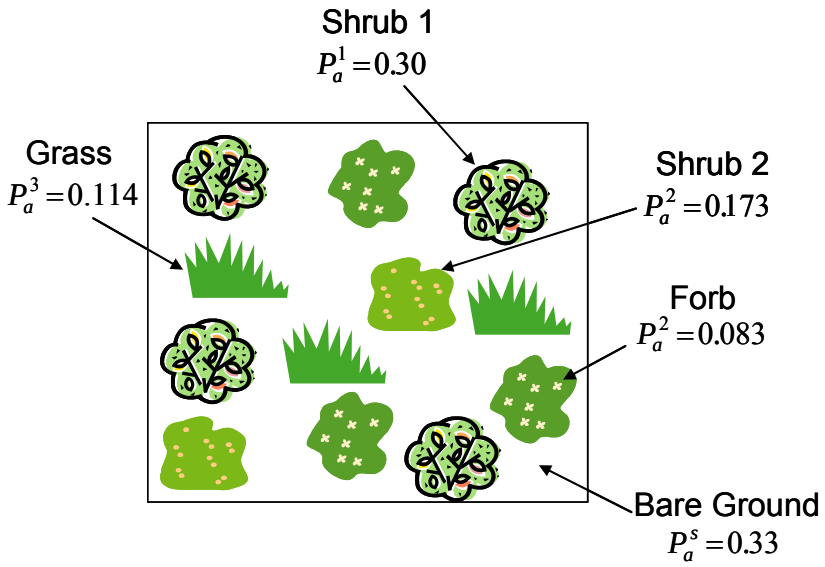

Figure 2.3. Schematic of Barrier Surface Showing the Concept of Plant Area Index for two Species of Shrub, a Grass, and a Forb. The sum of P_a^i for all the plant species, and bare ground must be 1.0.

Measures of plant density in a mature sagebrush community, including the percentage cover of shrubs, native grasses (principally Sandberg bluegrass) and native forb cover, have been reported for several proposed disposal sites at Hanford. The percent canopy cover for the 200-BP-1 prototype Hanford Barrier has also been documented over the last 13 years (Ward et al. 2005b,c; 2007)

2.9.5 Root Distributions

Root distributions, including the density and maximum rooting depth, exerts a large degree of control on the fluxes of water to the atmosphere and groundwater. Accurate simulation of these fluxes requires knowledge of spatial and changes in rooting patterns. In STOMP, the submodel used to describe the spatial distribution of roots is based on the root distribution equation described by Vrugt et al. (2001). This equation is written as:

$$\beta(z) = \left[1 - \frac{z}{z_m}\right] e^{-\left(\frac{p_z}{z_m}\right)|z^* - z|} \tag{2.33}$$

where z = depth (m)
$\beta(z)$ = root distribution factor at depth z
z_m = maximum rooting depth (m)
p_z = parameter to ensure zero uptake at $z = z_m$
z^* = parameter to ensure maximum uptake at $z = z_m$.

Parameterization of Eq. 2.33 requires the fitting of measured root distribution to the function to derive three model parameters, namely z_m, p_z, z^*.

2.9.6 Transpiration Reduction Functions

The actual uptake of water depends not only on the spatial distribution but also on temporal changes in the rate of uptake, which is controlled by soil water status, and on the potential transpiration. To account for the reduction in plant water uptake, a root stress factor or transpiration reduction factor, γ, that depends on soil water pressure, h, is required. The transpiration reduction function accounts for soil conditions that limit water uptake. For example, conditions that are too dry or too wet or soils that are too saline can all limit water uptake. Numerous forms of the transpiration reduction function have been proposed over the years (Feddes and Raats 2004). There are two general model types that have been most commonly used, 1) piecewise linear (threshold-type) functions and 2) continuous smooth functions. The detailed information on root distributions and transpiration that would be needed to select from the different models is difficult to obtain and mostly unavailable for shrub/grass associations. Therefore, STOMP includes options for both the piecewise linear and smooth functions and a third that combines the two model types. The piece-wise linear transpiration reduction function is based on the model of Feddes et al. (1978) and is parameterized using four critical values of soil matric potential h_1, h_2, h_3, and h_4 such that $h_4 < h_3 < h_2 < h_1$. The function is written as (Feddes et al. 1978):

$$\gamma(h)=\begin{cases} 0, & h \le h_4 \\ \dfrac{h-h_4}{h_3-h_4}, & h_3 > h > h_4 \\ 1.0, & h_2 \ge h \ge h_3 \\ \dfrac{h-h_1}{h_2-h_1}, & h_1 > h > h_2 \\ 0, & h \ge h_1 \end{cases} \tag{2.34}$$

A schematic of the piece-wise linear transpiration reduction function is shown in Figure 2.4a.
The smooth transpiration reduction function is sigmoid and is based on the model of Norero (1969). This function requires two parameters, h^* and k. The parameter h^* is the value of h at which the transpiration is equal to 50% of the maximum transpiration. The parameter k is an empirical parameter that determines the slope of the curve. The resulting function, graphed in Figure 2.4b, is written as (Norero 1969):

$$\gamma(h)=\frac{1}{1+\left(\dfrac{h}{h^*}\right)^k} \tag{2.35}$$

In this model, water uptake is insensitive to wet conditions ($h \rightarrow 0$ cm). This is not an unreasonable assumption for the simulation of a shrub-steppe ecosystem. Shrub-steppe typically has just enough moisture to support a cover of perennial grasses and/or shrubs, and growing conditions are mostly water stressed. If saturated conditions did occur, they would be unlikely to persist long enough to cause a significant reduction in transpiration.

The third option uses the piece-wise linear function at high matric potentials with the sigmoid function becoming active at lower matric potentials (van Asch 2001). This function requires five parameters, h_1, h_2, h^*, h_4, and k. The function is defined as

$$\gamma(h)=\begin{cases}0, & h \le h_4 \\ \dfrac{1}{\left(1+\dfrac{h}{h^*}\right)^k}, & h_2 > h > h_4 \\ 1.111 \cdot h - 1.111, & h_1 > h > h_2 \\ 0, & h \ge h_1\end{cases} \tag{2.36}$$

in which $h_4 < h^* < h_2 < h_1$, as in Eq. 2.34. The shape of the function is shown in Figure 2.4c.

Parameterization of the transpiration reduction functions therefore requires the critical stress points as well as the pressure head at which uptake is reduced by 50%, h^*. The functions account for soil conditions that limit water uptake. Under conditions that are too wet ($h > h_1$), uptake is limited by reduced oxygen availability. The points h_3 and h_2 generally depend on the evaporative demand of the atmosphere, and between these two pressures, uptake is at the potential rate. Soil conditions that are too dry ($h < h_3$) also limit demand, and water uptake ceases when the wilting point, h_4, is exceeded. These stress points are well documented for crop species, but few data exist for native species proposed for use in vegetating engineered barriers.

Most crop plants and plants from wetter parts of the country begin to wilt when leaf water potential drops to 15 bars (-1.5 MPa). A review of the literature suggests that native shrubs like sagebrush and rabbitbrush have developed several strategies to survive for long periods without wilting. Sagebrush, for example, has green leaves all summer long because it is able to concentrate its cell sap with compounds that will attract water from relatively dry soil (Link et al. 1994). Water potentials as low as 85 bars (-8.5 MPa) have been observed in live sagebrush. Rabbitbrush has small hairy leaves and branches with a covering of closely matted woolly hairs that reduce water loss.

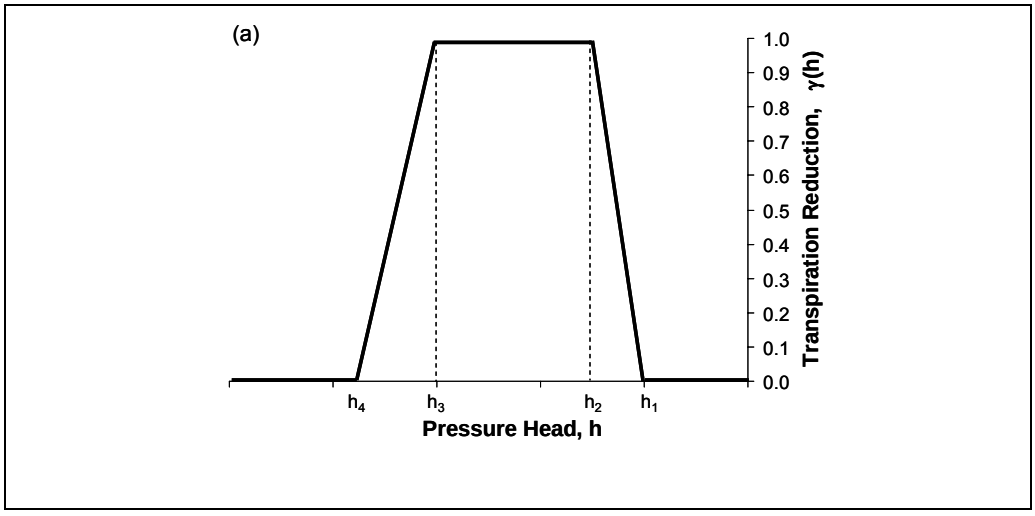

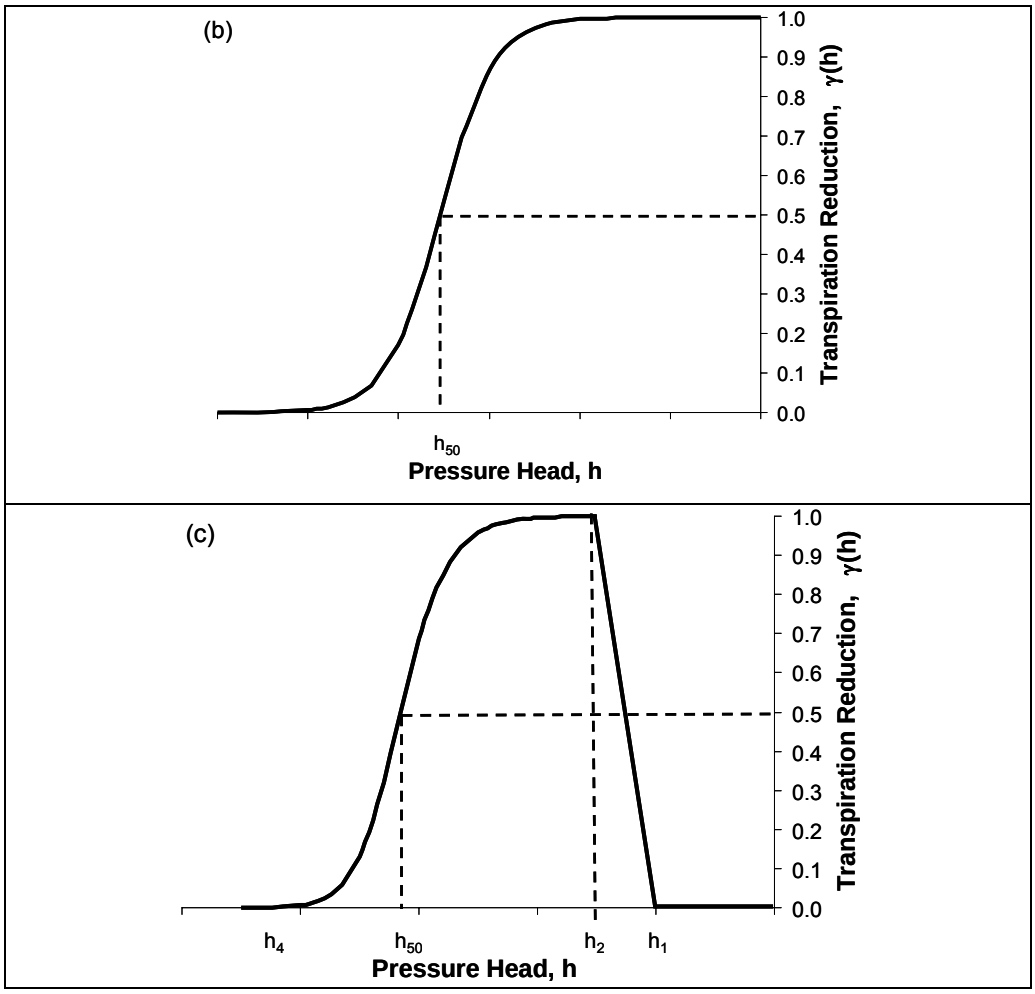

Figure 2.4. Plots of Transpiration Reduction Functions Available in STOMP, (a) Piece-Wise Linear Function (Eq. 2.34), (b) the Sigmoid Function (Eq. 2.35), and (c) the Combined Function (Eq. 2.36)

2.9.7 Plant Growth Cycle

Plant phenological response is controlled by complex interactions of soil temperature, soil water availability, radiation, and plant genotypic or phenotypic characteristics (Kremer et al. 1996). The current version of STOMP does not have the capability to simulate plant growth but allows the user to vary plant parameters over time to mimic such a response. Seasonal development is handled through the temporal distribution of the transpiration coefficient, K_c (Figure 2.5). If water is not limiting, plants will continue to develop until K_c reaches a maximum, and evapotranspiration reaches it full potential. At present, the user specifies the time of germination or greening up of a particular species, and this can be done only once for a given simulation.

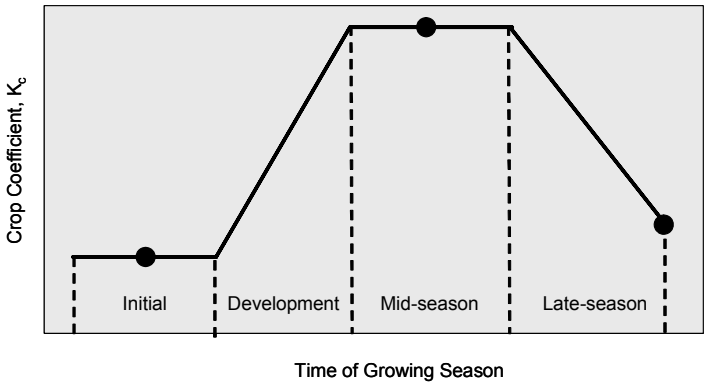

Figure 2.5. Schematic of a Transpiration Coefficient Curve for a Perennial Species Over a Single Growing Season

However, the leaf-area index and plant-area index can change hourly as these variables are read in with the meteorological input data. Because different species mature at different rates, the shape of the growth cycle varies and so does the transpiration coefficient. For a given species, the actual transpiration, T_a, can be higher or lower than the potential transpiration, T_0, depending on climatic conditions and the stage of development. In the model, T_a is calculated by multiplying T_0 by the transpiration coefficient, K_c,

$$T_a = K_c\, T_0 \tag{2.37}$$

From Eq. 2.37, the transpiration coefficient is simply the ratio of T_a to T_0. The transpiration coefficient is therefore used to scale actual transpiration to the potential transpiration. In STOMP, the $K_c(t)$ curve is defined with three average values of K_c (initial, mid-season, and late-season) and four growth-stage lengths (initial, development, mid-season, and late-season) as shown in Figure 2.5. Values of K_c for any period of the growing season can be derived by considering that during the initial and mid-season stages, K_c is constant and equal to the K_c value of the growth stage under consideration. During the crop development and late season stage, K_c varies linearly between the K_c at the end of the previous stage.

The required input is therefore information about the stages of development for each plant species of interest. The four development stages are defined using 1) initial stage, $K_{c\,ini}$, 2) development stage, $K_{c\,dev}$, 3) mid-season, $K_{c\,mid}$, and 4) the late-season or end stage, $K_{c\,end}$. Each of these stages of development is defined by growth-stage lengths by specifying the day of year (1 to 365) for the start of each stage: 1) initial stage start, L_{ini}, 2) development stage start, L_{dev}, 3) mid-season start, L_{mid}, and 4) late-season start, L_{late}. At present, only a single $K_c(t)$ curve can be specified for each plant in a given simulation. Different growth curves can be used from year to year by running a separate simulation for each year with a restart file from the previous year and a new growth curve.

The growth stages of the plant species of interest were specified through literature searches. The Fire Effects Information Service (FEIS) of the USDA Forest Service maintains a database of native plants, their biology, ecology, and relationship to fire. The database provides detailed information about the shrubs of interest as well as for the grasses at http://www.fs.fed.us/database/feis/plants/index.html.

2.9.8 Bulk Stomatal Resistance

Water-vapor loss from plants is controlled by the stomatal resistances and leaf boundary-layer resistances that act in series. Stomatal resistance, r_{pc}^{s}, is a complex function of environmental and physiological variables including atmospheric turbulence intensity, climate, water availability, radiation intensity, temperature, and vapor-pressure deficit (Jarvis 1976). Stomatal resistance increases when the plant is water stressed, causing a decrease in transpiration. In STOMP, the calculation of r_{pc}^{s} is simplified to reduce the number of required input parameters. The bulk stomatal resistance or canopy resistance is needed to model transpiration from the canopy. This is computed by scaling r_{pc}^{s} to the plant-area index. At present, there are two options for determining r_{pc}^{s}, each with different input requirements. The first option, also the default option, assumes that r_{pc}^{s} is affected only by the net solar radiation. Values of r_{pc}^{s} are calculated simply as

$$r_{pc}^{s} = r_{pc,\min}^{s} \cdot f_T \tag{2.38}$$

where $r_{pc,\min}^{s}$ (s m^{-1}) is a minimum stomatal resistance that is applied to all plant species, and f_T is a correction factor calculated as follows:

$$f_T = \frac{400 + R_n^s}{1.4 \cdot R_n^s} \tag{2.39}$$

In Equation (2.39), $r_{pc,\min}^{s}$ is the minimum stomatal resistance (s m^{-1}) and is fixed for all plant species at 50 s m^{-1}, and R_n^s is the incoming solar radiation as (W m^{-2}) read as input from the meteorological data. There are no other required input parameters.

The second option uses a discontinuous switch model to incorporate the effects of temperature and incoming solar radiation into stomatal function. This option allows r_{pc}^{s}, which incorporates a corrections factor to account for the effects of humidity, water stress, and temperature (Jarvis 1976; Hicks et al. 1987). In this sub model, r_{pc}^{s} is calculated as

$$r_{pc}^{s} = r_{pc,\min}^{s} \cdot \left(1 + \beta \cdot I^{-1}\right) f_T^{-1} \tag{2.40}$$

where f_T is a temperature factor that corrects for absolute temperature. The correction factor is calculated as follows:

$$f_T = \frac{(T - T_c)}{(T_o - T_e)} \left[\frac{T_h - T}{T_h - T_o} \right]^{\left(\frac{T_h - T_o}{T_o - T_e} \right)} \tag{2.41}$$

In Equations (2.40) and (2.41),

$r^{s}_{pc,\min}$ = minimum stomatal resistance (s m^{-1})
β = light response coefficient (Wm^{-2})
I = sunlight intensity (Wm^{-2})
f_T = correction to account for stomatal response outside a given temperature range
T = ambient temperature (K)
T_e = minimum temperature for stomatal opening (K)
T_h = maximum temperature (K)
T_o = optimum temperature (K).

Required input parameters are $r^{s}_{pc,\min}$, T_h, T_e, T_o, and β. These are all species-dependent, and no data have been identified for the Hanford site. However, there exists a large body of data in the air pollution and meteorology literature for plant species typical of the shrub-steppe ecosystem. The U.S. Environmental Protection Agency (EPA) has published some of these parameters for a variety of vegetation types for use in deposition calculations for the Clean Air Status and Trends Network (CASTNET). Battye and Barrows (2004) recently summarized these parameters for "natural vegetation." These data served as the source for this data package.

2.9.9 Plant Albedo

As with a bare-soil surface, the net radiation onto a vegetated surface is expressed in terms of downward and upward radiation fluxes. The downward short-wave radiation from the atmosphere is derived from the atmospheric data. A portion of this radiation strikes the ground surface directly, without being intercepted by plants, while another portion is attenuated by intervening plants. Plant albedo is known to vary with solar angle, spatial distribution of vegetation (height, density, etc.) and to some extent, with the spectral properties of the individual surface components. Albedo measurements in grassland, mixed grassland and woodland, and shrub-steppe ecosystems suggest that albedo varies with phenological stage. Following emergence from the dormant period, the albedo of grass-dominated areas typically decreases as the canopy expands and greens up to obscuring bare soil and litter. Sharp changes in albedo coincide with major changes in phenology, such as leaf emergence, the formation of reproductive heads, and their sequential senescence (Baldocchi et al. 2004). Albedo reaches a maximum in the summer and fall following flowering-induced dormancy that cause drying to a more reflective golden-brown color. Woodland and shrubs also show a similar temporal trend with sharp changes that coincide with leaf expansion. In general, albedo is lower than grassland during the summer, perhaps because the multi-storied structure traps sunlight.

Similar temporal trends could be expected for shrub-steppe ecosystems, although the specific timing of changes in albedo and the absolute values would be expected to differ because of differences in phenology. In fact, Hanson (2001) reported seasonal trends in albedo for stands of Wyoming big sagebrush (*Artemisia tridentata wymomingensis*) and bluebunch wheatgrass (*gropyron spicatum*) that appear strongly correlated with phenophase. Thus, computation of net short-wave radiation therefore requires an estimate of the canopy albedo for each plant species, α^{i}_{p}. To describe the dependence of α_p on phenophase, we adopted an approach similar to that used for the transpiration coefficient. Plant albedo is then defined at the start and end of the four main development stages of the growth developmental cycle: initial, development, mid-season, and late season, with four stage lengths (initial, development, mid-season, and late-season) as shown in Figure 2.6.

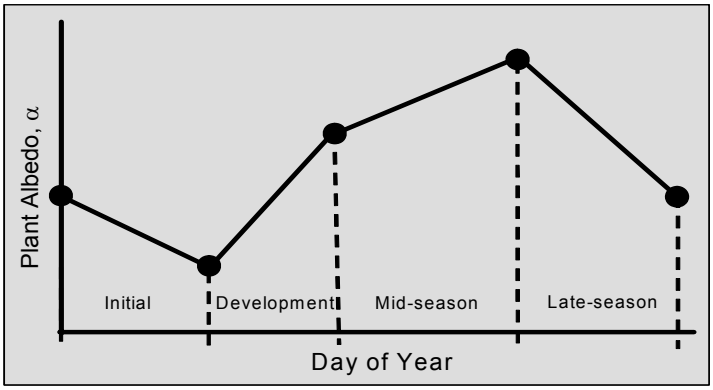

Figure 2.6. The Relation Between α_p^i and the Total Accumulated Growing Days

The plant albedo is a user-specified function used to model the change with phenophases. To parameterize α_p^i, five time points and three average values of α_p^i are required. This approach is consistent with the description of crop developmental stages: 1) initial, 2) crop development, 3) mid-season, and 4) late season. Linear interpolation is used between the intermediate time points and between the end of the late-season stage and the end of the calendar year (day of year [DOY] 365). STOMP input requirements include plant albedo at the start of the simulation, α_1; the minimum albedo that typically occurs between the initial and developmental stages, α_2; albedo at the end of the developmental stage (start of the mid-season), α_3; albedo at the start of the late-season stage, α_4; and an albedo at the end of the late-season stage.

2.10 Summary of Required Properties and Parameters

Because of the design requirements, the hydrologic design of engineered barriers requires analysis of complex interactions between climate, soil, and plants. In designing an engineered barrier, the interest is in identifying the most ideal soil materials and their arrangement and how to maximize water by recycling water to the atmosphere by evaporation and plant transpiration. Simulating the complex interactions among these processes requires a comprehensive simulation model, such as STOMP. The STOMP code requires a number of parameters to describe the hydraulic and thermal properties of porous materials as well as the phenology and physiology of plant species. Information on soil mechanical properties is also needed to support the engineering design. The preceding sections identified the parameters needed to support model simulations and engineering design.

Not all of the parameters required for characterizing the properties of geotechnical and soil materials and to describe the phenology and physiology of native plant species to be used in revegetation were readily available. However, extensive literature searches showed that some of the parameters or data from which the parameters could be derived were available in the open literature or in site historical records. When available, data were fitted to various analytical models to derive the required parameters needed for STOMP input. Most of the data sources, the resulting parameters, and justification for their selection were summarized in the report by Ward et al. (2005a). Most of the remaining parameters were derived from laboratory measurements conducted on soil materials expected to be used in constructing the 200-UW-1 barriers. Measurements were made at PNNL, Shannon and Wilson, Inc. (SW), Daniel B Stevens (DBS), and Geoengineers (GEO). Some of these parameters were also summarized by Ward et al.

(2005). Since this report was published, revisions of the STOMP code resulted in a need for additional parameterization, and the additional parameters are included in the current document. Tables 2.1 through 2.3 provide a summary of the different data types and their sources. Best-estimate values derived from literature values and site-specific data are presented in the next section.

Table 2.1. Summary of Soil Data and Sources

Component	Property	Symbol	Source
Soil	Albedo	α	Literature
	Compression Index	C_c	GEO
	Dry bulk density	ρ_b	PNNL
	Mass wetness	θ_m	PNNL
	Moisture retention	$\theta(h)$	PNNL, DBS
	Optimum Water Content	θ_{opt}	PNNL, GEO
	Particle density	ρ_s	PNNL, DBS
	Particle size distribution	psd	PNNL, DBS
	Plasticity Index	PI	GEO, DBS
	Ponding Storage Maximum	h_0^{max}	Literature
	Porosity	ϕ	PNNL, DBS
	Saturated hydraulic Conductivity	K_s	PNNL, DBS
	Saturated Conductivity (Directional)	K_{sx}, K_{sz}	PNNL
	Specific Heat	C	SW PNNL
	Thermal Conductivity	λ	SW PNNL
	Unsaturated hydraulic Conductivity	$K(\theta)$	PNNL, DBS

Table 2.2. Summary of Geotextile Data and Sources

Component	Property	Symbol	Source
Geotextile	Albedo	α	Literature
	Compression Index	C_c	Measured, GEO
	Dry bulk density	ρ_b	Measured, DBS, PNNL
	Mass wetness	θ_m	Measured, PNNL
	Moisture retention	$\theta(h)$	Measured, DBS, PNNL
	Optimum Water Content	θ_{opt}	Measured, GEO, PNNL
	Particle density	ρ_s	Measured, DBS, PNNL
	Particle size distribution	psd	Measured, DBS, PNNL
	Plasticity Index	PI	Measured, GeoEngineers
	Porosity	ϕ	Calculated PNNL
	Saturated hydraulic Conductivity	K_s	Measured, DBS, PNNL
	Saturated Conductivity (Directional)	K_{sx}, K_{sz}	Estimated, PNNL
	Specific Heat	C	Literature (SW), Estimated
	Thermal Conductivity	λ	Literature (SW, Estimated
	Unsaturated hydraulic Conductivity	$K(\theta)$	Calculated, DBS, PNNL

Table 2.3. Summary of Plant Data and Sources

Component	Property	Symbol	Source
Plants	Albedo	α	Literature
	Canopy zero plane displacement	d	Literature
	Transpiration Coefficient	K_c	Literature
	Growth Cycle	C	Literature
	Height	h_c	Literature
	Maximum condensate depth	c_m	Literature
	Leaf Area Index	L_{ai}	Literature
	Momentum Roughness Length	z_m	Literature
	Plant Area Index	P_{ai}	Literature
	Root Distribution	$\beta(z)$	Literature
	Thermal Roughness Length	z_h	Literature

3.0 Best-Estimate Values for Hydraulic Parameters

This section summarizes the best-estimate values for the hydraulic parameters of the soil and geotechnical materials to be used in the performance-assessment analyses of the candidate barriers. The term "best-estimate values" does not mean that the hydraulic parameters presented are inferior but instead signifies that the parameters are the best estimates given the data available and the current state of the science. A description of the source of these values is included and where appropriate, the method by which the parameters were estimated. In determining the best-estimate parameter values, it has been assumed in most cases that the saturated volumetric water content is equal to the porosity. Field saturation can be estimated by assuming a value for the volume of pores containing entrapped air.

3.1 Silt Loam

The silt loam to be used in constructing the U-plant waste site barriers is assumed to be mined from a borrow site located south of Rattlesnake Barricade and Highway SR240 (Petersen, 2003). The location of the borrow source is shown in Figure 3.1. In FY 2003, some 70 samples were obtained from this site for borrow-source characterization over a 0.82-square-mile area. Laboratory analyses of select samples were performed by Shannon and Wilson and D.B. Stephens and Associates and included:

- Dry Bulk density
- Particle density
- Grain size analysis (sieve and hydrometer)
- Proctor (moisture-density)
- Plasticity index (Atterburg limits)
- Unconfined compression strength
- Moisture content
- Saturated hydraulic conductivity
- Unsaturated hydraulic conductivity
- Moisture-retention characteristics.

This report focuses on the set of samples collected from the sub area of the borrow site that will be mined for fine-grained soils for use in U Plant waste-site surface barriers. The sample locations and associated laboratory testing are summarized in Table 3.1. The details of this characterization effort will be reported by others. For model parameterization, we limited our analysis to samples from the 0 to 12 ft depth of the sub area to be excavated. The sub area is best represented by samples from borings 17 and 18 (Figure 3.1). The samples of interest are B18DD5, B18DF5, and the two composites B18DD3/B18DD2, and B18DD4/B18DF7. Particle-size distribution curves for these samples are presented in Figure 3.2 with the associated size statistics given in Table 3.2.

Table 3.1. Sample Location and Laboratory Tests Performed for Sub Area Silt Loam Soils

HEIS #	Well	Boring	X Coordinate	Y Coordinate	Depth Interval Feet BGS	Initial Soil Properties w, ρ_d	K_{sat}	K_{unsat}	SMCC	GSD	SG	P	PI	CS	Notes
B18DD2	4278	17	568739.038	128370.227	1-4.7										
B18DD3	4279	18	569005.838	128369.127	1-4.5 & 1-2.7	X	X	X	X	X	X	X	X	X	Composite
B18DD4	4275	14	569546.739	128630.527	1-6.3										
B18DF7	4291	30	568153.261	128034.105	0.5-17.8	X	X	X	X	X	X	X	X	X	Composite
B18DD5	4272	11	568742.238	128628.527	6.5-7.8	X	X	X	X	X	X		X		
B18DF5	4277	16	568480.737	128367.027	5.2-5.8	X	X	X	X	X	X		X		

w = Mass Wetness
ρ_d = Dry Bulk Density
K_{sat} = Saturated Hydraulic Conductivity
K_{unsat} = Unsaturated Hydraulic Conductivity
BGS= below ground surface
SMCC = Soil Moisture Characteristic Curve
GSD = Grains Size Distribution
SG = Specific Gravity
P = Proctor Test
PI = Plasticity Index
CS = Compression Strength

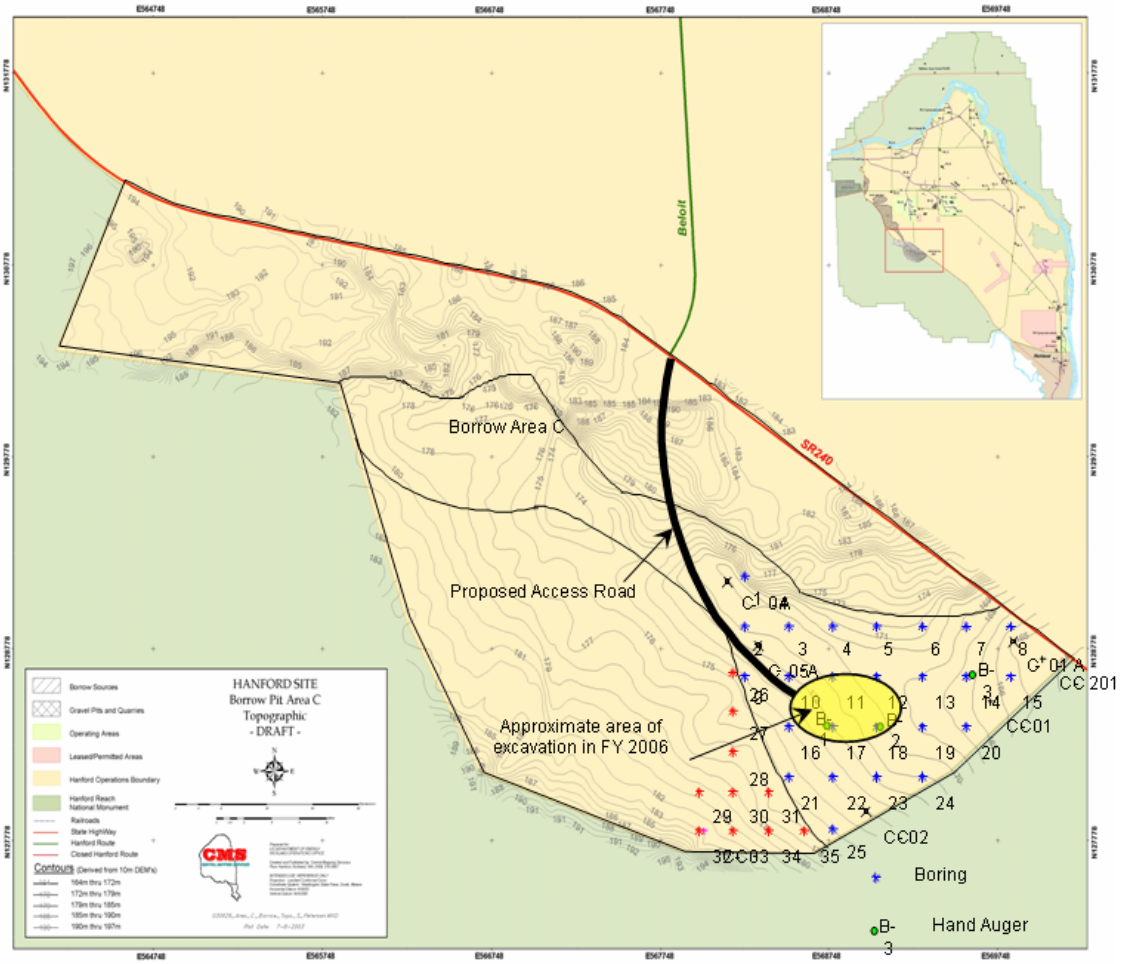

Figure 3.1. Location of Fine-Grained Soil Borrow Area Located South of the 200 West Area

Soil textural classes ranged from silt to sandy silt following the USCS and from sandy loam to silt loam following the USDA classification system. In this report, the borrow site fine-grained soil is referred to as silt loam. The grain-size distribution and water-retention data were used in the estimation of thermal properties for the silt loam and for both hydraulic and thermal properties of the silt loam-gravel admixture. A summary of the fitted van Genuchten (1980) parameters for the subset of samples analyzed by Daniel B. Stephens and Associates Inc. and documented in letter report by DBS[(a)] is in Table A1 of Appendix A. The best-fit parameter values and the means for the four samples of interest are given in Table 3.2.

The mean-saturated hydraulic conductivity is the geometric mean of the four sample values. Plots of the measured water-retention data and retention curve predicted using the mean van Genuchten parameters and one standard deviation of the mean parameters are presented in Figure 3.3.

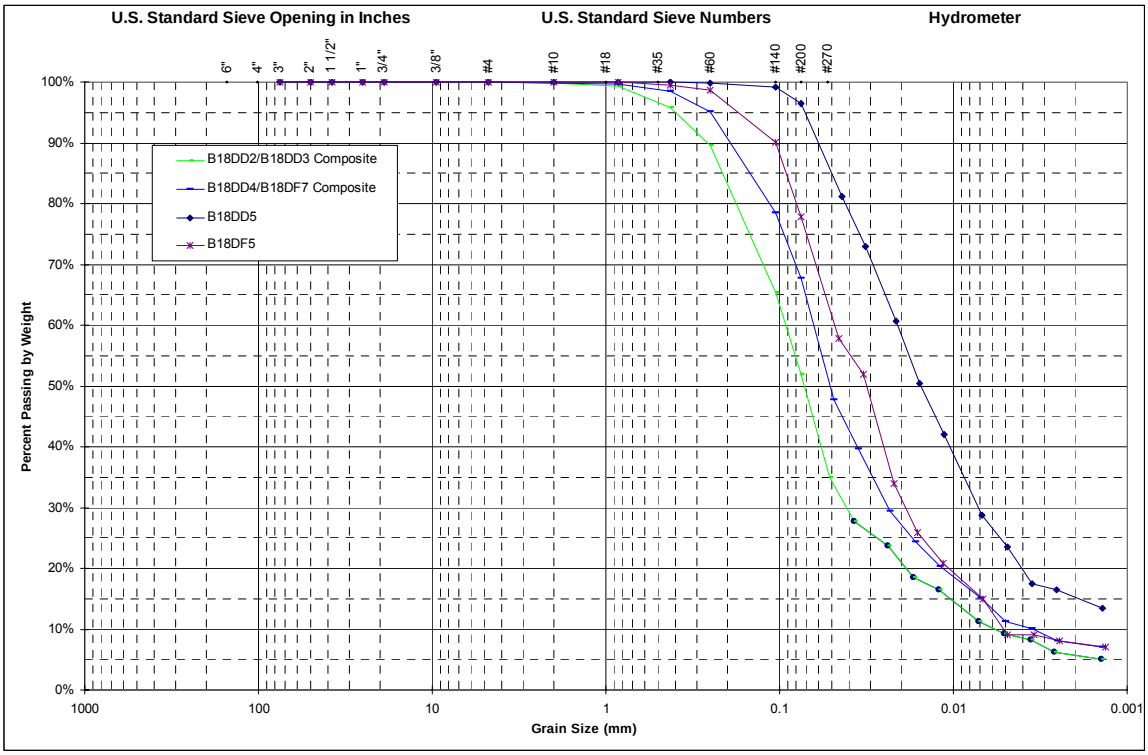

Figure 3.2. Particle-Size Distribution Curves for the Silt Borrow Site Samples

([a]) Daniel B. Stevens and Associates Incorporated. 2004. "Area C- Fine-grained Soils Characterization." Letter Report submitted to Fluor Hanford.

Table 3.2. Particle Size Statistics for the Silt Borrow Site Samples

Sample ID	USCS Texture	ASTM-D422 % Clay	ASTM-D422 % Silt	USCS % Sand	USCS % Coarse	D_{10} (mm)	D_{15} (mm)	D_{50} (mm)	D_{60} (mm)	D_{85} (mm)	Graphic Mean (mm)	Inclusive Graphic Standard Deviation (mm)	Sorting Index	C_c	C_u
B18DD2/B18DD3 Composite	Sandy Silt	9.23	42.74	48.03	0.00	0.0057	0.0104	0.0717	0.0922	0.2129	0.0553	0.2049	2.3369	3.1632	16.0978
B18DD4/B18DF7 Composite	Sandy Silt	11.20	56.52	32.28	0.00	0.0034	0.0069	0.0511	0.0634	0.1483	0.0380	0.1829	2.3349	2.5688	18.4349
B18DD5	Silt	23.87	72.68	3.55	0.00	0.0007	0.0019	0.0154	0.0208	0.0499	0.0120	0.2020	2.5392	3.3541	28.6919
B18DF5	Silt w/ Sand	9.33	68.49	22.28	0.00	0.0052	0.0067	0.0314	0.0479	0.0918	0.0274	0.2092	2.1526	1.4355	9.2755

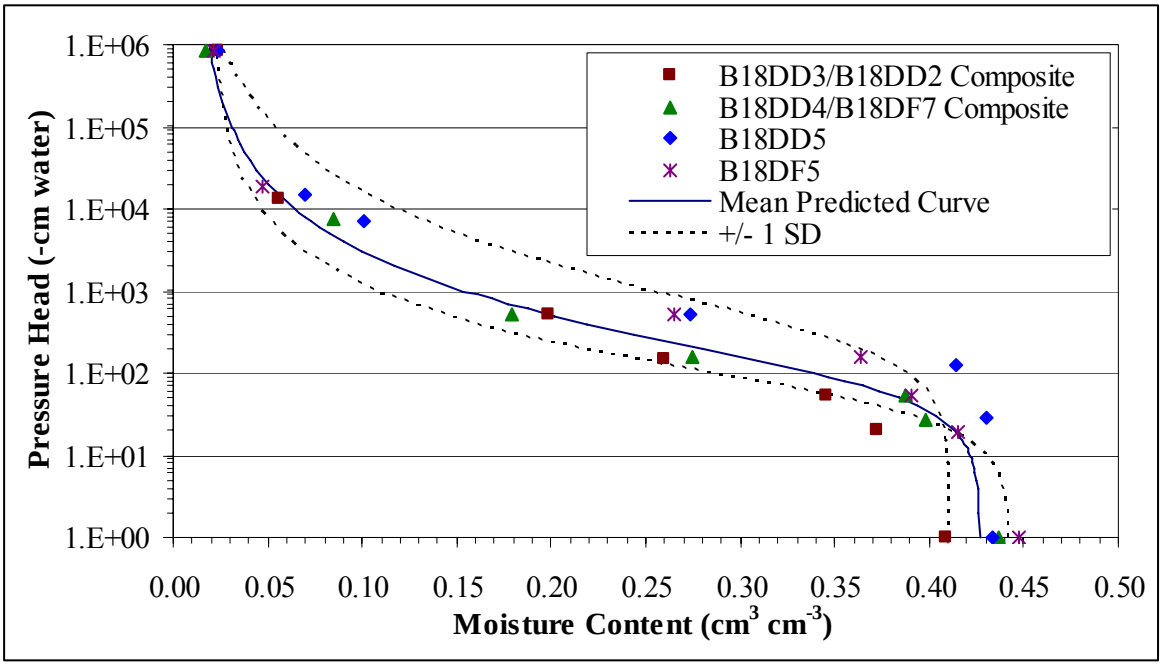

Figure 3.3. Measured and van Genuchten Model Predicted Water Characteristics Curve for the Silt Loam Soil. The predicted water characteristics curve represents the mean and one standard deviation van Genuchten parameters.

3.2 Silt Loam with Pea-Gravel Admixture

Figure 3.4 shows a plot of grain-size distribution for the borrow source silt loam samples as a hypothetical mixture containing 15 wt% of pea gravel. Warden silt loam, the fine soil used at the 200-BP-1 prototype barrier, is included for comparison. Table 3.3 compares the size statistics of hypothetical admixtures of silt loam and 15 wt% of pea gravel. The Warden silt-loam admixture is included for comparison.

Parameters for the silt loam-gravel admixture were calculated from the silt-loam parameters derived from measurements on the < 2-mm size fraction. To adjust the silt-loam parameters for a 15% by weight addition of pea gravel, the relationships of Bouwer and Rice (1983) were used. Although there have been no attempts to validate the accuracy of this correction method for local soils and sediments, there is precedent for its use to correct both hydraulic and geochemical properties of Hanford sediments (Khaleel and Freeman 1995; Meyer and Serne 1999). The water content of the admixture was calculated from the silt-loam water content and fraction of gravel as (Bouwer and Rice 1983)

$$\theta^{M} = (1 - F_g) \cdot \theta^{SiL} \tag{3.1}$$

where θ^{M} = volumetric water content of the silt loam-gravel admixture, ($m^3\ m^{-3}$)
θ^{SiL} = volumetric water content of the silt loam, ($m^3\ m^{-3}$)
F_g = volume fraction of gravel, i.e., the volume of gravel divided by the total volume of the silt loam-gravel admixture.

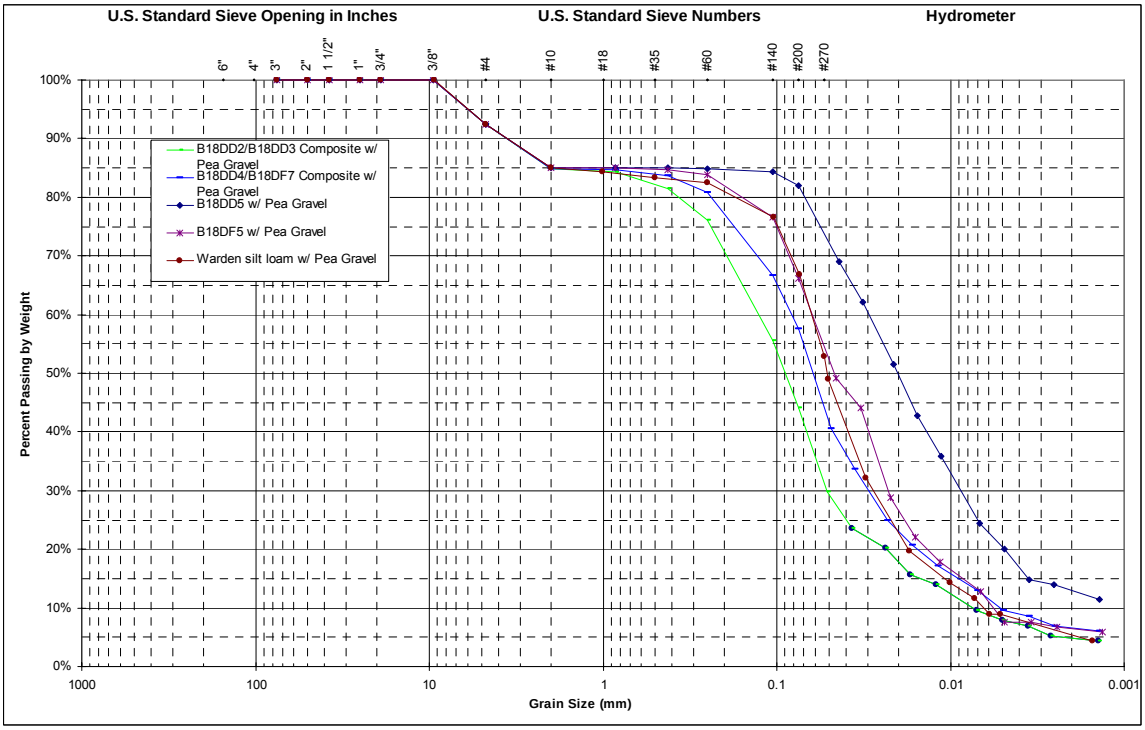

Figure 3.4. Particle Size Distribution Curves for Hypothetical Admixes of Silt Borrow Site Samples and 15% by Weight of Pea Gravel

The value of F_g is calculated by assuming that the gravel makes no contribution to the silt loam void space. This is not an unreasonable assumption as the secondary porosity associated with the gravel particles is quite small. The calculation is illustrated with a simple example of a 1000-g sample of silt loam-gravel admixture (Meyer and Serne 1999). The volume of silt loam is the ratio of silt loam mass (850 g) to silt loam bulk density (1.49 g/cm^3), or 570.47 cm^3. The silt-loam bulk density used is the average density reported by DBS[(a)]. The volume of gravel is the ratio of gravel mass (150 g) to gravel particle density (2.72 g/cm^3), or 55.1 cm^3. The gravel particle density used is the average density reported by Rockhold et al. (1993) for samples from a borehole adjacent to the ILAW disposal site. Using these values, the volume fraction of gravel in the silt loam-gravel admixture is F_g = 55.1/(55.1 + 570.47) = 0.08808. The dry bulk density of the admixture is 1.599 g/cm^3 calculated as [(850 +150)/(570.47 +55.1)]. The saturated hydraulic conductivity of the silt loam-gravel admixture can also be corrected for gravel using the relationship derived by Bouwer and Rice (1983).

$$K_s^M = (e^M / e^{SiL}) \cdot K_s^{SiL} \tag{3.2}$$

where K_s^M = saturated hydraulic conductivity of the silt loam-gravel admixture

K_s^{SiL} = saturated hydraulic conductivity of the silt loam

e^M = void ratios of the silt loam-gravel admixture

e^{SiL} = void ratios of the silt loam.

([a]) Daniel B. Stevens and Associates Incorporated. 2004. "Area C- Fine-grained Soils Characterization." Letter Report submitted to Fluor Hanford under Contract LB04.0220.00.

Table 3.3. Particle Size Statistics for Hypothetical Admixtures of the Silt Borrow Site Samples and 15% by Weight of Pea Gravel

Sample ID	USCS Texture	ASTM-D422 % Clay	ASTM-D422 % Silt	USCS % Sand	USCS % Coarse	D_{10} (mm)	D_{15} (mm)	D_{50} (mm)	D_{60} (mm)	D_{85} (mm)	Graphic Mean (mm)	Inclusive Graphic Standard Deviation (mm)	Sorting Index	C_c	C_u
B18DD2/B18DD3 Composite w/ Pea Gravel	Silty Sand	7.84	36.33	48.33	7.50	0.0074	0.0147	0.0894	0.1274	2.0195	0.1064	0.1165	2.4507	2.8009	17.1037
B18DD4/B18DF7 Composite w/ Pea Gravel	Sandy Silt	9.52	48.04	34.94	7.50	0.0052	0.0090	0.0618	0.0822	2.0233	0.0692	0.0945	2.7541	2.0207	15.6806
B18DD5 w/ Pea Gravel	Silt w/ Sand	20.29	61.77	10.43	7.50	0.0010	0.0035	0.0201	0.0295	0.8500	0.0197	0.0993	2.8340	2.5187	28.9405
B18DF5 w/ Pea Gravel	Sandy Silt	7.93	58.21	26.35	7.50	0.0057	0.0085	0.0465	0.0625	2.0000	0.0501	0.1066	2.3371	1.4553	11.0452
Warden Silt Loam w/ Pea Gravel	Sandy Silt	8.69	58.45	25.33	7.50	0.0064	0.0109	0.0512	0.0629	1.9990	0.0777	0.1034	2.1147	1.9002	9.7604

The void ratio is calculated from the soil porosity as $e = \phi/(1-\phi)$, where ϕ is the soil porosity. Using the particle and dry bulk densities listed in Table 3.4, and Eq. 2.7 for porosity, the second term of Eq. 3.2, e^{M}/e^{SiL} (0.7315/0.6267), gives a scaling factor of 0.8567. This approach was used to calculate scaling factors for all of the samples and ultimately scale the silt loam K_s to derive the value for the silt loam-gravel mixture. The water-content scale factor was applied to the water-retention function for the silt loam and the van Genuchten parameters refitted. The best-estimate van Genuchten (1980) parameters and their statistics are shown in Table 3.5. Plots of the measured water-retention data and retention curve predicted using the mean van Genuchten parameters and one standard deviation of the mean parameters are presented in Figure 3.5.

Table 3.4. Best-Estimate Parameter Values and Statistics for Silt Loam Soil

Sample ID	ρ_s (g cm^{-3})	ρ_b (g cm^{-3})	θ_s (m^3 m^{-3})	θ_r (m^3 m^{-3})	α (cm^{-1})	n (-)	K_s (cm/s)
B18DD3/B18DD2[(a)]	2.51	1.50	0.4048	0.0027	0.0197	1.3324	3.96E-05
B18DD4/B18DF7[(a)]	2.53	1.51	0.4374	0.0173	0.0161	1.4253	4.81E-05
B18DD5	2.48	1.49	0.4388	0.0214	0.0039	1.5284	1.80E-06
B18DF5	2.63	1.48	0.4266	0.0074	0.0049	1.4763	1.59E-05
Mean	2.54	1.50	0.4269	0.0122	0.0112	1.4406	1.53E-05
Standard Deviation	0.07	0.01	0.0157	0.0086	0.0079	0.0835	2.13E-05

(a) Composite samples

ρ_s is particle density, ρ_b is dry bulk density, θ_s is the saturated volumetric water content, θ_r is the residual volumetric water content, α and n are van Genuchten model fitting parameters, and K_s is saturated hydraulic conductivity.

Table 3.5. Best-Estimate Parameter Values and Statistics for Silt Loam with Pea Gravel

Silt Matrix Sample	ρ_s (g cm^{-3})	ρ_d (g cm^{-3})	θ_s (m^3 m^{-3})	θ_r (m^3 m^{-3})	α (cm^{-1})	n (-)	K_s (cm/s)
B18DD3/B18DD2[(a)]	2.53	1.61	0.369	0.0025	0.0197	1.3324	3.41E-05
B18DD4/B18DF7 [(a)]	2.55	1.62	0.3983	0.0158	0.0161	1.4255	4.13E-05
B18DD5	2.50	1.60	0.4003	0.0195	0.0039	1.528	1.55E-06
B18DF5	2.64	1.58	0.3893	0.0067	0.0049	1.4762	1.36E-05
Mean	2.56	1.60	0.3892	0.0111	0.0112	1.4405	1.31E-05
Standard Deviation	0.06	0.01	0.0143	0.0079	0.0079	0.0833	1.83E-05

(a) Composite samples

ρ_s is particle density, ρ_b is dry bulk density, θ_s is the saturated volumetric water content, θ_r is the residual volumetric water content, α and n are van Genuchten model fitting parameters, and K_s is saturated hydraulic conductivity.

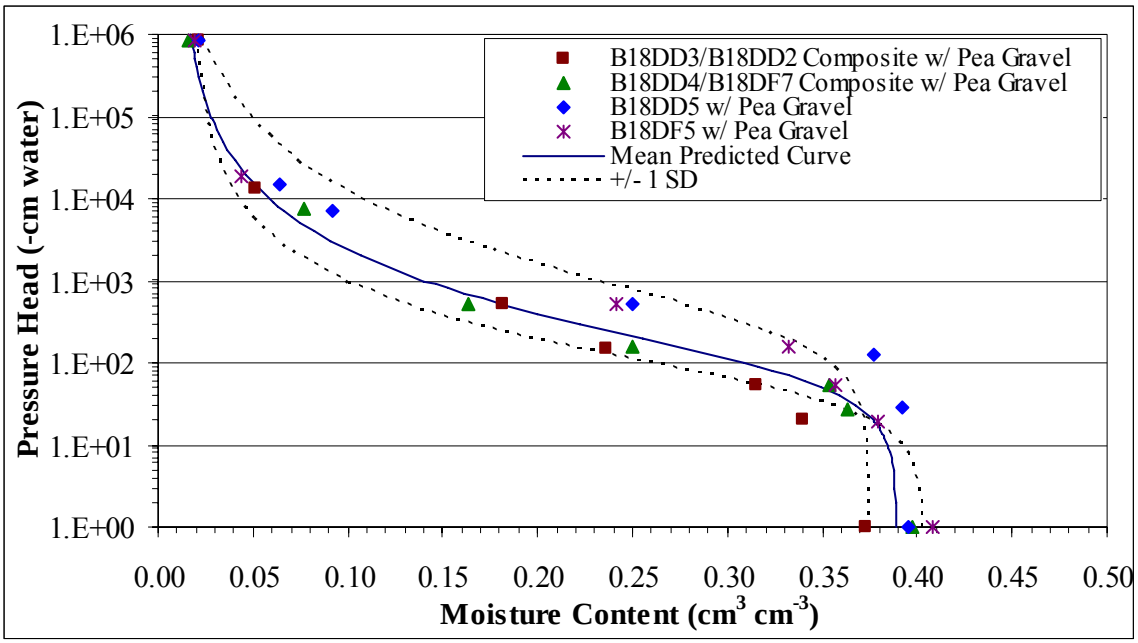

Figure 3.5. Measured and van Genuchten Model Predicted Water Characteristics Curve for the Silt-Loam Soil with Pea-Gravel Admixture. The predicted water-characteristics curve represents the mean and one standard deviation van Genuchten parameters.

3.3 Geotextile

Geotextile parameterization is based on literature data, primarily from Iryo and Rowe (2003) who compiled the main drying curves for 14 non-woven polypropylene geotextiles, including data published by Stormont et al. (1997). Moisture characteristic curves were measured on the geotextiles using the hanging water column method, the suction plate method of Klute (1986), or the capillary rise method. Measurements for the capillary rise method were performed by placing the base of a strip of geotextile into a reservoir of water and relating the moisture content at equilibrium of each geotextile segment to matric suction based on the segment height above the water basin. In addition to water-characteristic curves, the reported saturated transmissivity (T_s) and geotextile thickness (b) were used to calculate saturated hydraulic conductivity (K_s) using the relationship:

$$K_s = \frac{T_s}{b} \tag{3.3}$$

The data of Iryo and Rowe (2003) were fit to the van Genuchten (1980) and Brooks-Corey (1964) models to obtain model parameters for the geotextile fabrics.

Table 3.6 shows the geotextile properties presented by Iryo and Rowe (2003) and the soil hydraulic conductivity calculated according to Eq. (3.3). Also included are the fitted Brooks-Corey and van Genuchten parameters. Table 3.7 gives the means and standard deviations for the data presented in Table 3.5.

Table 3.6. Reported Geotextile Hydraulic Properties Including the fitted Brooks-Corey and van Genuchten Water-Retention Parameters for the 14 Geotextiles Characterized by Iryo and Rowe (2003)

Sample	Apparent Opening Size (mm)	Porosity (-)	T_s ($cm^2\ s^{-1}$)	K_s ($cm\ s^{-1}$)	θ_s ($cm^3\ cm^{-3}$)	Brooks-Corey			van Genuchten		
						θ_r[(a)] ($cm^3\ cm^{-3}$)	λ[(a)] (-)	h_b[(a)] (cm)	θ_r[(a)] ($cm^3\ cm^{-3}$)	α[(a)] (cm^{-1})	n[(a)] (-)
1	0.15	0.88	--	--	0.762	0.000	4.191	13.87	0.000	0.059	5.709
2	0.15	0.84	--	--	0.686	0.000	3.403	13.941	0.000	0.056	5.623
3	0.18	0.87	--	--	0.690	0.000	1.95	5.688	0.000	0.118	4.824
4	0.15	0.88	--	--	0.667	0.000	2.041	6.25	0.000	0.113	4.873
5	0.04	0.89	0.068	0.256	0.704	0.000	1.518	12.878	0.000	0.050	3.561
6	0.18	0.94	0.390	0.626	0.654	0.000	2.001	4.082	0.000	0.194	3.531
7	0.15	0.88	0.293	--	0.879	0.021	6.366	12.142	0.029	0.075	10.536
8	0.15	0.87	0.165	0.359	0.796	0.011	7.445	14.528	0.026	0.062	17.539
9	0.15	0.96	0.390	--	0.962	0.000	4.765	8.679	0.004	0.099	11.402
10	--	0.94	--	--	0.926	0.000	6.148	10.457	0.000	0.086	9.144
11	--	0.93	--	0.431	0.893	0.000	2.102	6.609	0.000	0.102	6.973
12	--	0.91	0.055	0.163	0.854	0.000	1.66	16.063	0.008	0.040	4.643
13	--	0.86	--	--	0.861	0.114	1.594	0.653	0.128	1.115	3.464
14	0.15	0.78	--	--	0.729	0.010	2.973	5.998	0.010	0.135	6.740

(a) Fitted value.

T_s is saturated transmissivity, K_s is the saturated hydraulic conductivity, θ_s is the saturated volumetric water content, θ_r is the residual volumetric water content, λ and h_b are Brooks-Corey model fitting parameters, and α and n are van Genuchten model fitting parameters.

Table 3.7. Best-Estimate Mean and Standard Deviation for Geotextile Hydraulic Properties and Fitted Water-Retention Characteristic Function Parameters

	T_s ($cm^2 s^{-1}$)	K_s ($cm\ s^{-1}$)	θ_s ($cm^3\ cm^{-3}$)	Brooks-Corey			van Genuchten		
				θ_r ($cm^3\ cm^{-3}$)	λ (-)	h_b (cm)	θ_r ($cm^3\ cm^{-3}$)	α (cm^{-1})	n (-)
Mean	0.174[(a)]	0.332[(a)]	0.785[(b)]	0.003[(b)]	3.582[(b)]	9.261[(a)]	0.006[(b)]	0.083[(a)]	6.538[(a)]
Standard Deviation	0.163	0.181	0.107	0.007	2.023	4.150	0.010	0.043	4.046

(a) Geometric Mean; (b) Arithmetic Mean
Sample 13 was excluded from the mean and standard deviation calculations.

Note that the fitted values of θ_r h_b, and α for Sample 13 are considerably different than those fitted for the other 13 geotextile samples. Based on this significant difference and its ability to erroneously skew the mean and standard deviation results, sample 13 was treated as an outlier and removed from the data set. Owing to the high porosity of the geotextiles, an average saturated water content of 0.785 $cm^3\ cm^{-3}$ was calculated.

Figure 3.6 shows the geotextile-water characteristic curves for the 14 samples characterized by Iryo and Rowe (2003) as well as the water-retention curves from the average of the fitted van Genuchten and Brooks-Corey parameters. To place these data in proper perspective in relation to geologic materials, the water-retention curve for a typical sandy soil is included. Due to the uniform pore size of the geotextile, a sharp transition from saturated to unsaturated conditions is observed, with air entry, h_b, occurring at a suction of about 9.3 cm. This value is similar to the sandy soil shown in Figure 3.6, but significantly less than the expected air entry pressure for a silt-loam soil. Because of the smaller pore size of the silt loam, an air entry pressure of 20 cm or higher can be expected. A major difference between the van Genuchten and Brooks-Corey models is evident near the inflection point associated with the air entry pressure. Because no air entry pressure is specified in the van Genuchten model, the curve is a smooth function. In contrast, the Brooks-Corey model requires specification of the air entry pressure, and a discontinuous function results. This is an important consideration in simulations that include a geotextile as its impact on flow in a layered system will depend on the choice of model for water retention.

3.4 Base Fill

The proposed source for the structural base-fill or grading-fill material is the spoil pile at Hanford's ERDF. The structural base-fill material is assumed to be a compacted ERDF spoil pile material. Figure 3.7 shows an aerial view of the ERDF spoil pile and the approximate locations where the samples were taken. Ten samples were collected on August 5, 2004, by digging to a specified depth and excavating bulk samples with a shovel.

Figure 3.6. Aerial Photograph of the Soil Spoil Pile at Hanford's ERDF, the Borrow Source for Structural Base Fill and Sand Capillary Break Materials, and Approximate Sample Locations

The samples were placed in 20-liter (5-gallon) buckets and sealed for transport and storage. Samples were taken to the laboratory and analyzed using the methods described in Section 2. Tests were conducted on samples compacted to 90 and 95 percent of maximum dry density (ASTM D698). The sample numbers and laboratory tests conducted on each sample are summarized in Table 3.8. Initial water contents were determined on the 10 samples and particle density on 4 samples. The mean antecedent water content was 0.059 g/g while the mean particle density was 2.68 g/cm^3. Results for the particle density and initial water contents are documented in Appendix B in Table B3.

Particle-size distributions were determined for the original 10 samples; a composite of all 10 samples (referred to as B1B382-385); B1B394 (a composite of 7 soils, excluding B1B382, B1B383, B1B385); and B1BRD4 (a composite of 4 west side samples B1B380, B1B381, B1B386, B1B387). Figure 3.8 shows a plot of the particle-size distributions for the 13 samples while the grain-size statistics are presented in Table 3.9. Particle-size analysis of the samples yielded USCS textures ranging from silty sand to well graded sand with silt (USDA loamy sand to sand). The percentage of sand (passing #4 sieve [4.75 mm] and retained on #200 sieve [0.075 mm]) ranged from 75.2% to 89.3%; silt (passing #200 sieve [0.074mm] to 0.075 mm) ranged from 7.3% to 15.2%; while clay (passing 0.005 mm) content ranged from 0.80% to 6.9%. Calculated D_{50} ranged from 0.22 mm to 0.60 mm.

Table 3.8. Sampling Depths and Laboratory Tests Performed for Base-Fill Soil

HEIS #	Boring #	Depth Interval Inches BGS	Initial Soil Properties w, ρ_b	K_{sat}	SMCC	GSD	SG	P	Notes
B1B380	1	12–24	X			X			
B1B381	2	12–24	X	X		X		X	
B1B382	3	12–24	X	X		X	X	X	
B1B383	4	12–24	X			X			
B1B383	4	12–24	X			X			
B1B384	5	12–30	X	X		X		X	
B1B385	6	12–24	X			X	X		
B1B386	7	12–24	X			X			
B1B387	8	12–24	X			X			
B1B388	9	12–24	X			X	X		
B1B389	10	12–36	X			X			
B1B382-385	NA	NA		X		X	X	X	Composite
B1B394	NA	NA		X	X	X		X	Composite
B1BRD4	NA	NA		X	X	X		X	Composite

W = Mass Wetness
ρ_b = Dry Bulk Density
K_{sat} = Saturated Hydraulic Conductivity
SMCC = Soil Moisture Characteristic Curve
GSD = Grain-Size Distribution
SG = Specific Gravity
P = Proctor Test

Three soils enveloping the range of the particle-size distributions, including the mid point, were selected for compaction tests. These were B1B382, B1B383, and B1B385 as well as a composite of the 10 samples (B1B382-385). Compaction tests were conducted according to ASTM D698-00A. The density data were fitted to a quadratic function on gravimetric water content using the SoilVision® fitting routines and estimates of the optimum moisture and maximum density determined.

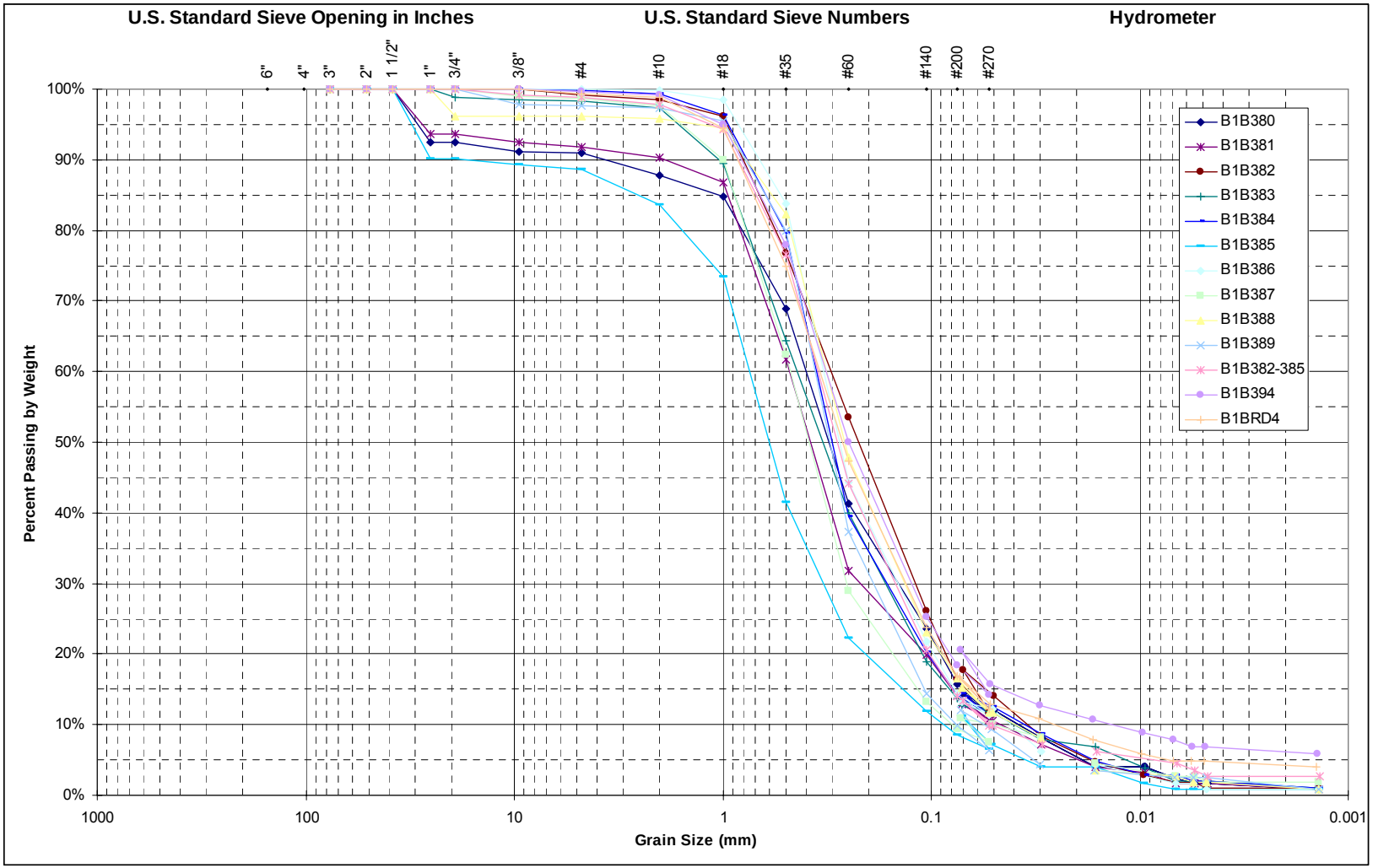

Figure 3.7. Particle-Size Distribution Curves for ERDF Spoil Pile Materials

Table 3.9. Particle-Size Statistics for ERDF Spoil Pile Sediments

Sample ID	USDA Texture	USCS Texture	ASTM-D422 % Clay	ASTM-D422 % Silt	USCS % Sand	USCS % Coarse	D_{10} (mm)	D_{15} (mm)	D_{50} (mm)	D_{60} (mm)	D85 (mm)	Graphic Mean (mm)	Graphic Standard Deviation (mm)	Sorting Index	C_c	C_u
B1B380	Sand	Silty sand	1.60	14.14	75.18	9.08	0.0412	0.0706	0.3105	0.3992	1.0614	0.2836	0.1741	2.3947	1.2703	9.6802
B1B381	Sand	Silty sand	1.61	12.45	77.80	8.14	0.0469	0.0793	0.3809	0.4802	0.9507	0.3096	0.1830	2.1672	2.1419	10.2381
B1B382	Sand	Silty sand	1.23	15.22	82.66	0.89	0.0394	0.0675	0.2245	0.3040	0.6724	0.2195	0.3147	2.1587	1.2007	7.7119
B1B383	Sand	Silty sand	1.95	11.83	84.48	1.74	0.0404	0.0814	0.3326	0.4418	0.8849	0.2920	0.2664	2.2238	1.5526	10.9363
B1B384	Sand	Silty sand	1.92	12.27	85.64	0.17	0.0397	0.0785	0.2999	0.3565	0.6255	0.2464	0.3315	1.8786	1.8941	8.9838
B1B385	Sand	Well-graded sand w/ silt	0.80	7.74	80.10	11.36	0.0874	0.1376	0.6019	0.7480	2.5380	0.5772	0.1859	2.0105	1.6760	8.5621
B1B386	Sand	Silty sand	1.16	13.20	85.61	0.03	0.0454	0.0773	0.2763	0.3295	0.5311	0.2246	0.3588	1.8932	1.4018	7.2543
B1B387	Sand	Well-graded sand w/ silt	2.12	7.27	89.28	1.32	0.0792	0.1168	0.3866	0.4757	0.8837	0.3451	0.3123	1.8466	1.7310	6.0041
B1B388	Sand	Silty sand	1.80	14.68	79.68	3.84	0.0401	0.0673	0.2613	0.3193	0.5825	0.2183	0.3183	1.9530	1.4139	7.9570
B1B389	Sand	Poorly-graded sand w/ silt	2.57	7.27	87.81	2.35	0.0759	0.1087	0.3074	0.3617	0.6277	0.2751	0.3999	1.7096	1.3193	4.7631
B1B394[(a)]	Loamy Sand	Silty sand	6.86	11.60	81.20	0.33	0.0134	0.0565	0.2495	0.3200	0.6650	0.2136	0.1739	2.1175	3.5681	23.7934
B1BRD4[(a)]	Sand	Silty sand	4.90	12.00	82.50	0.64	0.026	0.065	0.267	0.3436	0.715	0.23395	0.263038	2.139	1.971	13.3659
B1B382-385[(a)]	Sand	Silty sand	3.05	11.06	84.64	1.25	0.0537	0.0787	0.2837	0.3513	0.6951	0.2506	0.2939	1.9713	1.1849	6.5416

(a) Composite samples

Figure 3.9 shows plots of dry densities obtained at various moisture contents used in the compaction process based on the PNNL results. Table 3.10 presents the fitted parameters for the compaction curve. The mean of three (B1B382, B1B383, B1B385) values of optimum moisture was 0.136 g/g while the mean maximum dry density was 1.74 g/cm^3 (108.89 lb/ft^3). The optimum moisture for the composite B1B382-385 sample was 0.141 g/g while the maximum dry density was 1.71 g/cm^3 (106.47 lb/ft^3). Using the estimated maximum density values, preliminary saturated hydraulic conductivities were measured on samples B1B382, B1B383, B1B385, and B1B382-385 packed at 85% of maximum dry density. Table 3.11 gives the measured saturated hydraulic conductivities. Difficulties experienced in attaining a packing of 85% of the maximum density resulted in further measurements being performed at a minimum of 90% of maximum dry density.

Compaction tests were also performed on composite samples B1B394 and B1BRD4 by GeoEngineers in Tigard, Oregon. Figure 3.10 shows the observed data and the fitted curves. Table 3.10 also includes the results for the samples analyzed by GeoEngineers. The optimum moistures were 0.166 g/g and 0.195 g/g for B1B394 and B1BRD4, respectively. The maximum dry densities were 1.73 g/cm^3 (107.7 lb/ft^3) and 1.75 g/cm^3 (109.0 lb/ft^3), respectively. Even though the densities were quite comparable, the optimum moistures were somewhat different. Results for composite samples B1B394 and B1BRD4 were considered most representative and were used as the basis of subsequent testing and analyses.

Samples of B1B394 and B1BRD4 were packed into cores at densities equal to 90% and 95% of the maximum dry density determined in the compaction tests. Water retention and saturated hydraulic conductivities were measured on samples according to the procedures described in Chapter 2. The resulting water-retention data were fitted to the van Genuchten (1980) model, the parameters of which are given in Table 3.12. The saturated hydraulic conductivity value reported for each sample is the geometric mean of three values obtained from replicates of each sample. Both samples show a consistent decrease in saturated hydraulic conductivity as the density increased. The samples also showed an increase in saturated moisture content as density increased. This is somewhat counterintuitive as porosity typically decreases with increasing density. However, one possible explanation is a decrease in air-filled porosity with increasing density, which would result in a decrease in the amount of entrapped air. A decrease in entrapped air would result in a smaller discrepancy between the measured saturated water content and the sample porosity. Efforts were made to remove entrapped air from the samples while saturating, but results suggest that entrapped air may not have been completely evacuated. Plots of the measured water-retention data and retention curve predicted using the mean van Genuchten parameters and one standard deviation of the mean parameters for soils at 90 and 95 percent maximum dry density are presented in Figures 3.11 and 3.12.

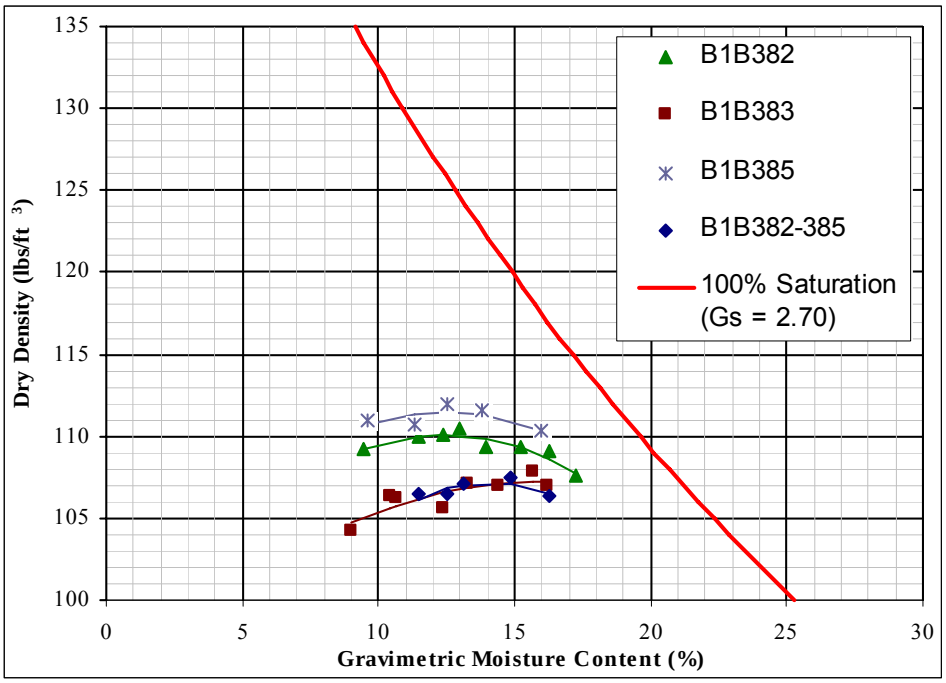

Figure 3.8. Dry Density-Water Content Curves for Samples B1B382, B1B383, B1B385, and B1B382-385 from the ERDF Spoil Pile

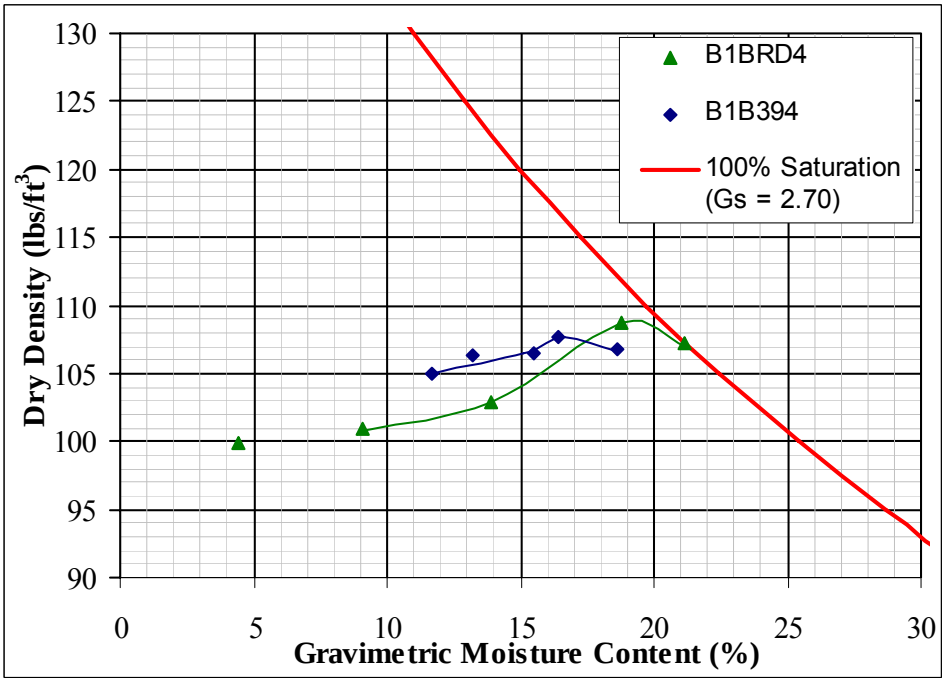

Figure 3.9. Dry Density-Water Content Curves for Composite Samples B1BRD4 and B1B394 from the ERDF Spoil Pile

Table 3.10. Static Compaction Characteristics for ERDF Spoil Pile Sediments

Sample ID	Maximum Dry Density, ρ_{bmax} (lb/ft^3)	Optimum Gravimetric Water Content θ_g (g/g)
B1B382	109.3	0.124
B1B383	106.5	0.161
B1B385	110.8	0.125
B1B382-385[(a)]	106.5	0.141
B1B3984[(a)]	107.7	0.166
B1BRD4[(a)]	109.0	0.195
(a) Composite samples.		

Table 3.11. Measured Particle Density and Saturated Hydraulic Conductivity for ERDF Samples Packed at 85% Maximum Dry Density. ρ_s is particle density, ρ_b is dry bulk density, and K_s is the saturated hydraulic conductivity.

Sample ID	ρ_s (g cm^{-3})	ρ_b (g cm^{-3})	K_s (cm/s)
B1B382	2.70	1.49	6.21E-01
B1B383	-	1.45	1.31E-01
B1B385	2.72	1.51	2.18E-01
B1B382-385	2.68	1.45	1.31E-01

Table 3.12. Best-fit Parameter Values and Statistics for ERDF Base Fill Samples at 90 and 95 Percent of Maximum Density

Sample ID	ρ_s (g cm^{-3})	ρ_d (g cm^{-3})	θ_s (m^3 m^{-3})	θ_r (m^3 m^{-3})	α (cm^{-1})	n (-)	K_s (cm/s)
B1B394 90% Max. Density	2.68	1.55	0.3716	0.0090	0.0234	2.2355	2.31E-02
B1BRD4 90% Max. Density	2.68	1.57	0.3494	0.0110	0.0161	2.9905	2.15E-02
Mean 90% Max. Density	2.68	1.56	0.3605	0.0100	0.0198	2.6130	2.23E-02
Stdev. 90% Max. Density	NA	0.01	0.0157	0.0014	0.0052	0.5339	1.13E-03
B1B394 95% Max. Density	2.68	1.64	0.3945	0.01	0.0191	2.4366	1.98E-02
B1BRD4 95% Max. Density	2.68	1.66	0.3716	0.011	0.0243	2.244	1.35E-02
Mean 95% Max. Density	2.68	1.65	0.3831	0.0105	0.0217	2.3403	1.63E-02
Stdev 95% Max. Density	NA	0.01	0.0162	0.0007	0.0037	0.1362	4.45E-03

Stdev= one standard deviation

ρ_s is particle density, ρ_b is dry bulk density, θ_s is the saturated volumetric water content, θ_r is the residual volumetric water content, α and n are van Genuchten model fitting parameters, and K_s is saturated hydraulic conductivity.

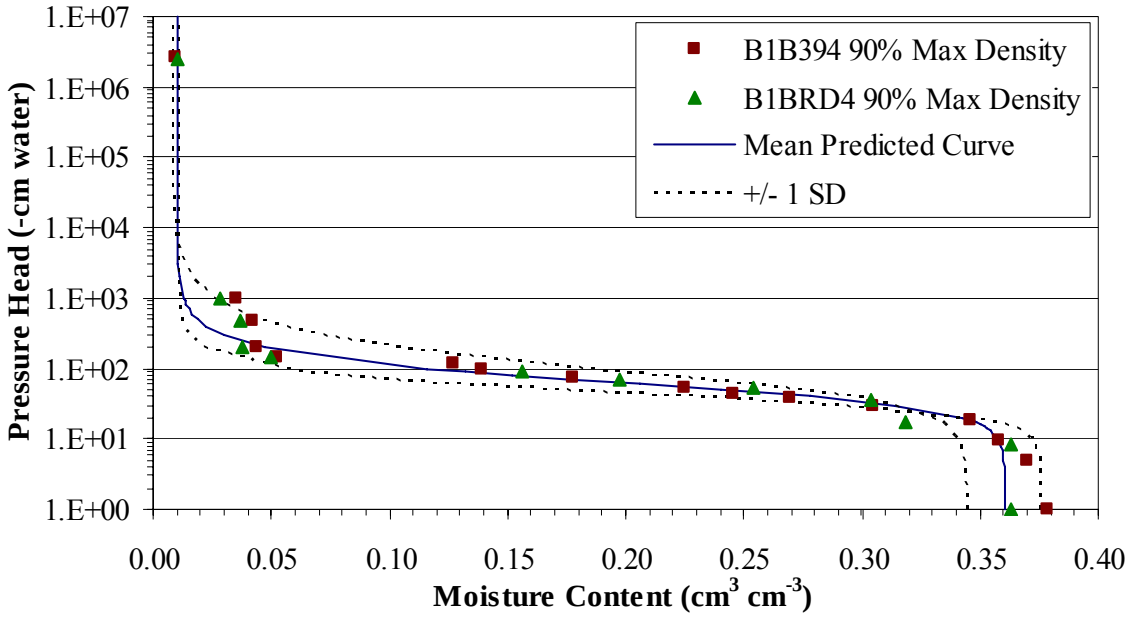

Figure 3.10. Measured and van Genuchten Model Predicted Water Retention Curve for the ERDF Structural Base Fill Soil at 90% Maximum Dry Density. The predicted water characteristics curve represents the mean and one standard deviation van Genuchten parameters.

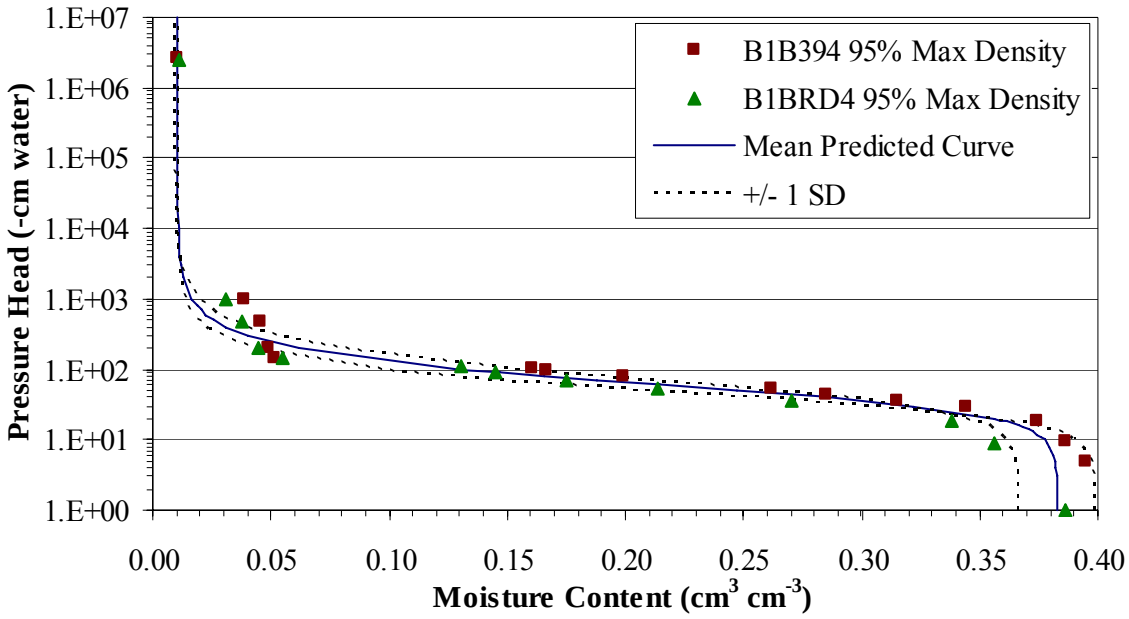

Figure 3.11. Measured and van Genuchten Model Predicted Water Retention Curve for the ERDF Structural Base Fill Soil at 95% Maximum Dry Density. The predicted water characteristics curve represents the mean and one standard deviation van Genuchten parameters.

3.5 Quarry Spalls

Quarry spalls are composed of angular broken stone, in this case basalt, free from segregation and meeting the size criteria in Table 3.13. The particle-size distribution is based on the specifications for quarry spalls as described in Section 9-13.6 of the Washington State Department of Transportation (WDOT) standard specifications (WDOT 2006). Quarry spalls will be used in constructing the protective side slopes. Properties of this material were estimated from the specified particle-size distribution using a combination of methods. Hydraulic properties were estimated using pedotransfer functions based on the model of Arya and Paris (1981).

Table 3.13. Particle-Size Distribution for Quarry Spalls Used to Estimate Water-Retention Parameters

Particle Diameter		Percent Passing
mm	inches	
200	8	100
75	3	40
19	0.75	5

Arya and Paris (1981) described a method to estimate the water retention from the particle-size distribution. The method is based on scaling the pore lengths in an idealized packing of spherical particles to those expected in a real porous medium. A scaling parameter is used to define the relationship between the total pore length in the idealized packing to that in the actual porous medium:

$$\alpha_i = \log(N_i) / \log(n_i) \tag{3.3}$$

where α = pore length scaling parameter
n_i = number of spherical particles in the idealized packing and
N_i = number of spherical particles required to trace the pore length in the corresponding real porous medium.

To obtain pairs of water content and matric potential needed to generate a water-retention curve, the continuous particle-size distribution of the porous medium is divided into *i* discrete fractions. Separate calculations are carried out for each fraction. The key part of the model is calculating the scaling parameter. For this, n_i is calculated first using:

$$n_i = \frac{3W_i}{4\pi\rho_s R_i^3} \tag{3.4}$$

where W_i is weight of the i^{th} particle size fraction, ρ_s is density of solids, and R_i is the mean particle radius for the i^{th} particle-size fraction. The parameter α_i is then calculated using Eq. 3.3. The matric potential for each pore size class is calculated as follows:

$$\psi_i = \frac{0.18}{R_i \sqrt{e\, n_i^{(1-\alpha_i)}}} \tag{3.5}$$

where *e* is void ratio. The corresponding water content for each pore size class is calculated as follows

$$\theta_i = \theta_s \cdot \sum_{j=1}^{j=i} W_j \qquad i = 1,2,\ldots,n \tag{3.6}$$

where θ_s is the saturated water content, and W_j is the j^{th} weight fraction of the soil particles. The $\theta(\psi)$ pairs may then be fitted to parametric models for water retention. The fitted parameters for the riprap are shown in Table 3.14. The porosity resulting from this analysis was 0.317 $m^3\ m^{-3}$. A plot of the quarry spalls retention curve predicted using van Genuchten parameters is presented in Figure 3.13.

Table 3.14. Best-Estimate Parameter Values for the Quarry Spalls material. ρ_s is particle density, ρ_b is dry bulk density, θ_s is the saturated volumetric water content, θ_r is the residual volumetric water content, α and *n* are van Genuchten model fitting parameters, and K_s is saturated hydraulic conductivity.

ρ_s ($g\ cm^{-3}$)	ρ_d ($g\ cm^{-3}$)	θ_s ($m^3\ m^{-3}$)	θ_r ($m^3\ m^{-3}$)	α (cm^{-1})	n (-)	K_s (cm/s)
2.86	1.95	0.318	0.0000	0.1059	4.570	144.4

3.6 Quarry Spalls with Silt Loam Matrix

The proposed barrier design incorporates a unique side slope configuration constructed from a composite of quarry spalls and silt loam (Figure 1.1). The composite is treated as a binary mixture with coarse packing at the critical packing volume, i.e., the composite is supported by quarry-spalls with all primary pore space filled with a silt loam. Parameters for the composite were calculated from the measured properties of the silt loam and the size-distribution information of the quarry spalls. In a coarse-packed system, fine particles fit within the voids created by the coarser grains. After estimating the porosity of the quarry spalls, an approach similar to that used for the silt loam-pea gravel admixture was then followed to adjust the known properties of the silt loam. The calculated porosity of the quarry spalls was 0.318 m^3 m^{-3}. The porosity resulting from these calculations is assumed to be occupied by silt loam in the silt loam-quarry spalls admixture. Figure 3.14 shows the grain size distribution for the admixture. The grain size statistics for the hypothetical quarry spalls and quarry spalls-silt loam admixture are given in Table 3.15.

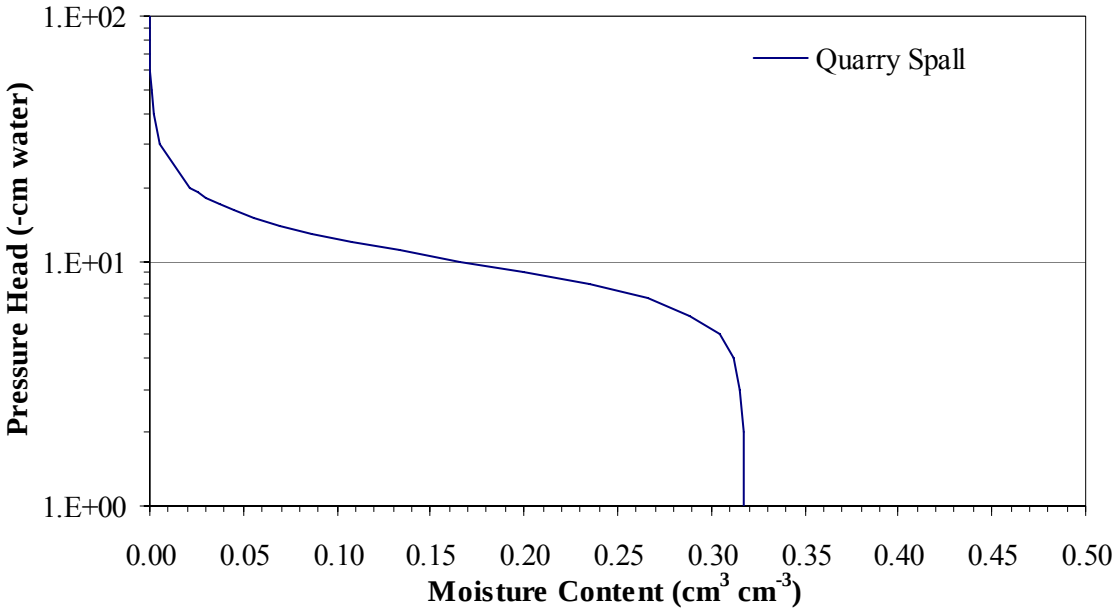

Figure 3.12. van Genuchten Model Predicted Water Characteristic Curve for Quarry Spalls

To adjust the silt-loam parameters for the quarry spalls, the relationships of Bouwer and Rice (1983) were also used. The calculation is illustrated with a simple example of a 1000-L sample of silt loam-quarry spalls composite. We know that 31.8 percent (porosity of quarry spalls) of the total volume or 318 L is occupied by silt loam. The remainder, 682 L, is occupied by the quarry spalls solids; thus F_g=0.682. Assuming a quarry-spalls particle density of 2.86 g/cm^3, the mass of quarry spalls is calculated as the product of the quarry-spalls particle density and quarry-spalls volume, or 1950.52 kg. Again assuming a silt-loam dry bulk density of 1.49 g/cm^3, the mass of silt loam is the product of the bulk density and the silt loam volume, or 473.82 kg. Therefore, the dry bulk density of the composite is 2.424 g/cm^3, calculated as [(1953.38 + 472.33)/ (683 + 317)].

The saturated hydraulic conductivity of the silt loam-quarry spalls composite was corrected for quarry-spalls content using the relationship derived by Bouwer and Rice (1983). Applying Eqs. 2.6 and 3.2 allowed the scaling factors for saturated hydraulic conductivity to be calculated. This approach was used to calculate scaling factors for all of the samples and ultimately scale the silt-loam K_s to derive the value for the silt loam-quarry spalls mixture. The water-content scale factor was applied to the water-retention function for the silt loam and the van Genuchten parameters refitted. The best-estimate van Genuchten (1980) parameters and their statistics are shown in Table 3.16. Plots of the measured water-retention data and retention curve predicted using the mean van Genuchten parameters, and one standard deviation of the mean parameters are presented in Figure 3.15.

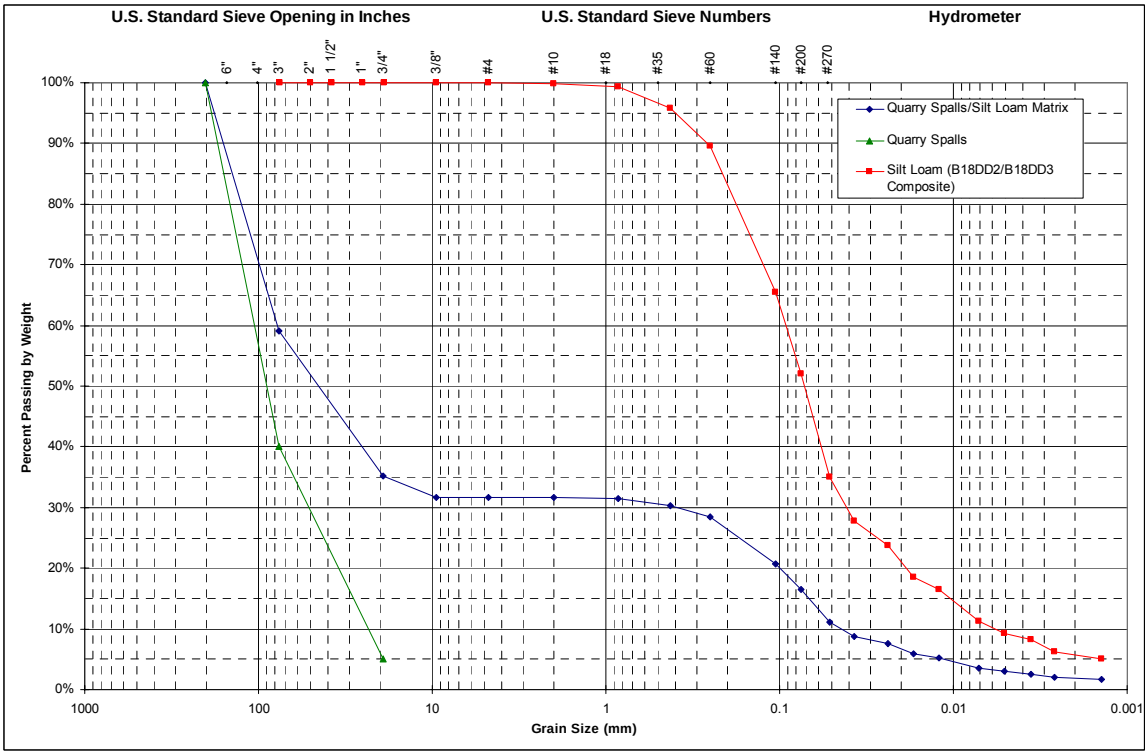

Figure 3.13. Particle-Size Distribution Curves for Quarry Spalls with Silt-Loam Composite

Table 3.15. Best-estimate Grain Size Statistics for the Quarry Spalls Materials

Sample ID	USCS Texture	ASTM D422 % Clay	ASTM D422 % Silt	USCS % Sand	USCS % Coarse	D_{10} (mm)	D_{15} (mm)	D_{50} (mm)	D_{60} (mm)	D_{85} (mm)	Graphic Mean (mm)	Graphic Standard Deviation (mm)	Sorting Index	C_c	C_u
Quarry Spalls	Well graded gravel	0.00	0.00	0.00	100.00	23.27	28.36	89.73	105.67	159.01	74.54	0.4663	1.7906	1.071	4.5401
Quarry Spalls/Silt Loam	Silty gravel w/ sand	2.93	13.54	15.23	68.30	0.044	0.068	45.20	78.01	141.91	7.69	0.0349	25.547	0.043	1780.8

Table 3.16. Best-Estimate Parameter Values for the Quarry Spalls with a Silt Loam Matrix

Silt Admixture Sample	ρ_s (g cm^{-3})	ρ_b (g cm^{-3})	θ_s (m^3 m^{-3})	θ_r (m^3 m^{-3})	α (cm^{-1})	n (-)	K_s (cm/s)
B18DD3/B18DD2[(a)]	2.75	2.43	0.1282	0.0025	0.0197	1.3324	8.584E-06
B18DD4/B18DF7 [(a)]	2.76	2.43	0.1279	0.0158	0.0161	1.4255	1.043E-05
B18DD5	2.74	2.43	0.1257	0.0195	0.0039	1.528	3.930E-07
B18DF5	2.79	2.42	0.1393	0.0067	0.0049	1.4762	3.279E-06
Mean	2.76	2.43	0.1302	0.0111	0.0112	1.4405	3.277E-06
Standard Deviation	0.02	0.00	0.0061	0.0079	0.0079	0.0833	4.645E-06

(a) Composite samples.

ρ_s is particle density, ρ_b is dry bulk density, θ_s is the saturated volumetric water content, θ_r is the residual volumetric water content, α and n are van Genuchten model fitting parameters, and K_s is saturated hydraulic conductivity.

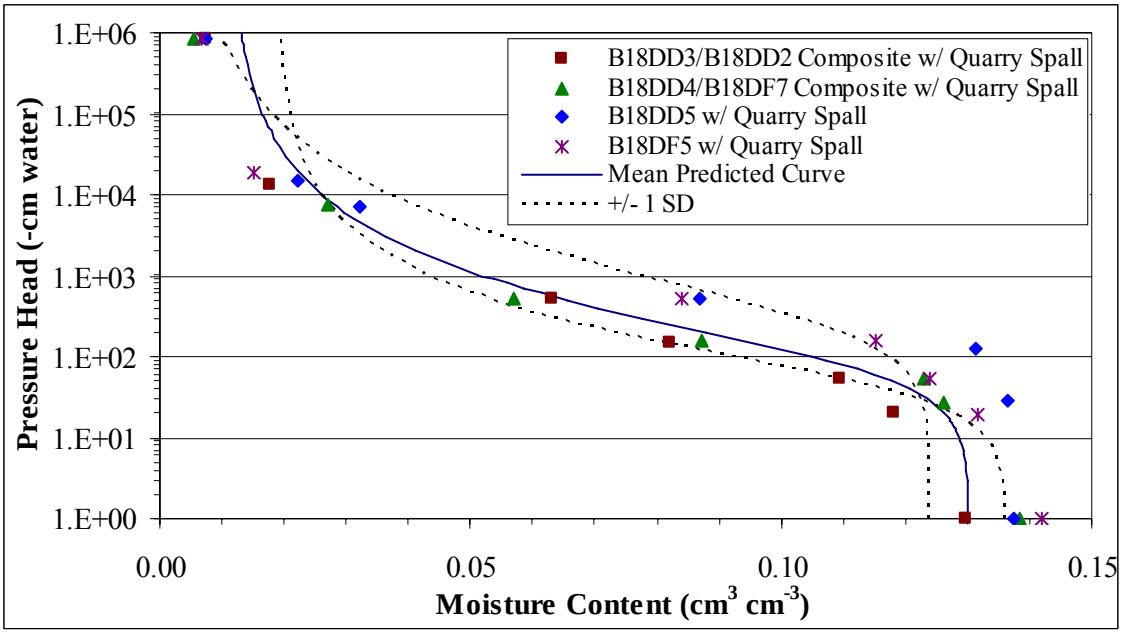

Figure 3.14. Measured and van Genuchten Model Predicted Water Retention for the Quarry Spalls with a Silt Loam Matrix. The Predicted Water-Retention Curve Represents the Mean and one Standard Deviation in the van Genuchten Parameters.

3.7 ASTM C-33 Aggregates

One of the candidate designs includes a capillary break. In engineered barriers, capillary breaks have been shown to increase the storage capacity of the fine soil layer and limit down migration of water by increasing lateral flow. To enhance the lateral diversion water, the material comprising the capillary break must meet very specific gradation requirements. The material proposed for use in the capillary break is required to meet the specifications of ASTM C33 (ASTM 2006). ASTM C33-03 defines the requirements for grading and quality of fine and coarse aggregate (other than lightweight or heavyweight aggregate) for use in concrete. This specification is typically used by a contractor, concrete supplier, or other purchaser as part of the purchase document describing the material to be furnished.

The fine aggregate specifications were selected for the capillary break material. According to ASTM C30-03, fine aggregate should consist of natural sand, manufactured sand, or a combination graded with the limits shown in Table 3.17. Specifications for a custom blend of sample B1F3D4 were developed based on the C33 limits and are also shown in Table 3.17. The custom blend called for not more than 3% by weight of sediment passing the 75 μm (No. 200) sieve.

Table 3.17. Sieve Analysis for Fine Aggregate Meeting ASTM C33 Specifications

Sieve Size	Percent Passing by Weight	
	ASTM C33-03	**Custom Blend**
9.5-mm (3/8-in)	100	100
4.75-mm (No. 4)	95 to 100	100
2.36-mm (No. 8)	80 to 100	100
1.18-mm (No. 16)	50 to 85	85
600-μm (No. 30)	25 to 60	60
300-μm (No. 50)	5 to 30	30
150-μm (No. 100)	0 to 10	10
75-μm (No. 200)[†]	NA	3[(a)]
(a) Maximum 3%		

Sample B1F3D4 was dry sieved and blended, according to Table 3.17, by DBS[(a)] The sample was compacted to 80%, 90%, and 95% of maximum dry density, corresponding to 1.40 g/cm^3, 1.58 g/cm^3, and 1.66 g/cm^3 for measuring hydraulic properties. Figure 3.15 is a plot of the particle-size distribution of the custom blend and composite of sample B1F3D4. The grain-size distribution statistics are shown in Table 3.18. Both samples are considered to be poorly graded sand under the USCS whereas they are considered as sands under the USDA classification system. Published data for an ASTM C33 fine aggregate with rounded particles show a C_u of 3.9 and a C_c of 0.9. The measured C_u of the custom blend is 3.9 whereas the C_c is 0.97, both of which compare well with published values of the ASTM C33 fine aggregate. These results suggest that the custom-blended ERDF spoil pile samples can meet the gradation requirements needed for a capillary break material.

Hydraulic properties, including water retention and saturated hydraulic conductivity, were also measured for the custom blend (Figure 3.16). Measured water-retention data were fitted to the van Genuchten function and the parameters used to predict the unsaturated hydraulic conductivity. Table 3.19 summarizes the estimated water-retention parameters for the van Genuchten model for the remolded samples as reported by DBS[(a)]. Saturated hydraulic conductivity and porosity were corrected for gravel content when necessary. Remolded samples were observed to settle significantly during measurement of saturated hydraulic conductivity and continued to settle throughout testing as reported by DBS[(a)]. Hydraulic properties are therefore reported as 80%, 90%, and 95% of the measured settled density (MSD).

([a]) Daniel B. Stevens and Associates Incorporated. 2004. "Area C- Fine-grained Soils Characterization." Letter Report submitted to Fluor Hanford.

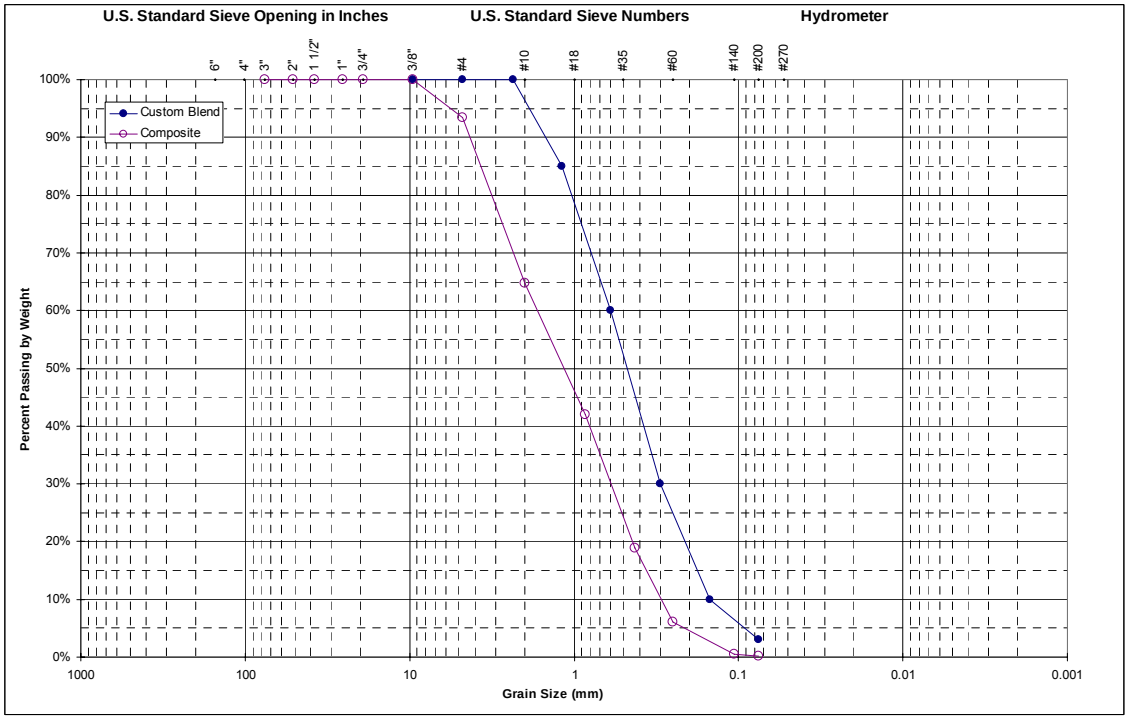

Figure 3.15. Particle-Size Distribution Curves for Sample B1F3D4 Custom Blend and Composite

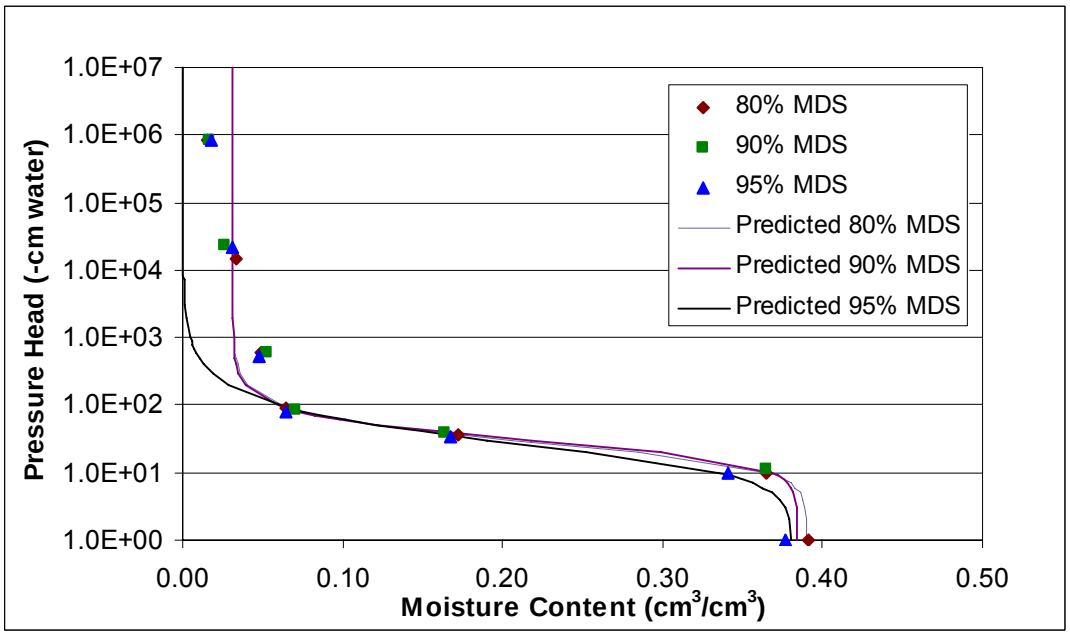

Figure 3.16. Measured and van Genuchten Model Predicted Water Retention for B1F3D4 Custom Blended to Meet ASTM C33 Specifications. The Predicted Water-Retention Curves are Based on the Fitted Parameters.

The capability of the ASTM C33 aggregate to function as a capillary break depends partly on the difference in air entry pressure relative to the silt loam admixture and silt-loam soils. The ideal situation is one in which the C33 has a smaller air entry pressure (larger α) than the overlying fine-textured soil. The α parameter values for the silt loam reported in Table 3.16 range from 0.0049 to 0.0197 cm^{-1} with a mean of 0.011 cm^{-1}. The means value of α corresponds to an air entry pressure of about 90 cm. The mean value of α for the custom blend is 0.0462 cm^{-1}, corresponding to an air entry pressure of 21.6 cm. These results also suggest that the custom-blended ERDF spoil pile sample may meet the hydrologic requirements of a capillary break.

3.8 Biointrusion Barrier Layer

A rock layer to minimize root and animal intrusion has been proposed for the 216-U-1/2 and 216-U-8 barrier design. The deepest barrier layer is therefore a 16-inch-thick biointrusion layer constructed from coarse rock with a graded filter to prevent the migration of the finer ERDF sand (compacted grading fill layer) into the coarse rock. The first 30 cm (12 inches) is comprised of a minimum of 2.5" minimum crushed ballast overlain by 4 inches (10 cm) of ¾" minimum crushed gravel. The WDOT specifications meeting these criteria are "Shoulder Ballast" per WSDOT M41-10, DOT 9-30.9(2), and "Crushed Surfacing Gravel, Top Course and Keystone" per DOT 9-03.9(3). The grading requirements for shoulder ballast and crushed surfacing gravel are shown in Table 3.20. For the crushed gravel, there is a requirement that the sand equivalent be a minimum of 35% by weight.

Table 3.18. Best-Estimate Grain Size Statistics for the Custom Blended ERDF Spoil Pile Sediments used to Generate the ASTM C33 Soil

Sample ID	ASTM-D422	USCS		D_{10} (mm)	D_{15} (mm)	D_{50} (mm)	D_{60} (mm)	D_{85} (mm)	Graphic Mean (mm)	Graphic Standard Deviation (mm)	Sorting Index	C_c	C_u
	% Fines	% Sand	% Coarse										
B1B394	18.46	81.20	0.33	0.013	0.057	0.249	0.320	0.665	0.214	0.174	2.118	3.568	23.793
B1BRD4	16.90	82.50	0.64	0.026	0.065	0.267	0.344	0.715	0.234	0.263	2.139	1.971	13.366
Composite[(a)]	1.33	88.36	10.27	0.298	0.408	1.111	1.442	3.346	0.325	0.361	2.006	1.012	4.839
Custom Blend[(a)]	2.88	96.34	0.78	0.158	0.205	0.442	0.534	0.976	0.687	0.766	1.672	1.058	3.384
(a) Composite and custom blend of dry-sieved B1B394.													

Table 3.19. Best-Estimate Parameter Values for the Quarry Spalls with a Silt Loam Matrix

Silt Admixture Sample	ρ_s (g cm^{-3})	ρ_b (g cm^{-3})	θ_s (m^3 m^{-3})	θ_r (m^3 m^{-3})	α (cm^{-1})	n (-)	K_s (cm/s)
B1F3D4 Composite[(a)]	2.65	1.83	0.3240	0.0260	0.0213	2.721	6.4E-02
B1F3D4 Composite[(b)]	2.65	1.83	0.3504	0.0298	0.0609	2.561	3.4E-02
B1F3D4 Composite[(c)]	2.65	1.85	0.3383	0.0312	0.0519	3.270	3.7E-02
B1F3D4 Custom Blend[(a)]	2.75	1.72	0.3901	0.0311	0.0449	2.635	4.3E-02
B1F3D4 Custom Blend[(a)]	2.75	1.78	0.3842	0.0314	0.0401	2.829	4.5E-02
B1F3D4 Custom Blend[(a)]	2.75	1.75	0.3811	0.0000	0.0548	2.076	2.7E-02

(a) 80% measured settled density, (b) 90% measured settled density, (c) 95% measured settled density
ρ_s is particle density, ρ_b is dry bulk density, θ_s is the saturated volumetric water content, θ_r is the residual volumetric water content, α and n are van Genuchten model fitting parameters, and K_s is saturated hydraulic conductivity.

Table 3.20. Sieve Analysis for Fine Aggregate Meeting ASTM C33 Specifications

Sieve Size	Percent Passing	
	Shoulder Ballast	**Crushed Gravel**
63-mm (2 1/2-in)	100	
31.5-mm		100
19-mm (3/4 -in)	40–80	
16-mm (5/8-in)		50–80
6.3-mm (1/4-in)	5 max	30–50
425-µm (No. 40)		3–18
150-µm (No. 100)	0–2	
75-µm (No. 200)		75 min.

Accounting for the effects of this layer in barrier hydrologic performance requires knowledge of the hydraulic properties. However, these data were not readily available, and properties were therefore estimated from available information. Hydraulic properties were estimated for the crushed basalt and gravel by pedotransfer functions based on the approach of Arya and Paris (1981). The first step in estimating the properties was to generate a particle-size distribution based on the WDOT specifications. To obtain the pairs of water content and matric potential needed to generate a water-retention curve, a continuous function was fitted to the particle-size distribution for each material. The plot of the expected particle-size distribution for crushed basalt and crushed gravel is shown in Figure 3.17 based on the upper end of the ranges shown in Table 3.20. The size statistics are summarized in Table 3.21.

Based on the size distribution, the crushed basalt is classified as a poorly graded gravel according to USCS whereas the crushed gravel is classified as well graded sand with silt and gravel. Porosity was estimated using the expected packing density and the particle density of local basaltic materials. Predicted hydraulic properties are summarized in Table 3.22 whereas the functions are shown in Figure 3.18 and Figure 3.19.

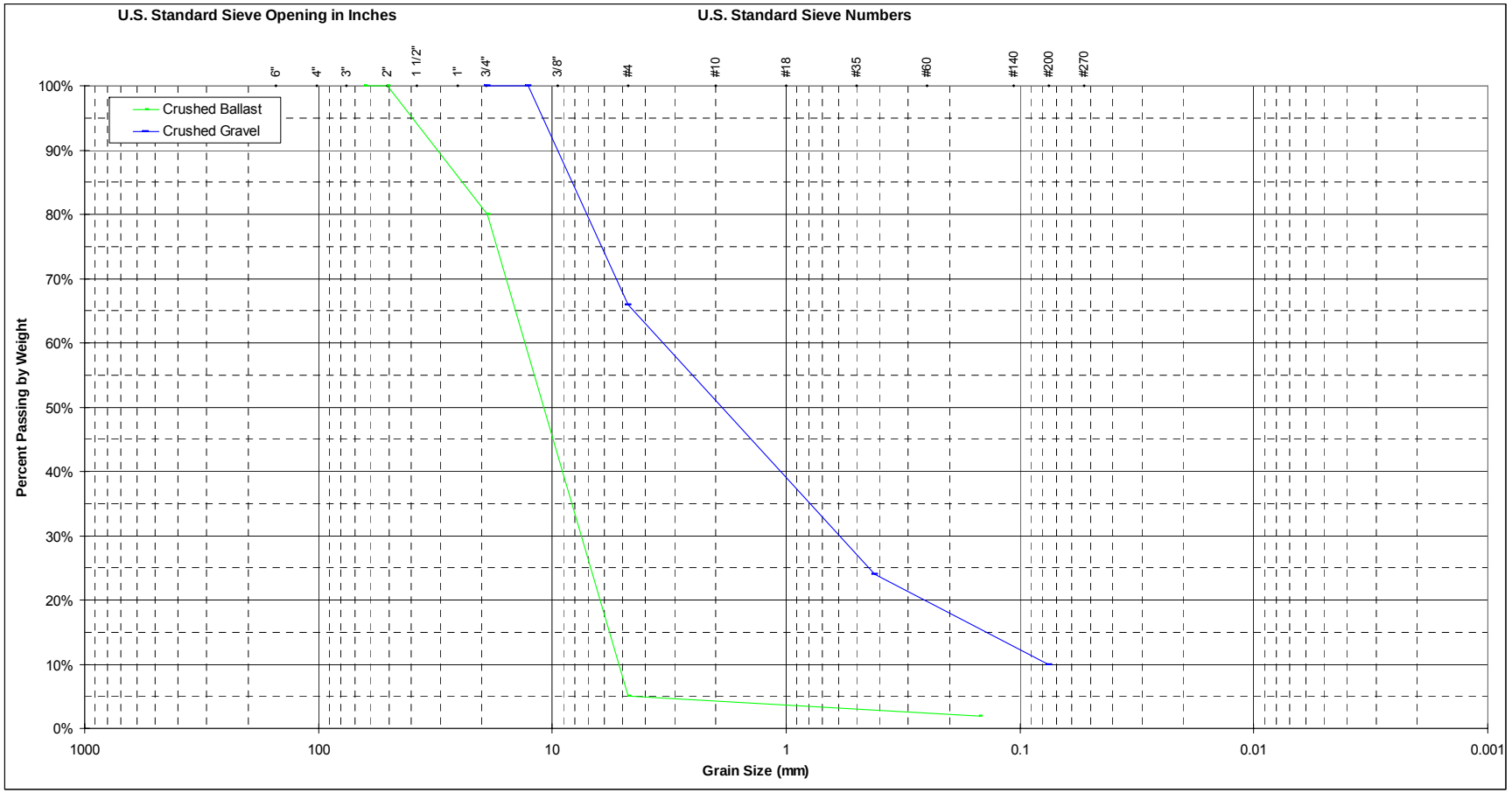

Figure 3.17. Particle-Size Distribution for the Crushed Basalt and Crushed Gravel Based on WDOT Specifications

Table 3.21. Grain-Size Statistics for Crushed Ballast and Crushed Gravel Based on WDOT Specifications

Sample ID	USCS Texture	USCS % Fines	USCS % Sand	USCS % Gravel	D_{10} (mm)	D_{15} (mm)	D_{50} (mm)	D_{60} (mm)	D_{85} (mm)	Graphic Mean (mm)	Inclusive Graphic Standard Deviation (mm)	Sorting Index	C_c	C_u
Crushed Ballast	Poorly Graded Gravel	2.00	3.00	95.00	5.2108	5.7164	10.9299	13.1535	24.3437	11.3838	0.5131	1.5888	0.8309	2.5243
Crushed Gravel	Well Graded Sand w/ Silt and Gravel	10.00	56.00	34.00	0.075	0.1388	1.8853	3.3589	8.2295	1.3324	0.1602	3.7214	1.4003	44.7858

Table 3.22. Estimated Saturated Conductivity, van Genuchten, and Brooks Corey Model Parameters for Crushed Ballast and Crushed Gravel

Sample	ρ_s (g/cm^3)	ρ_b (g/cm^3)	Porosity (cm^3/cm^3)	K_s (cm/s)	Van Genuchten Parameters				Brooks Corey Parameters			
					θ_s ($cm^3\,cm^{-3}$)	θ_r ($cm^3\,cm^{-3}$)	α (cm^{-1})	n (-)	θ_s ($cm^3\,cm^{-3}$)	θ_r ($cm^3\,cm^{-3}$)	ψ_b (cm)	λ (-)
Crushed Ballast	2.86	1.95	0.3182	7.134	0.2795	0.0000	38.7397	2.0421	0.2686	0.0018	0.0246	1.0577
Crushed Ballast	2.86	1.85	0.3531	10.840	0.3102	0.0000	41.9010	2.0421	0.2982	0.0000	0.0225	1.0318
Crushed Gravel	2.86	1.95	0.3182	0.109	0.2915	0.0000	28.8759	1.2640	0.2860	0.0000	0.0260	0.2428
Crushed Gravel	2.86	1.85	0.3531	0.166	0.3236	0.0000	31.2321	1.2640	0.3174	0.0000	0.0241	0.2428

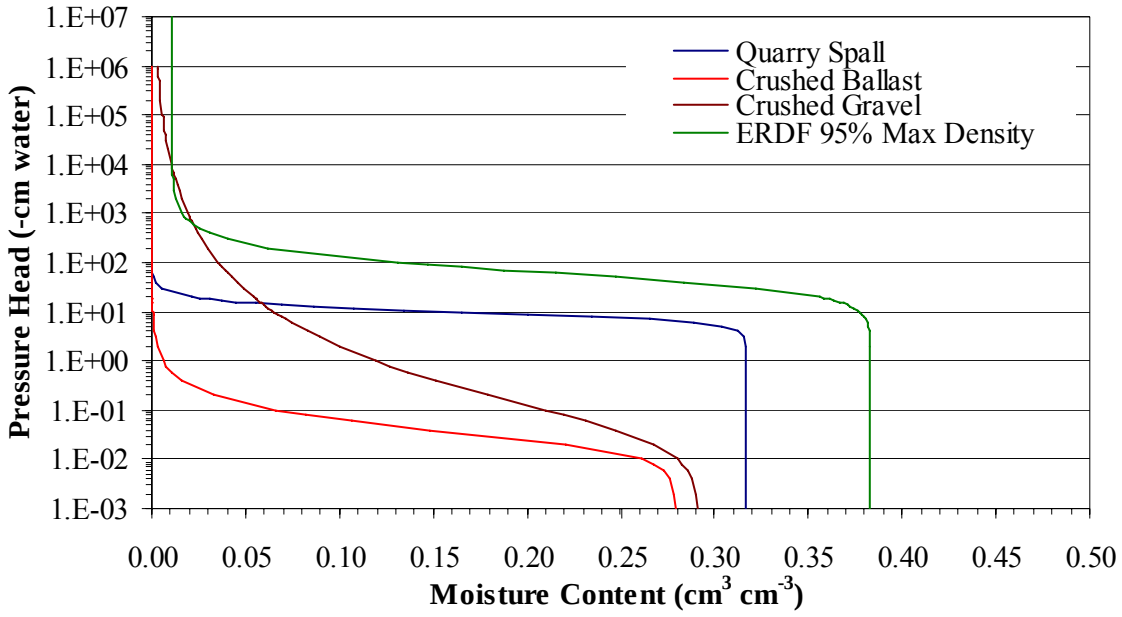

Figure 3.18. Soil Water Retention Curves for Crushed Ballast and Crushed Gravel, Each at a Bulk Density of 1.95 g/cm^3, Quarry Spalls, and ERDF Soil at 95% Maximum Density

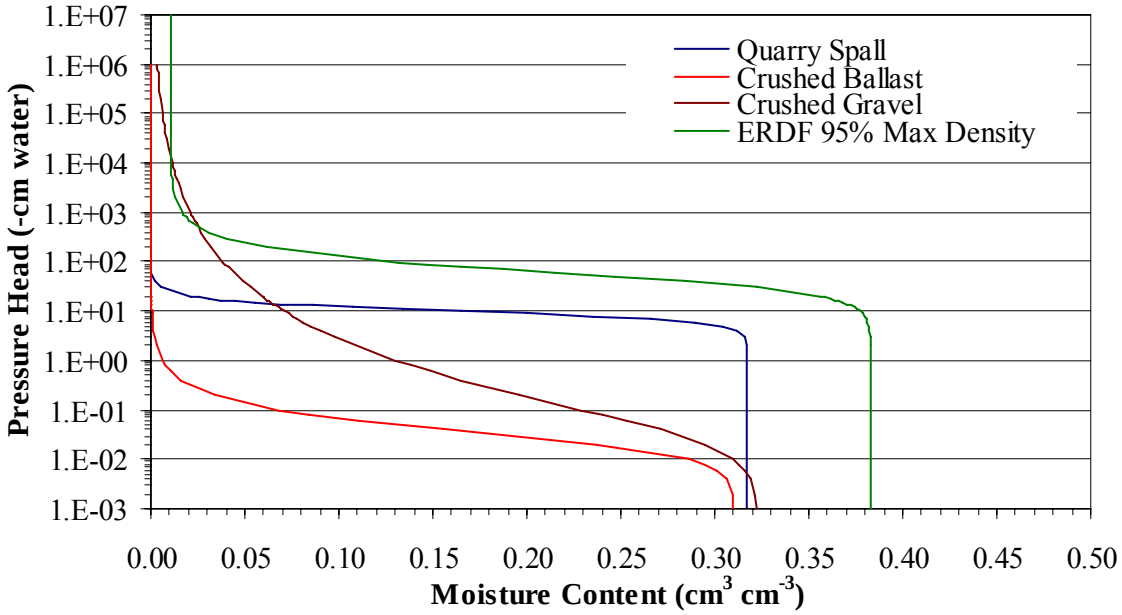

Figure 3.19. Soil Water Characteristic Curves for Crushed Ballast and Crushed Gravel, Each at a Bulk Density of 1.85 g/cm^3, Quarry Spalls, and ERDF Soil at 95% Maximum Density

Because of the coarse texture of the materials, the residual moisture content, θ_r, was assumed to be zero. The coarse texture is also responsible for the large estimates of the van Genuchten α parameter. The inverse of the α parameter is a measure of the air entry pressure, which was also calculated using the Brooks-Corey model. Estimated air entry values are all less than 1 cm (Table 3.22). This will have implications for the functioning of the biointrusion layer. The large difference in α relative to the sand above will result in the formation of a capillary break. This would help to improve the water-control function of the barrier.

Animal and plant root intrusion into buried waste is a concern in the design of engineered barriers. The efficacy of the proposed design in controlling root penetration, however, cannot be assessed at this point. There is evidence of limitations on root penetration by rock layers from clear-tube lysimeters and excavations at Hanford's Field Lysimeter Test Facility (FLTF). Excavated lysimeters did not reveal roots below the capillary break from fractured basalt. These results suggest that if the biointrusion layer and the sediment immediately above it are consistently dry, roots will not penetrate. However, any condition that leads to the long-term wetting of even the faces of the rock could result in some root penetration. A number of products derived from porous nonwoven, polypropylene geotextile fabric with permanently attached nodules containing slow-release herbicide are currently available to control root growth. These materials could be used to supplement the efficacy of the biointrusion layer.

3.9 Summary

Best-estimate values for the hydraulic parameters of the soil and geotechnical materials to be used in the performance-assessment analyses of the candidate barriers were presented. Moisture-retention characteristics and saturated hydraulic conductivity were directly measured for the ERDF spoil pile soils and the silt loam borrow-source soils. Hydraulic properties for the silt loam-pea gravel admixture and composite of quarry spalls and silt loam were estimated by adjusting the silt-loam parameters by the weight addition of pea gravel or rock material following the relationships of Bouwer and Rice (1983). Geotextile hydraulic properties were compiled from data reported in the literature. Hydraulic properties for quarry spalls, which will be used to construct the side slopes, and for crushed gravel and crushed basalt, to be used in construction of the biointrusion layer, were estimated from specified particle-size distributions using pedotransfer functions based on the model of Arya and Paris (1981).

A summary of Brooks-Corey and van Genuchten parameters along with saturated hydraulic conductivity, particle density, and dry density for the rocks and soils of interest are given in Table 3.23. A comparison of the water-retention curves for the silt loam, silt loam with pea gravel admixture, geotextile, and ERDF soils predicted using the mean van Genuchten parameters is presented in Figure 3.20. Figure 3.21 gives a plot of retention curves for the quarry spalls and silt loam-quarry spalls composite.

Table 3.23. Best-Fit Parameter Values and Statistics for Soil Materials

Sample	ρ_s (g cm^{-3})	ρ_b (g cm^{-3})	K_s (cm/s)	Brooks-Corey θ_s (cm^3 cm^{-3})	Brooks-Corey θ_r (cm^3 cm^{-3})	Brooks-Corey λ (-)	Brooks-Corey h_b (cm)	van Genuchten θ_s (cm^3 cm^{-3})	van Genuchten θ_r (cm^3 cm^{-3})	van Genuchten α (cm^{-1})	van Genuchten n (-)
Silt Loam											
B18DD3/B18DD2	2.51	1.50	3.96E-05	0.3754	0.0233	0.3714	56.9152	0.4048	0.0027	0.0197	1.3324
B18DD4/B18DF7	2.53	1.51	4.81E-05	0.4362	0.0176	0.2933	24.6731	0.4374	0.0173	0.0161	1.4253
B18DD5	2.48	1.49	1.80E-06	0.4260	0.0233	0.4736	187.9699	0.4388	0.0214	0.0039	1.5284
B18DF5	2.63	1.48	1.59E-05	0.4181	0.0213	0.4092	117.5088	0.4266	0.0074	0.0049	1.4763
Mean	2.54	1.50	1.53E-05	0.4139	0.0214	0.3869	96.7668	0.4269	0.0122	0.0112	1.4406
Standard Deviation	0.07	0.01	2.13E-05	0.0267	0.0027	0.0753	71.9581	0.0157	0.0086	0.0079	0.0835
Silt Loam with Pea Gravel Admixture											
B18DD3/B18DD2	2.53	1.61	3.41E-05	0.3422	0.0213	0.3717	57.0125	0.3690	0.0025	0.0197	1.3324
B18DD4/B18DF7	2.55	1.62	4.13E-05	0.3973	0.0160	0.2917	24.3605	0.3983	0.0158	0.0161	1.4255
B18DD5	2.50	1.60	1.55E-06	0.3938	0.0213	0.3967	120.4819	0.4003	0.0195	0.0039	1.5280
B18DF5	2.64	1.58	1.36E-05	0.3691	0.0194	0.6248	246.3054	0.3893	0.0067	0.0049	1.4762
Mean	2.56	1.60	1.31E-05	0.3756	0.0195	0.4212	112.0401	0.3892	0.0111	0.0112	1.4405
Std. Deviation	0.06	0.01	1.83E-05	0.0255	0.0025	0.1429	98.0037	0.0143	0.0079	0.0079	0.0833
Geotextile											
Mean	NA	NA	0.332	0.785	0.003	3.582	9.261	0.785	0.006	0.083	6.538
Standard Deviation	NA	NA	0.181	0.107	0.007	2.023	4.150	0.107	0.010	0.043	4.046

ρ_s is particle density, ρ_b is dry bulk density, K_s is saturated hydraulic conductivity, θ_s is the saturated volumetric water content, θ_r is the residual volumetric water content, λ and h_b are Brooks-Corey model fitting parameters, and α and n are van Genuchten model fitting parameters.

Table 3.24. Best-Fit Parameter Values and Statistics for Soil Materials

Sample	ρ_s (g cm^{-3})	ρ_d (g cm^{-3})	K_{su} (cm/s)	Brooks-Corey θ_s (cm^3 cm^{-3})	Brooks-Corey θ_r (cm^3 cm^{-3})	Brooks-Corey λ (-)	Brooks-Corey h_b (cm)	van Genuchten θ_s (cm^3 cm^{-3})	van Genuchten θ_r (cm^3 cm^{-3})	van Genuchten α (cm^{-1})	van Genuchten n (-)
ERDF Structural Fill at 90% of Max. Density											
B1B394	2.68	1.55	2.31E-02	0.3633	0.0090	0.8057	25.4647	0.3716	0.0090	0.0234	2.2355
B1BRD4	2.68	1.57	2.15E-02	0.3373	0.0110	1.3735	44.9236	0.3494	0.0110	0.0161	2.9905
Mean	2.68	1.56	2.23E-02	0.3503	0.0100	1.0896	35.1942	0.3605	0.0100	0.0198	2.6130
Stdev.	0.00	0.01	1.13E-03	0.0184	0.0014	0.4015	13.7595	0.0157	0.0014	0.0052	0.5339
ERDF Structural Fill at 95% of Max. Density											
B1B394	2.68	1.64	1.98E-02	0.3814	0.0100	0.8948	31.9081	0.3945	0.0100	0.0191	2.4366
B1BRD4	2.68	1.66	1.35E-02	0.3600	0.0110	0.9020	27.6243	0.3716	0.0110	0.0243	2.2440
Mean	2.68	1.65	1.63E-02	0.3707	0.0105	0.8984	29.7662	0.3831	0.0105	0.0217	2.3403
Stdev	0.00	0.01	4.45E-03	0.0151	0.0007	0.0051	3.0291	0.0162	0.0007	0.0037	0.1362
Quarry Spalls with Silt Loam Matrix											
B18DD3/B18DD2	2.75	2.43	8.58E-06	0.1190	0.0074	0.3714	56.9152	0.1282	0.0025	0.0197	1.3324
B18DD4/B18DF7	2.76	2.43	1.04E-05	0.1383	0.0056	0.2934	24.6792	0.1279	0.0158	0.0161	1.4255
B18DD5	2.74	2.43	3.93E-07	0.1350	0.0074	0.4738	187.9699	0.1257	0.0195	0.0039	1.5280
B18DF5	2.79	2.42	3.28E-06	0.1282	0.0067	0.6234	246.3054	0.1393	0.0067	0.0049	1.4762
Mean	2.76	2.43	3.28E-06	0.1301	0.0068	0.4405	128.9674	0.1302	0.0111	0.0112	1.4405
Standard Deviation	0.02	0.00	4.65E-06	0.0085	0.0008	0.1426	105.3835	0.0061	0.0079	0.0079	0.0833

ρ_s is particle density, ρ_b is dry bulk density, K_s is saturated hydraulic conductivity, θ_s is the saturated volumetric water content, θ_r is the residual volumetric water content, λ and h_b are Brooks-Corey model fitting parameters, and α and n are van Genuchten model fitting parameters.

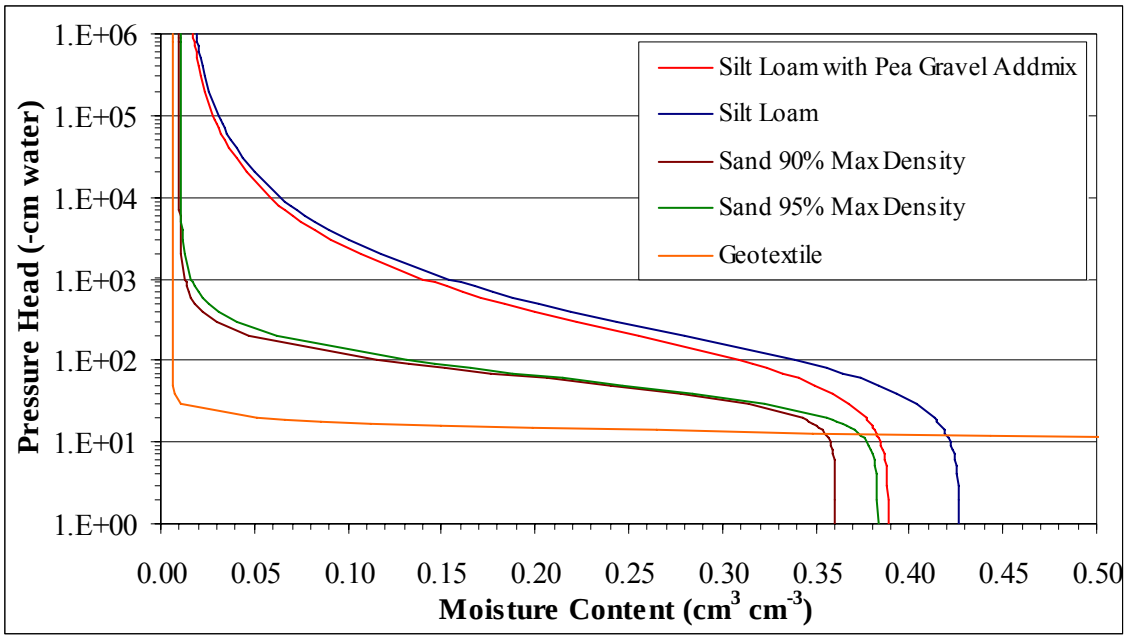

Figure 3.20. van Genuchten Model Predicted Water Characteristics Curve for the Silt Loam with Pea Gravel Admixture Soil, Silt Loam Soil, ERDF Structural Base Fill Soil at 90% and 95% Maximum Dry Density, and the geotextile. The predicted water characteristic curves represent the mean van Genuchten parameters for each soil.

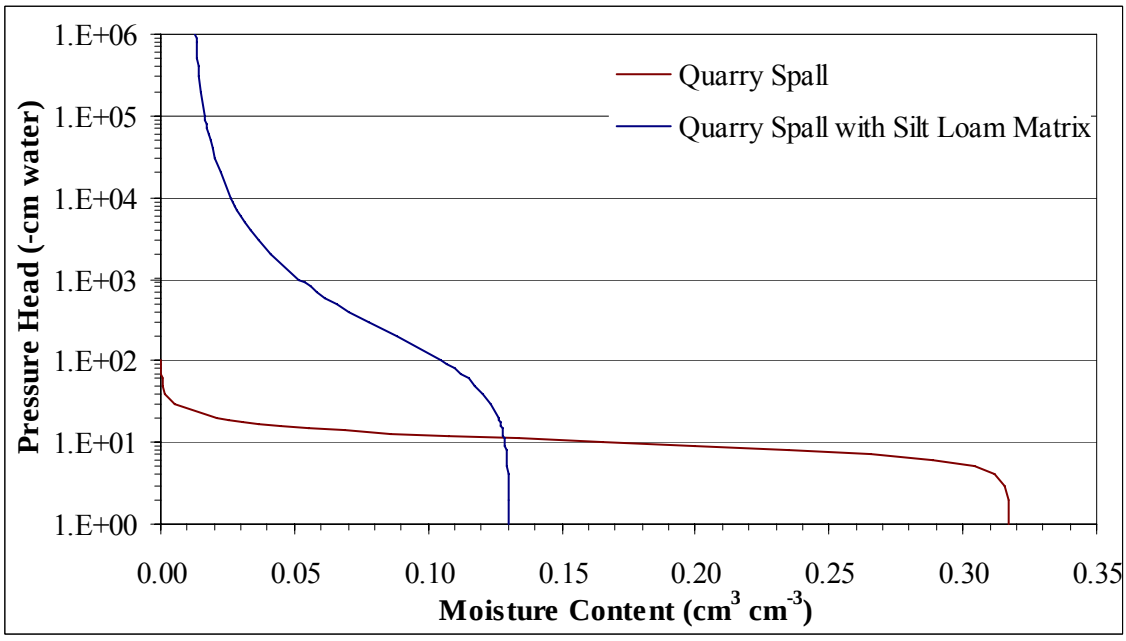

Figure 3.21. van Genuchten Model Predicted Water Characteristics Curve for the Quarry Spalls and the Quarry Spalls with Silt Loam Matrix

4.0 Best-Estimate Values for Thermal Parameters

This section summarizes the best-estimate values for the thermal parameters of soil and geotechnical materials to be used in the performance-assessment analyses of the candidate barriers. The thermal parameters reported here are derived mostly from published measurements of specific heat and from pedotransfer functions for thermal conductivity based on water retention and grain-size distributions.

4.1 Specific Heat

The specific heat of the different materials was estimated by summing the contributions of each mineral weighted by its volume fraction, as described in Section 2.8.2. Values of specific heat and densities for the major constituents of soil and geotechnical materials are listed in Table 4.1. Due to the small heat capacity of air, its contribution to the total heat capacity may be neglected without any significant reduction in accuracy.

Table 4.1. Specific Heat and Density of Soil Minerals and Polymers

Group	Rock Type	Specific Heat (J/ kg C)	Density (kg/m^3)
Silica Minerals	Quartz	698	2647
	Silica	700	2205
Carbonates	Calcite	793	2710
Alkali Feldspar	Microline	680	2558
	Orthoclase	610	2583
Plagioclase	Albite	709	2610
	Anorthite	700	2740
Micas	Muscovite	880	2851
	Biotite	880	2980
	Chlorite	880	2641
	Serpentine	880	2619
Amphiboles	Tremolite	n/a	2981
	Anthophylite	740	3028
	Hornblende	n/a	3111
Oxides	Hematite	610	5143
	Ilmenite	n/a	4547
	Spinel	n/a	3633
Selected Rocks	Basalt	840–858	2580–2920
	Claystone	820–930	2360–2830
	Sandstone	750–1380	2350–2970
Organic matter		1923	1300
Polymers	Polypropylene	1925	850
	Polyethylene	1850	941
	Polystyrene	1170	1050

Knowledge of the composition of the sediments and geotechnical materials is needed to estimate specific heat from these values. The composition of soil is determined form the mineralogy, which can be inferred from X-ray diffraction analyses. No mineralogical studies were performed on the borrow-source or ERDF spoil pile samples, but such analyses have been conducted for a variety of Hanford sediments with similar parent materials and depositional environments. Some of these data were recently summarized by Murray et al. (2003). Table 4.2 provides a summary of the mineral composition of typical Hanford coarse-grained sediments while Table 4.3 summarizes the mineral composition of typical fine-grained sediments.

Table 4.2. Mineral Composition of Typical Hanford Coarse-Textured Sediments

	Mineral Phase (wt-%)					
Sample ID	**Quartz**	**Amphibole**	**Plagioclase**	**K-Spar**	**Mica**	**Chlorite**
A-1	36.0	3.0	30.0	16.0	12.0	3.0
A-2	30.0	5.0	35.0	17.0	10.0	3.0
A-5	30.0	3.0	35.0	15.0	14.0	3.0
B-1	37.0	4.0	33.0	13.0	11.0	3.0
B-2	37.0	2.0	34.0	13.0	11.0	3.0
Mean	34.0	3.4	33.4	14.8	11.6	3.0

Table 4.3. Mineral Composition of Typical Hanford Fine-Textured Sediments (after Murray et al. 2003)

	Mineral Phase (wt-%)					
Sample ID	**Quartz**	**Amphibole**	**Plagioclase**	**K-Spar**	**Mica**	**Chlorite**
A-3	40.0	5.0	22.0	13.0	17.0	4.0
A-4	31.0	3.0	26.0	12.0	19.0	8.0
A-6	35.0	5.0	30.0	14.0	11.0	4.0
Mean	35.3	4.3	26.0	13.0	15.7	5.3

Quartz content is an important input parameter for estimating thermal properties using the proposed methods. However, quartz content as a function of soil type is generally not tabulated. It is known that sand usually contains a very high percentage of quartz in crystalline form (Buckman and Brady 1969). Silt may also contain silicates, but these are not generally in the form of crystals. It is only quartz crystals that have a very high thermal conductivity, whereas the conductivity of quartz or silicate material bound inside clay or silt particles is similar to that of other soil materials (Farouki 1981). In the absence of mineralogical data, the mean value reported above can be used. These values are somewhat low compared to those reported for Peters-Lidard et al. (1988) in a study of quartz composition as a function of texture. In that study, it was assumed that the quartz content was equal to the sand content and ranged from 92% for a sand to 40% for a loam and 10% for a silt. Clay also plays an important role in the thermal properties. Table 4.4 and Table 4.5 summarize the clay composition for coarse and fine-textured Hanford sediments, respectively.

Table 4.4. Clay Minerals in Typical Coarse-Textured Hanford Sediments

Sample	Mineral Phase (wt-%)			
ID	Smectite	Illite	Chlorite	Kaolinite
A-1	53.0	29.0	10.0	8.0
A-2	35.0	40.0	16.0	8.0
A-5	38.0	37.0	15.0	9.0
B-1	33.0	44.0	14.0	8.0
B-2	45.0	33.0	14.0	8.0
Mean	40.8	36.6	13.8	8.2

Table 4.5. Clay Minerals in Typical Fine-Textured Hanford Sediments

Sample	Mineral Phase (wt-%)			
ID	Smectite	Illite	Chlorite	Kaolinite
A-3	49.0	34.0	8.0	9.0
A-4	44.0	37.0	11.0	8.0
A-6	39.0	37.0	13.0	11.0
Mean	44.0	36.0	10.7	9.3

Published values for fine and coarse quartz sand are 824.8 and 795.49 J kg^{-1} $^oC^{-1}$, respectively (Jury et al. 1991). A clay soil of unknown mineralogy was reported to have a value of 1130.43 J kg^{-1} $^oC^{-1}$, whereas the heat capacity of silt loam ranged from 689.63 to 812.24 J kg^{-1} $^oC^{-1}$. For more site-specific data, Shannon and Wilson (1994) reported measurements of specific heat for sediments collected from the southeastern side of Hanford's 200 West Area. Specific heat was measured at temperatures of 14^{o}C, 48.7^{o}C, and 86.25^{o}C and at bulk densities of 1.682 g cm^{-3}, 1.762 g cm^{-3}, and 1.81 g cm^{-3}. These measurements were repeated at different moisture contents, ranging from 0% to 12.6% results. The results of these measurements are summarized in Table 4.6.

Table 4.6. Measured Specific Heats of Hanford Sediments

	Specific Heat (J/ kg C)		
Moisture Content (m^3 m^{-3})	14.3^{o}C	48.75^{o}C	86.25^{o}C
0.00	430.31	488.46	558.24
0.02	471.02	529.17	598.95
0.13	674.54	721.06	790.84

Our interest is the specific grain specific heat as this is the input parameter for STOMP. Owing to the absence of data, the grain specific heat is inferred from the dry specific heat. Results showed no density effects on specific heat for dry soils, an expected result given that specific heat is expressed on a unit weight basis. The dry specific heat values, however, appear quite low compared to literature values of between 795.49 and 824.8 J kg^{-1} $^oC^{-1}$ for quartz sands. These low values could be due to the relatively low quartz content of the sediments (35%) compared to that of a "typical" sand (92%). In fact, the quartz

content of these sediments is more consistent with the 40% expected for a loam soil (Peters-Lidard et al. 1988).

The best-estimate values for the grain specific heat of the materials to be used in construction are given in Table 4.7. These values were calculated from the mean mineral composition and specific heats using Eq. 2.18 after converting the mass fraction to a volume fraction using the material density. These values are more consistent with those reported in the soils literature (Jury et al. 1991).

Table 4.7. Best-Estimated Values of Grain Specific Heat of Barrier Materials

Material	Specific Heat (J/ kg C)
Hanford Clay	890.00
Sand	730.59
Silt/Silt Loam	793.09
Quarry Spalls- Soil Admixture	852.16
Crushed Basalt/gavel	712.25
Geotextile	1925.00

4.2 Thermal Conductivity

For all of the materials, thermal conductivity as a function of saturation was predicted from the water-retention curve using the methods of Johansen (1975) as implemented in SoilVision (2001). The parameters needed for STOMP input were obtained by fitting the resulting functions to the Cass model (Cass et al. 1984).

4.2.1 Silt Loam

Figure 4.1 shows a plot of thermal-conductivity data predicted by the pedotransfer functions and the fit to the Cass model for the composites B18DD3/B18DD2 and B18DD4/B18DF2 as well as samples B18DD5 and B18DF5. Table 4.8 gives the predicted grain specific heat and thermal-conductivity parameters for the Cass model.

Table 4.8. Best-Estimate Thermal Parameter Values for Silt loam

Sample ID	Grain Specific Heat (J/kg C)	A W/(m°C)	B W/(m°C)	C [-]	D W/(m°C)	E [-]
B18DD3/B18DD2	793.1	1.208	1.014	3.533	0.184	2.477
B18DD4/B18DF7	793.1	1.179	0.983	3.453	0.190	2.240
B18DD5	793.1	1.084	0.884	3.396	0.189	2.077
B18DF5	793.1	1.047	0.889	3.524	0.187	2.505
Mean	793.1	1.130	0.943	3.477	0.188	2.325
Standard Deviation	0.0	0.076	0.066	0.065	0.003	0.203

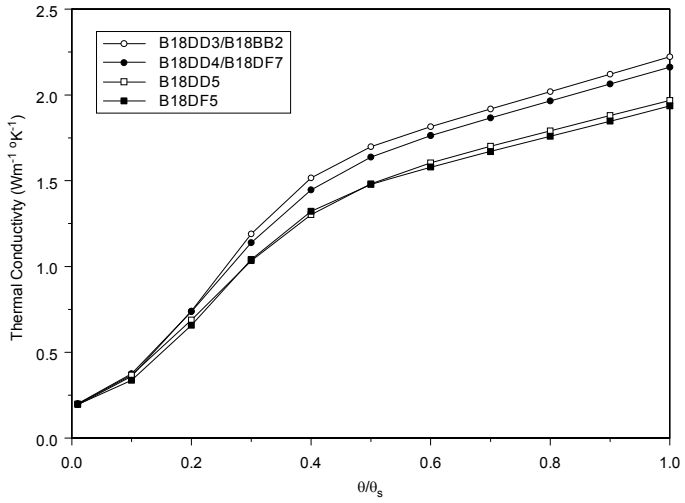

Figure 4.1. Predicted Relationship Between Thermal Conductivity and Water Content at Atmospheric Pressure and 25°C for a Silt-Loam Soil from the Silt-Loam Borrow Site

4.2.2 Silt Loam with Pea Gravel Admixture

Figure 4.2 shows a plot of thermal conductivity data predicted by the pedotransfer functions and the fit to the Cass model for the 15 percent pea-gravel admixtures containing composites B18DD3/B18DD2 and B18DD4/B18DF2 as well as samples B18DD5 and B18DF5. Table 4.9 gives the predicted heat-capacity and thermal-conductivity parameters for the Cass model.

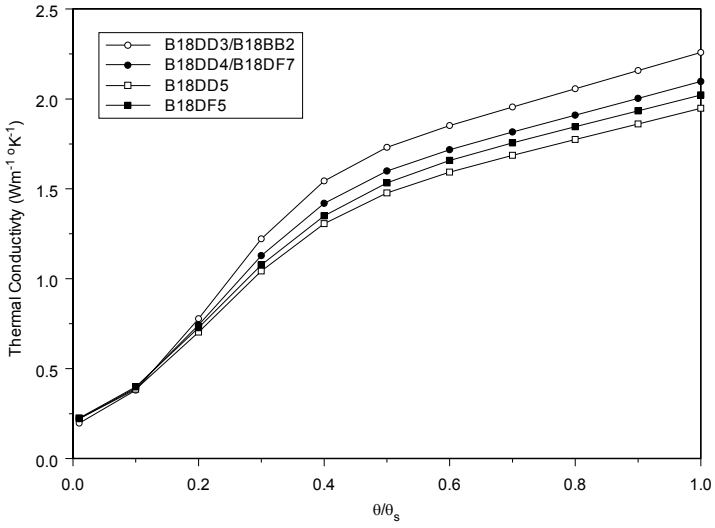

Figure 4.2. Predicted Relationship Between Thermal Conductivity and Water Content at Atmospheric Pressure and 25°C for Silt Loam-Pea Gravel Admixture

Table 4.9. Best-Estimate Thermal Parameter Values for Silt Loam-Pea Gravel Admixture

Silt Matrix Sample	Grain Specific Heat (kJ/kg C)	A W/(m °C)	B W/(m°C)	C [-]	D W/(m°C)	E [-]
B18DD3/B18DD2	712.25	1.250	1.008	3.565	0.187	2.321
B18DD4/B18DF7	712.25	1.163	0.934	3.486	0.212	2.222
B18DD5	712.25	1.081	0.867	3.440	0.213	2.120
B18DF5	712.25	1.145	0.877	3.381	0.216	2.044
Mean	712.25	1.160	0.922	3.468	0.207	2.177
Standard Deviation	0.00	0.070	0.065	0.078	0.013	0.121

4.2.3 Geotextile

Figure 4.3 shows a plot of thermal conductivity data predicted by the pedotransfer functions and the fit to the Cass model for a polypropylene geotextile material. Table 4.10 gives the heat-capacity and thermal-conductivity parameters for the Cass model.

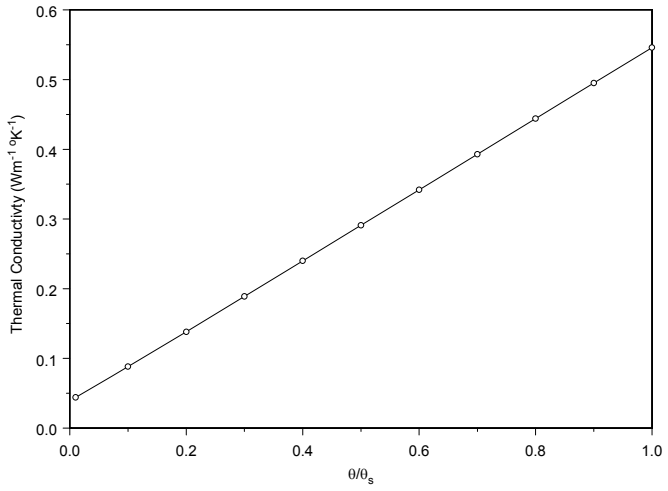

Figure 4.3. Predicted Relationship Between Thermal Conductivity and Water Content at Atmospheric Pressure and 25°C for a Polypropylene Geotextile Fabric

Table 4.10. Best-Estimate Thermal Parameter Values for a Polypropylene Geotextile

Sample ID	Grain Specific Heat (kJ/kg C)	A W/(m°C)	B W/(m°C)	C [-]	D W/(m°C)	E [-]
Geotextile	1925	0.036	0.510	9.161	0.039	2.851

4.2.4 Base Fill

Figure 4.4 shows a plot of thermal-conductivity data predicted by the pedotransfer functions and the fit to the Cass model for two composite samples from the ERDF spoil pile. The two samples, B1B394 and B1BRD4, were compacted to 90 and 95 percent of the maximum dry density. The 90-percent maximum dry densities were 1.55 g cm^{-3} and 1.57 g cm^{-3} for B1B394 and B1BRD4, respectively. The 95-percent maximum dry densities were 1.64 g cm^{-3} and 1.66 g cm^{-3} for B1B394 and B1BRD4, respectively. Because of the variability of thermal conductivity between samples, a single set of parameters for the Cass model was determined by fitting both soils simultaneously.

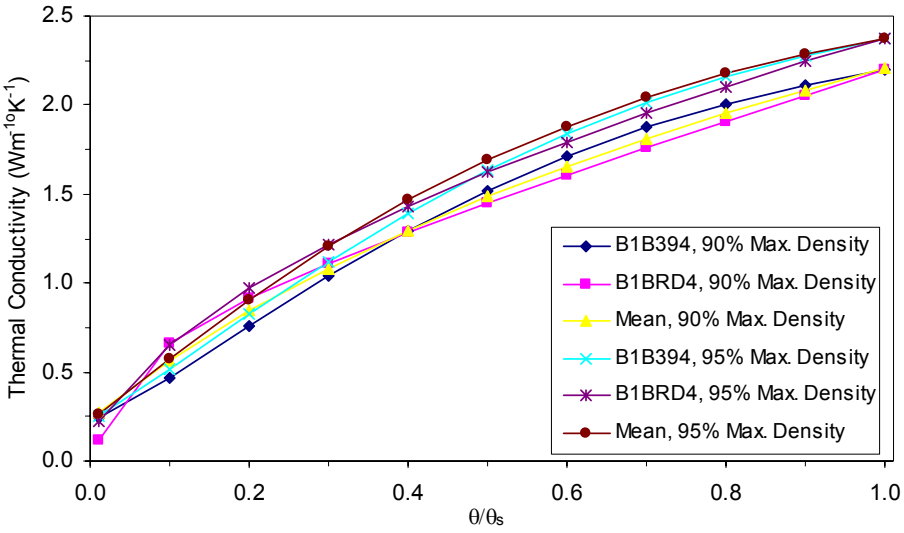

Figure 4.4. Predicted Relationship Between Thermal Conductivity and Water Content at Atmospheric Pressure and 25°C for the Compacted ERDF Spoil Pile Sand to Be Used as Structural Fill

Table 4.11 gives the heat-capacity and thermal-conductivity parameters for the Cass model at 90- and 95-percent maximum density as well as the mean parameters. Differences in the thermal conductivity-saturation relationship for the 90- and 95-percent maximum dry-density samples can be attributed to the importance of dry bulk density and porosity in the calculation of thermal conductivity for dry and saturated soils using the Johansen (1975) method. From the Johansen relationships presented in Section 2.8.1, an increase in porosity leads to a decrease in the thermal conductivity at full saturation. Likewise, as bulk density decreases (porosity increases), the thermal conductivity of the dry material will decrease. Both trends result from an increase in the pore space available for water (at saturation) and air (at dry state), each of which possesses a smaller thermal conductivity than the soil material.

4.2.5 Quarry Spalls

Figure 4.5 shows a plot of thermal conductivity data predicted by the pedotransfer functions and the fit to the Cass model for basalt riprap. The water retention was estimated using the model of Arya and Paris (1980) on an interpolated grain-size curve for quarry spalls and used to predict the thermal conductivity function. Table 4.12 gives the heat capacity and thermal conductivity parameters for the Cass model.

Table 4.11. Best-Fit Parameter Values and Statistics for ERDF Structural Fill Samples at 90 and 95 Percent of Maximum Dry Density

Sample ID	Specific Heat (kJ/kg C)	A W/(m°C)	B W/(m°C)	C [-]	D W/(m°C)	E [-]
B1B394, 90% Max. Dry Density	730.6	4.936	-1.219	1.246	0.247	1.117
B1BRD4,90% Max. Dry Density	730.6	1.816	1.432	5.198	-0.937	0.163
Mean 90% Max. Dry Density	730.6	3.15	0.168	0.963	0.228	0.915
Stdev. 90% Max. Dry Density	NA	NA	NA	NA	NA	NA
B1B394, 95% Max. Dry Density	730.6	4.288	-1.011	1.318	0.268	1.132
B1BRD4, 95% Max. Dry Density	730.6	4.354	-0.444	0.959	0.329	0.961
Mean 95% Max. Dry Density	730.6	4.33	-0.797	1.244	0.235	1.067
Stdev 95% Max. Dry Density	NA	NA	NA	NA	NA	NA

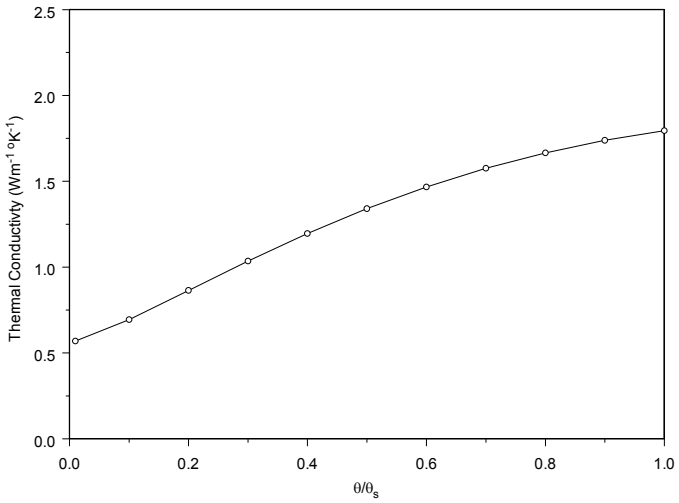

Figure 4.5. Predicted Relationship Between Thermal Conductivity and Water Content at Atmospheric Pressure and 25°C for Basalt Riprap

Table 4.12. Best-Estimate Parameter Values for Quarry Spalls

Sample ID	Grain Specific Heat (kJ/kg C)	A W/(m°C)	B W/(m°C)	C [-]	D W/(m°C)	E [-]
NA	880.0	3.042	-0.58	1.249	0.564	1.221

4.2.6 Quarry Spalls with Silt Loam Matrix

Figure 4.6 shows a plot of thermal-conductivity data predicted by the pedotransfer functions and the fit to the Cass model for basalt riprap in a silt-loam matrix. The silt-loam grain-size distribution was modified to incorporate that for quarry spalls with the assumption that silt loam would occupy the entire pore space of the riprap.
Table 4.13 gives the heat capacity and thermal conductivity parameters for the Cass model.

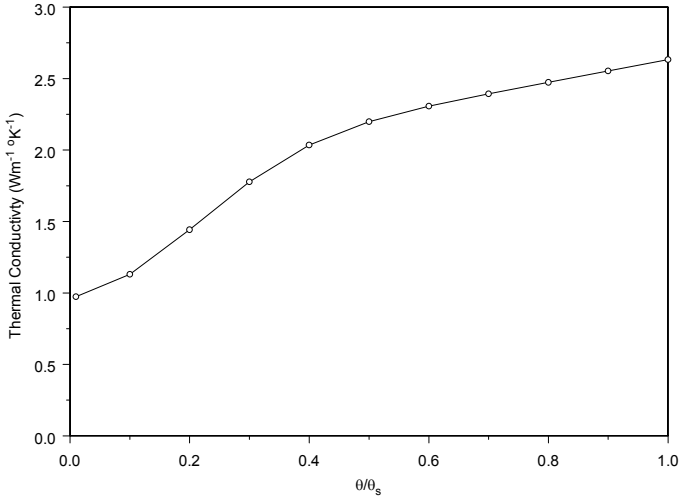

Figure 4.6. Predicted Relationship Between Thermal Conductivity and Water Content at Atmospheric Pressure and 25°C for Basalt Riprap in a Silt-Loam Matrix

Table 4.13. Best-Estimate Parameter Values for Quarry Spalls with Silt Loam Matrix

Sample ID	Grain Specific Heat (kJ/kg C)	A W/(m°C)	B W/(m°C)	C W/(m°C)	D W/(m°C)	E W/(m°C)
NA	861.0	1.838	0.794	3.449	0.964	2.125

4.2.7 ASTM C-33 Aggregates

Sample B1F3D4 was custom blended to meet the specifications of the ASTM C-33 fine aggregate and grain-size distribution, and the water retention was determined. Figure 4.7 shows a plot of thermal-conductivity data predicted by the pedotransfer functions and the fit to the Cass model for the custom blends of B1F3D4. Table 4.14 gives the heat-capacity and thermal-conductivity parameters for the Cass model.

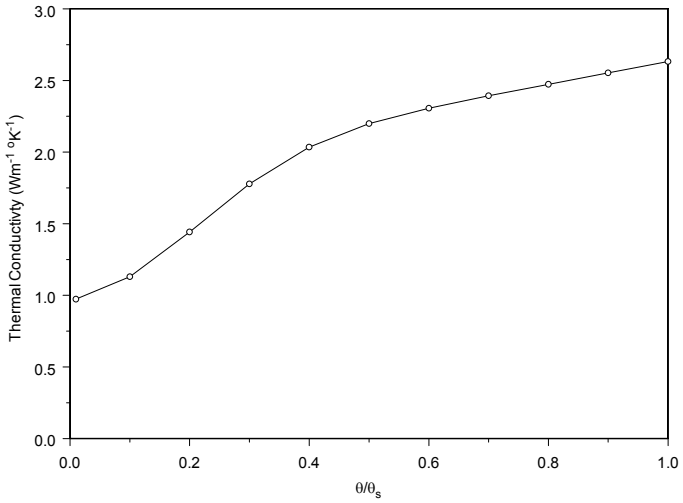

Figure 4.7. Predicted Relationship Between Thermal Conductivity and Water Content at Atmospheric Pressure and 25°C for B1F3D4 Custom Blended to ASTM C-33 Specifications

Table 4.14. Best-Estimate Parameter Values for B1F3D4 Custom Blend at 80%, 90%, and 95% Mean Settled Density

Sample ID	Grain Specific Heat (kJ/kg C)	A W/(m°C)	B W/(m°C)	C [-]	D W/(m°C)	E [-]
B1F3D4 (80% MSD)	730.6	1.816	1.432	5.198	-0.937	0.163
B1F3D4 (90% MSD)	730.6	3.15	0.168	0.963	0.228	0.915
B1F3D4 (95% MSD)	730.6	4.354	-0.444	0.959	0.329	0.961

4.2.8 Biointrusion Layer

Table 4.15 gives the heat-capacity and thermal-conductivity parameters for the Cass model.
Figure 4.8 shows a plot of thermal-conductivity data predicted by the pedotransfer functions and the fit to the Cass model for the biointrusion layer.

Table 4.15. Cass Model Parameters for Crushed Ballast and Crushed Gravel

Sample ID	ρ_b (g/cm^3)	Grain Specific Heat (kJ/kg C)	A W/(m°C)	B W/(m°C)	C [-]	D W/(m°C)	E [-]
Crushed Ballast	1.95	880.0	0.427	0.188	5.315	2.226	-0.638
Crushed Ballast	1.85	880.0	0.371	0.175	5.238	2.119	-0.633
Crushed Gravel	1.95	880.0	0.435	0.216	5.164	2.691	-0.628
Crushed Gravel	1.85	880.0	0.376	0.183	4.931	2.593	-0.611

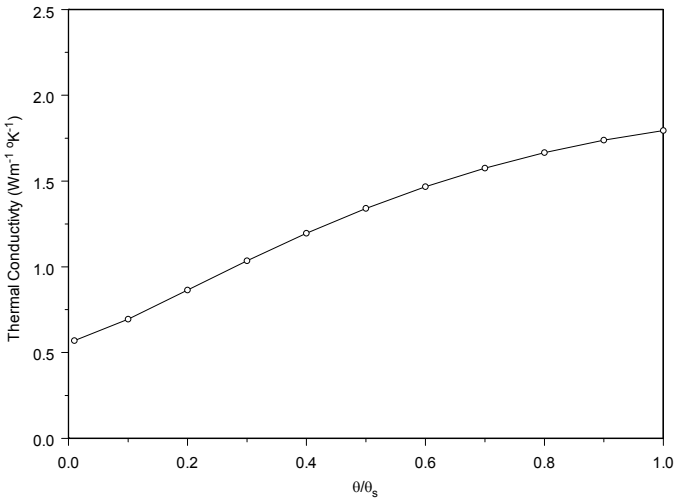

Figure 4.8. Predicted Relationship Between Thermal Conductivity and Water Content at Atmospheric Pressure and 25°C for the Biointrusion Layer

4.3 Bare-Soil Albedo

Recent studies focused on an improved understanding of the effects of tillage systems of the energy balance have yielded a large body of data for albedo under varying moisture conditions (e.g. Dickinson et al. 1993; Post et al. 2000; Lobell and Asner 2002; Oguntunde et al. 2006). These data suggest that soil albedo is a nonlinear function of soil-water content of the uppermost layer of soil. Idso et al. (1975) reported that for soil depths on the order of 2 cm, the albedo water-content relationship was independent of season. For greater depth intervals, a given albedo may correspond to slightly greater average soil water content during periods of high evaporative demand. Table 4.16 represents Eppley pyranometer 0.3- to 2.8-μm albedo measurements for a range of soil textures (Post et al. 2000). These soils include those expected to be used on the surface of engineered covers. In general, albedo increased as mean gain size increased. The Clover Springs silt loam had the lowest values (dry= 0.048, wet = 0.115) whereas sand had the highest values (dry = 0.402, wet = 0.275). The mean and standard deviation for each texture are also reported.

Table 4.16. The 0.3 to 2.8 Δm Soil Albedo, with Means and Standard Deviation (in parentheses) and Estimated Albedo Attenuation Coefficient, κ

Texture	Soil Series	Albedo		
		Dry Soil	Wet Soil	κ
Clay loam	Epitaph	0.149	0.077	
Clay loam	Gaston	0.199	0.107	
Clay loam	Gothard	0.326	0.165	
Clay loam	Pima	0.220	0.115	
	$\overline{\alpha}$	0.224 (0.075)	0.116 (0.037)	0.136
Loam	Avondale	0.255	0.162	
Loam	Gila	0.279	0.150	
Loam	Graham	0.168	0.086	
Loam	Miamian	0.223	0.098	
Loam	Steward	0.325	0.165	
	$\overline{\alpha}$	0.250 (0.059)	0.132 (0.037)	
Loamy sand	Amarillo	0.250	0.167	
Loamy sand	Brazito	0.267	0.161	
Loamy sand	Hersh	0.285	0.153	
	$\overline{\alpha}$	0.267(0.014)	0.160 (0.006)	
Sand	Superstition	0.402	0.275	0.0201
	$\overline{\alpha}$	0.402 (0.000)	0.275 (0.000)	
Sandy clay	White House	0.183	0.118	
	$\overline{\alpha}$	0.183 (0.000)	0.118 (0.000)	
Sandy clay loam	Casa Grande	0.248	0.152	
Sandy clay loam	Mohave	0.237	0.155	
	$\overline{\alpha}$	0.243 (0.008)	0.154 (0.002)	
Sandy Loam	Bernardino	0.175	0.109	
Sandy loam	Canelo	0.362	0.186	
Sandy loam	Cave	0.271	0.146	
Sandy loam	Hathaway	0.214	0.121	
Sandy loam	McAllister	0.212	0.136	
Sandy loam	Stronghold	0.238	0.138	
	$\overline{\alpha}$	0.245 (0.065)	0.139 (0.026)	
Silt loam	Clover springs	0.115	0.048	
Silt loam	Loring	0.295	0.154	
Silt loam	Mexico	0.206	0.088	
	$\overline{\alpha}$	0.205 (0.090)	0.097(0.054)	0.076
	Population Mean	**0.244 (0.066)**	**0.137 (0.044)**	

4.4 Summary

Best-estimate values for the thermal properties of soil and geotechnical materials to be used in the performance-assessment analyses of the candidate barriers were presented above. Thermal properties were not measured for the samples of interest but instead, were estimated from available data, particularly the grain-size distributions, water retention, and mineralogy.

Literature values of specific heat for Hanford sediments were limited to those reported by Shannon and Wilson (1994) for the 200 West Area. Values of specific heat reported for a dry sand at 14°C, 48.75°C and 86.25°C were interpolated to estimate the value of 448.23 J kg^{-1} $°C^{-1}$ at 25°C. These values appear quite low compared to values published in the soils literature. For example, Jury et al. (1991) reported values of 824.8 J kg^{-1} $°C^{-1}$ for a fine quartz sand, 795.49 J kg^{-1} $°C^{-1}$ for a coarse quartz sand, and a range for 689.63 to 812.24 J kg^{-1} $°C^{-1}$ for a silt-loam soil. In more recent work, Ochsner et al. (2001) reported a value of 801 J kg^{-1} $°C^{-1}$ for a sandy loam, 846 J kg^{-1} $°C^{-1}$ for a clay loam, 871 J kg^{-1} $°C^{-1}$ for a silt loam, and 895 J kg^{-1} $°C^{-1}$ for a silty-clay loam. Values estimated for barrier sediments based on mineralogy are more consistent with values from the soils literature than those reported by Shannon and Wilson (1994). Values of specific heat calculated from mineralogical composition ranged from 730.6 J kg^{-1} $°C^{-1}$ for sand to 852.2 J kg^{-1} $°C^{-1}$ for a quarry spalls admixture with the geotextile fabric having the highest value of 1925 J kg^{-1} $°C^{-1}$ (Table 4.7).

A small amount of experimental measurements of thermal conductivity as a function of saturation have been reported in the literature for Hanford sediments. Measurements made on the lysimeter sand from the BWTF were reported by Cass et al. (1981) whereas measurements on sediments from the 200 West Area were reported by (Shannon and Wilson 1994). Measurements were also reported by Cass et al. (1981) for a Portneuf silt loam, a soil from southern Idaho, which could be used as an analogue for the finer textured soils although the composition is somewhat different with 19% clay, 61% silt, and 20% sand. A larger body of work was found in the wider soils literature, including a comprehensive study by Ochsner et al. (2001) that covered 60 soils.

In general, thermal conductivity, λ, of a given material increased with increasing water content from the dry state to saturation, and this was observed in literature values as well as in the pedotransfer function predictions. Published values for dry sand from the soils literature ranged from 0.15 to 0.25 W m^{-1} K^{-1} whereas predicted values for ERDF spoil samples ranged from 0.26 to 0.37 W m^{-1} K^{-1}. Measured values reported by Shannon and Wilson (1994) for sand from Hanford's 200 West Area ranged from 0.45 W m^{-1} K^{-1} to 0.47 W m^{-1} K^{-1}. Thus, the predicted values are around the upper end of the range of published values from the soils literature but somewhat lower than the measured values for Hanford sand. Published values for saturated sand ranged from 2 to 4 W m^{-1} K^{-1}. The range of thermal conductivity from data published for a range of soils in the literature was between 0.15 and 4.0 W $m^{-1}K^{-1}$. However, values of $\lambda(\theta)$ predicted for barrier soil materials similar to those for which data have been published were consistently higher than the measured values.

The albedo of near-surface sediments plays an important role in surface energy balance and meteorological processes. On bare-soil surfaces, the partitioning of incoming solar radiation into absorbed and reflected is due solely to soil albedo. Input parameters needed to describe the dependence of albedo on soil moisture content, and ultimately the albedo of bare and vegetated surfaces, was also summarized. In general, albedo increases as mean gain size increases. Silt-loam soils, which are

expected to form the surface layer of engineered barriers, had the lowest albedo values (dry= 0.048, wet = 0.115) whereas sand had the highest values (dry = 0.402, wet = 0.275). Soil albedo appears to be a nonlinear function of soil water content of the uppermost layer of soil.

5.0 Best-Estimate Values for Plant Parameters

It is expected that future barriers will be vegetated with native plant species and in a manner similar to the prototype Hanford barrier at the 200-BP-1 operable unit. Accounting for the effect of plants on barrier performance requires a variety of input parameters, particularly those identified in Section 2. This section describes the plant data collected and summarizes best-estimate values for plant parameters to be used as input for the STOMP model. The data described in this section are mostly from literature reviews with a small amount coming from the Hanford site, particularly the prototype Hanford barrier.

5.1 Canopy Interception

Interception rates in shrub-steppe ecosystems are often assumed to be minor because the vegetation canopies are typically small, and total ground cover is often less than 50%. However, on a percentage basis, rangelands and shrub-steppe ecosystems of semi-arid regions lose considerably more water via canopy interception than more humid environments (West and Gifford 1976). Owing to the potential for canopy interception to reduce the amount of water available for infiltration, this mechanism is included into the conceptual model.

Published data on dependence of the fraction of rainfall intercepted on precipitation depth at different intensities were used to calibrate Eq. (2.29) and thereby estimate c_m and the empirical constant, c. Figure 5.1 shows there is indeed a strong relationship between interception of rainfall and rainfall intensity as reported by Massman (1980).

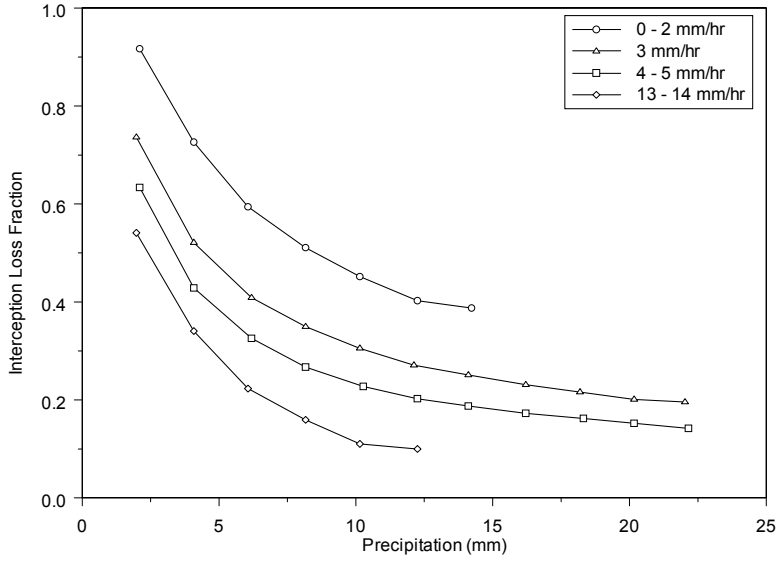

Figure 5.1. The Dependence of the Fraction of Rainfall Intercepted on Precipitation Depth at Different Intensities (after Wells and Blake 1972)

In general, interception is highest under low rainfall intensities and under misty, drizzle-like conditions. Conversely, interception is typically small under intense precipitation conditions (Wells and Blake 1972). This behavior can also be expected for desert plants. However, the only published studies of interception rates of semi-arid shrub steppe ecosystems are those of Hull (1972) and Hull and Klomp (1974). The two input parameters required for STOMP are the maximum condensate depth, c_m, and the empirical constant, c.

Because maximum condensate depth, c_m, depends only on the vegetative characteristics of the canopy, all of the interception data were fitted simultaneously with a single value of c_m but different values of the empirical constant, c (Eq. 2.19), to characterize the relation between interception capacity and rainfall intensity. A single value of maximum dew depth, c_m = 1.984 mm, described the data quite well, confirming that plant-canopy characteristics control the magnitude of interception loss with the maximum being determined by the interception capacity. The default value for c_m in STOMP is therefore 1.984 mm.

Although there are no data for rainfall interception in plant canopies at Hanford, a coefficient for rainfall interception capacity that depends on intensity is consistent with observations reported in the literature. West and Gifford (1976) suggested that an average of about 0.59 cm of rain is intercepted yearly by the sagebrush and shadscale plant communities in Idaho for storms over 0.15 cm. This is equivalent to 4% of the total annual precipitation that falls as rain (West and Gifford 1976). A comparison between interception in heavy brush and in brush-free areas showed that the heavy brush intercepted 31% of the rain that fell between April 1 and October 30. During the winter months, snow interception averaged 37%. The potential interception per rainfall event, derived from a sample size of 10 plants, was 0.11 cm. Interception losses from rangelands are generally between 20% and 40% but may range from 1% to 80% of the annual water budget (Wilcox et al. 2003). Average interception losses from sagebrush (*Artemisia* sp.) in these ecosystems have been reported at around 30%. Values of c fitted to the interception data in Figure 5.1 are summarized in Table 5.1.

Table 5.1. Range of Literature-Reported Values of Thermal Conductivity for Soil

Rainfall Intensity (mm/yr)	***c*** **(mm/mm)**
0–2	-0.093
3.0	0.073
4–5	0.158
10–14	0.087

5.2 Plant Height

The plant height acts to increase the momentum roughness length, z_m, and canopy zero-plane displacement, d_c, the height at which the exponential wind velocity profile approaches a zero velocity. Plant height is therefore a required input parameter and also a required input for STOMP. Long-term plant-height data for the Hanford site are quite limited. Essentially, two data sets were used for this study. The first is the data set from the 200-BP-1 prototype Hanford Barrier (Ward et al. 2005a,b). The second is the data set collected for the ILAW facility performance assessment (Downs and Khan 1999).

Figure 5.2 is a 10-yr summary of height for irrigated and nonirrigated sagebrush data from the prototype barrier. Figure 5.3 shows a 10-yr summary of rabbitbrush height on the irrigated and nonirrigated treatments. Shrub height at the time of planting was about 20 cm (Ward et al. 1997).

Equation 2.30 was fitted to the plant height versus time in Figures 5.2 and 5.3 to obtain parameters to represent the growth curve and to identify the maximum height. It is not anticipated that treatability tests at the proposed barrier will be irrigated, so only the nonirrigated data were fitted to the model. The sagebrush data fit the model reasonably well but not the rabbitbrush data. Table 5.2 shows the fitted parameters for the logistic growth function.

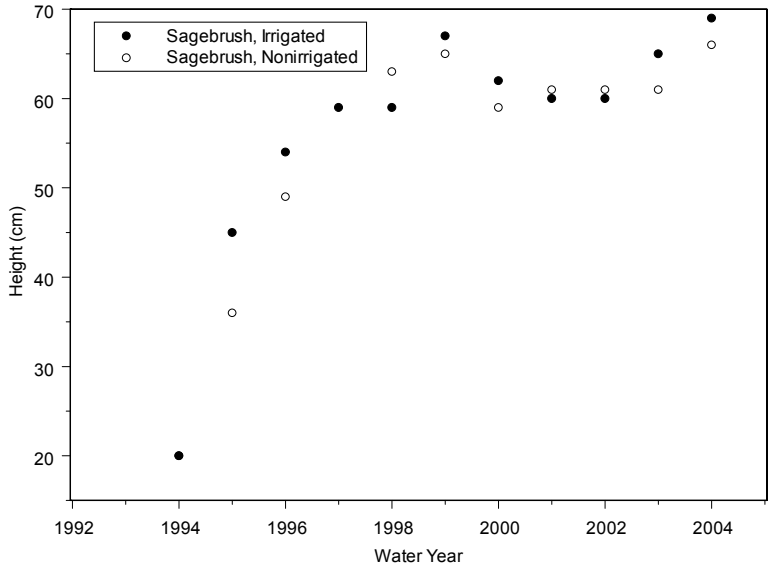

Figure 5.2. Mean Shrub Height for Sagebrush at the Prototype Hanford Barrier

The best-fit maximum height was 63.768 cm for nonirrigated sagebrush and 41.150 cm for rabbitbrush after 10 years of growth. Fitted growth rates for the irrigated and nonirrigated rabbitbrush were significantly different. These parameters can be used to generate time-dependent growth rates for model input.

Values of h_m for long-term simulations are based on studies of Wyoming and mountain big sagebrush communities in northeast and central Wyoming. Published data show mean stand ages of 32 ± 9 yr for Wyoming big sagebrush and 26 ± 9 yr for Mountain big sagebrush compared to 17 ± 3 yrs for basin big sagebrush (Perryman and Olson 2000). These data suggest that Basin big sagebrush typically grows 1 to 2 m (3 to 10 ft) in height but can occasionally have a treelike appearance, reaching a height of 5 m (16 ft). Height measurements in a mature sagebrush ecosystem at the ILAW disposal site show heights ranging from 7 to 225 cm and a mean height of 101 cm (Downs and Khan 1999). Similar measurements at the grout site show heights ranging from 10 to 175 cm and a mean height of 89 cm (Downs and Khan 1999).

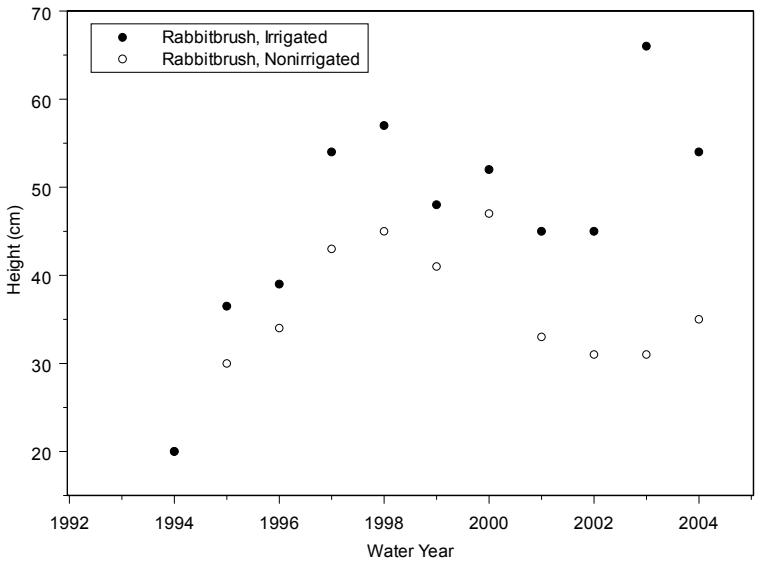

Figure 5.3. Mean Shrub Height for Rabbitbrush at the Prototype Hanford Barrier

Table 5.2. Best-Fit Parameters for the Logistic Growth Curve (Eq. 2.30) for Non-irrigated Shrubs at the Prototype Hanford Barrier

Species	Model Parameters		
	h_m (cm)	A	k
Sagebrush	63.768	2.393	1.174
Rabbitbrush	41.159	1.174	1.124

Rabbitbrush is also an erect shrub that can reach heights of 31 to 229 cm (12 to 90 inches). Certain populations have been reported to reach heights of 3.3 to 3.6 m (10 to 12 ft). Therefore, with these growth parameters, user-supplied mean stand ages, and the maximum heights, reasonable estimates of shrub heights can be obtained for simulation times beyond observations made onsite.

There are no height measurements for grasses at the prototype Hanford Barrier, but measurements were reported for the ILAW site by Downs and Khan (1999). Both cheatgrass and Sandberg bluegrass showed greater growth and canopy cover under shrubs than plants in inter-shrub spaces. Table 5.3 shows the mean heights during the winter of 1998–1999. Cheatgrass is known to have panicle inflorescence of 5 to 20 cm (2 to 8 inches) long, and leaves are typically 4 to 16 cm (2 to 6 inches) long. Although these data are insufficient to obtain model parameters, they can provide some guidance for specifying grass heights. The default h_m for grasses is 50 cm.

Table 5.3. Grass Height Measured at the Proposed ILAW Site During Winter 1998–1999

Species	Plant Height (cm)					
	October	**November**	**December**	**January**	**February**	**March**
Cheatgrass	2	3	4.5	5	6	7.5
Sandberg Bluegrass	2	3.5	6	8	8.5	10

5.3 Leaf-Area Index

The leaf-area index, L_{ai}^{i}, is a key parameter for simulating the exchange of water vapor with the atmosphere. Leaf-area data collected at the prototype Hanford barrier were fitted to the polynomial function in Eq. 2.31 to develop a predictive model for leaf-area index. The only data available were measurements made on sagebrush. The resulting coefficients of the polynomial equation are as given in Table 5.4.

Table 5.4. Model Coefficients for the Polynomial Used to Predict Shrub Canopy Leaf Area

b_0	=	-1959	b_5	=	11.0
b_1	=	-11.96	b_6	=	-0.822
b_2	=	56.52	b_7	=	-3.287
b_3	=	225.3	b_8	=	0.0579
b_4	=	-51.65	b_9	=	-50.88

The regression resulted in a significant ($F = 35.5$; $p < 0.00001$; $r^2=0.92$) relation between observed and predicted values of leaf area. The correlation between predicted and observed data resulted in a slope of 0.92 ± 0.045 (± 1 standard error), which is not significantly different from a slope of one, and an intercept of 214 ± 163, which is not significantly different from zero. The prediction of sagebrush leaf area using Eq. 2.31 was converted to leaf area index (m^2 green leaf area/m^2 ground area) using Eq. 2.32. For this purpose, the mean predicted canopy leaf area is multiplied by the number of sagebrush plants in the non-irrigated treatment (1977 plants), divided by 10,000 to convert cm^2 to m^2 and then divided by 1296 m^2. The leaf-area index increased over time, and values ranged from 0.460 to 0.737 for the non-irrigated sagebrush. This function applies only to sagebrush on the prototype Hanford barrier.

Downs and Khan (1999) used shrub and understory leaf-area data collected from the ILAW site in 1998 and 1999 to estimate the leaf-area index near peak biomass. While these data are insufficient to develop a reliable model for seasonal changes in L_{ai}^{i}, they provide insight into L_{ai}^{i} for mature ecosystems. Table 5.5 provides measures of leaf-area index in a mature sagebrush community onsite based on the work by Downs and Khan (1999). Leaf-area indices averaged around 0.25 in mature ecosystems dominated by sagebrush, but these measurements are for plants growing on much coarser soils.

Table 5.5. Estimated Leaf Area Index for Shrubs and Understory Plants Measured in 1998 and 1999 (after Downs and Khan 1999)

Month	Location	Shrubs	Understory
February	ILAW Site	0.102	0.118
April	ILAW Site	0.204	0.904
May	ILAW Site	NA	0.395
June[(a)]	ILAW Site	0.282	NA
July[(a)]	Grout Site	0.140	NA
(a) Values estimated using morphometric and plot data.			

Few examples exist of leaf-area measurements for rabbitbrush. One of the few examples is the work of Steinwand et al. (2001) in which the transpiration coefficients of three Great Basin shrubs, including rabbitbrush, were compared. The leaf-area index was determined using the quadrant method at approximately monthly intervals during the summer months. The mean curve for each species was determined and the mean curve normalized to 1.0. Uncertainty in the mean was determined from the deviation of the scaled data points from the mean curve within several time periods and was usually 20 to 25%. Figure 5.4 shows the L_{ai} for rabbitbrush (*Chrysothamnus nauseosus*) as a function of time, in this case day of year. The distribution of L_{ai} is best described by the function

$$L_{ai} = 1.0 \exp\left[-\frac{(DOY - 184)^2}{9147} \right] \tag{5.1}$$

The points were normalized by dividing each datum by the maximum of its individual fitted curve. The relatively small dataset and the similarity among parameters suggested that it may be advantageous to determine a single L_{ai}^{i} for each species.

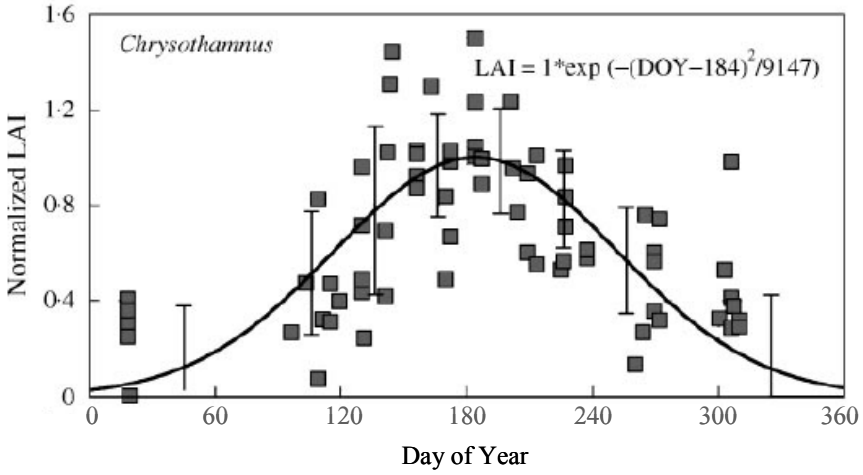

Figure 5.4. Normalized Mean Leaf Area Index Curve and Standard Deviation about the Mean for Rabbitbrush (*Chrysothamnus nauseosus*) after Steinwand et al. (2001). Each error bar is centered within the block of time it represents.

For other species of interest, L_{ai}^{i} can be estimated from published relationships between cover and L_{ai}^{i} as the two indices are strongly correlated. For example, Steinwand et al. (2001) reported a 93% coefficient of determination (r^2) for the relationship between leaf-area index and percent cover for rabbitbrush given by L_{ai}^{i} = 0.041 × % cover (Table 5.6).

Table 5.6. Empirical Relationships for Estimating Leaf-Area Index from Plant-Area Index

Plant Type	L_{ai}^{i}	Literature Source
Annual	$1.17 \times P_{ai}^{i}$	Werk et al. (1983); International Biological Program (1974)
Forbs	$2.37 \times P_{ai}^{i}$	International Biological Program (1974)
Grass	$3.60 \times P_{ai}^{i}$	Williamson et al. (1987)
Shrub	$5.70 \times P_{ai}^{i}$	Ludwig et al. (1975); Depuit and Caldwell (1975)
Creosote Bush	$0.65 \times P_{ai}^{i}$	Ludwig et al. (1975); Barbour (1977)
Rabbitbrush	$0.041 \times P_{ai}^{i}$	Steinwand et al. (2001)

5.4 Plant-Area Index

The plant-area index for plant species *i*, P_{ai}^{i}, is a measure of the species fractional cover and takes into account the spatial distribution of the vegetation and is an important input parameter. Available site data are limited to measurements from locations investigated for use with the ILAW program and the prototype Hanford barrier. The Hanford Site resides within the sagebrush-bunchgrass vegetation zone, and common native species include sagebrush and rabbitbrush, several species of forbs, and perennial grasses. Data from two mature natural sagebrush-grass ecosystems, the ILAW disposal site, and the Grout site are shown in Table 5.7. Data from the prototype Hanford barrier in the 200 Area are also shown.

Although shrub canopy cover is nearly equal at the ILAW and Grout sites, the density of shrubs at the ILAW site (4000/ha) is 1.5 times that at the Grout Site (2590/ha). For the native grasses (mostly Sandberg bluegrass) and native forbs, percent ground cover was also higher on the ILAW site than on the Grout site. This difference is reflected in the higher species diversity found on the ILAW site (Downs and Khan 1999). These densities can be considered representative of the sagebrush/bunchgrass associations, the desired mix on engineered covers. Franklin and Dyrness (1988) reported a ground cover range of 8 to 35% and an average cover of 24% for such associations.

Also shown in Table 5.7 are data from the prototype Hanford Barrier for the period 2002 through 2007. There were no measurements in 2005 or 2006. On the southern (non-irrigated) half of the barrier, percent cover by forbs and grass was very low, but shrubs accounted for nearly 32%. Litter and bare soil were essentially the same while soil cryptogam cover was significantly higher than bare soil. Bare-soil cover was calculated as the sum of soil and soil cryptogam cover. The prototype barrier continues to show a high cover of native plants 13 years after the initial restoration effort. Sagebrush is the most common

Table 5.7. Percentage Cover For Sagebrush/Grass Ecosystems at the Hanford Site

Year	Location	Percent Cover				
		Desert Shrubs	Grass	Forbs	Litter	Bare Ground
1998	ILAW Site	32.0	42.2	8.4	NA	19.9
1998	Grout Site	29.6	30.9	3.1	NA	34.8
2002	Barrier	18.9	5.90	2.5	27.0	38.8
2003	Barrier	41.4	15.9	2.5	20.2	63.2
2004	Barrier	33.8	17.3	2.5	29.1	55.1
2005	Barrier	NA	NA	NA	NA	NA
2006	Barrier	NA	NA	NA	NA	NA
2007	Barrier	31.9	3.39	2.5	26.9	30.8

plant on the surface, essentially forming a monoculture. Shrub cover (mostly sagebrush) has remained unchanged from the period 1997 to 2007, and forbs were most often found in association with grasses.

Plant community dynamics, including changes to the mixture of plant species and in the abundance and density of individual species, can be expected on engineered covers. For example, annual grass and forb canopies are known to vary greatly from year to year depending on rainfall. Long-term changes in plant communities usually occur in response to climatic changes, and such changes could significantly affect long-term barrier performance (Link et al. 1995). Thus, the composition of communities in natural areas could provide insight into the long-term composition and density of species on revegetated covers. Table 5.8 summarizes the canopy cover by plant species at three locations on the Hanford site.

Table 5.8. Canopy Cover by Main Plant Growth Forms at Various Places at the Hanford Site

Location	Percent Cover					
	Desert Shrubs	Bunch Grass	Annual Grass	Perennial Forbs	Annual Forbs	Total
Cold Creek, 200 Area	20	13	12	< 1	< 1	46
B-C Cribs, 200 Area	18	2	19	1	14	54
Supply System, 300 Area	26	10	56	4	28	124(a)
(a) Exceeds 100% cover because of overlapping layers of canopy.						

These data can be used to calculate the ground fractional cover or plant area index for STOMP simulations involving multiple plant species. The calculated fractional ground-cover values are shown in Table 5.9. Note that Link et al. (1995) did not report bare-ground percentages. Therefore, these calculations assume that the difference between 100% ground cover and the total canopy cover is bare ground. Owing to this assumption, data from the Supply System 300 Area site were not included in the calculations. Annual and bunchgrass percentages were summed to allow comparison to sites at which grasses were not differentiated; the same was done for annual and perennial forbs.

Table 5.9. Fractional Ground Cover (Plant Area Index) for Main Plant Growth Forms at Various Places at the Hanford Site

Location	Plan Area Index			
	Desert Shrubs	Grass	Forbs	Bare Ground
Barrier	0.47	0.05	0.04	0.45
ILAW Site	0.31	0.41	0.08	0.19
Grout Site	0.30	0.31	0.03	0.35
Cold Creek, 200 Area	0.20	0.25	0.01	0.54[†]
B-C Cribs, 200 Area	0.18	0.21	0.15	0.46[†]

Table 5.9 clearly shows that the prototype barrier is not representative of the typical sagebrush-bunchgrass vegetation zone as the desert shrubs (mostly sagebrush) forms a monoculture. The plant-area index is also significantly higher than the natural sites. No forbs were included in the mix of plants used in the revegetation program, which perhaps accounts for the low-percentage of forb cover at the barrier. However, these species contribute significantly to the diversity at the natural sites. The best-estimate values of plant-area index in Table 5.9 can be used in parametric studies of the impact of plant community dynamics.

5.5 Root Distributions

Understanding and predicting barrier performance requires an accurate assessment of plant root distributions. Root distributions can be expected to vary by plant functional groups (shrubs vs. grasses, vs. forbs), but the data available to assess the distributions for native plant species at Hanford are quite limited. Root-distribution measurements at the prototype barrier are limited to vertical distributions measured in rhizotrons and do not provide the species-specific data needed for model parameterization. Other data from across the site were mostly one-dimensional and insufficient to parameterize multi-dimensional forms of the root-distribution model.

To allow parameterization of the multi-dimensional form of the Vrugt et al. (2001) root model for the various species of plants proposed for use on engineered barriers, we used observations of root distributions reported in the literature. Schenk and Jackson (2002) provided a comprehensive literature synthesis of rooting depths, lateral root spread, and below-ground to above-ground biomass ratios that have proven useful in estimating root distributions by plant functional groups. The database consists of over 1300 records of root-system sizes for plant functional groups collected from different precipitation zones. It was concluded that root-system sizes differed among growth forms and increased with above-ground size according to annuals < perennial forbs = grasses < semi-shrubs < shrubs. Absolute rooting depths increased with mean annual precipitation (MAP) in all plant functional groups except shrubs. In general, root systems tended to be shallower and wider in dry and hot climates and deeper and narrower in cold and wet climates. Shrubs were more shallowly rooted under climates with summer than winter precipitation regimes.

Using an independent data set of 20 test locations, Schenk and Jackson (2002) predicted rooting depths from MAP using regression models for three broad growth forms. These models were successful in explaining 62% of the observed variance in median rooting depths and are therefore used to estimate rooting characteristics for species without site-specific data. Rainfall was a much stronger predictor for

rooting depth than mean annual evapotranspiration (PET) in all growth forms. Regression parameters for the relationships between root-system dimensions, MAP, and mean annual potential evapotranspiration are shown in Table 5.10. The parameters are for the linear equations:

$$\log_{10} Y = a + b \log_{10} MAP \tag{5.2}$$

where Y is the respective root variable in meters, i.e., rooting depth (z_m), lateral root spread (r_m), or ratio of lateral spread to rooting depth (r_m/z_m); MAP is mean annual precipitation in mm (160 mm for Hanford); and PET is mean annual evapotranspiration in mm. For simulations involving multi-dimensional root distributions as well as vertical and lateral root extent, Table 5.10 should be used to estimate root-system dimensions.

Table 5.10. Regression Parameters for the Relationships Between Root System Dimensions and Mean Annual Precipitation (> 50 to ≤1000 mm). Statistically significant parameters are marked by *($P < 0.05$), **($P < 0.01$), or *** ($P < 0.001$). Calculated values of Y are for Hanford conditions assuming a mean annual precipitation of 160 mm.

Rooting Depth	**a**	**b**	**r^2**	**Y (m)**
Annuals	-2.312	0.809***	0.265***	0.296
Perennial forbs	-1.603	0.629***	0.136***	0.607
Perennial grasses	-1.053	0.409***	0.111***	0.705
Semi-shrubs	-0.316	0.178*	0.018*	1.192
Shrubs	-0.053	0.158	0.007	1.974
Lateral Root Spread				
Annuals	-3.096	0.919***	0.253***	0.085
Perennial forbs	-1.029	0.196	0.009	0.253
Perennial grasses	-0.020	-0.180	0.008	0.383
Semi-shrubs	1.273	- 0.638***	0.171***	0.736
Shrubs	0.279	0.020	0.000	2.104
Lateral: Depth Ratio				
Annuals	-0.684	0.056	0.000	0.275
Perennial forbs	0.585	- 0.434***	0.064***	0.425
Perennial grasses	1.040	- 0.589***	0.132***	0.552
Semi-shrubs	1.316	- 0.701***	0.192***	0.590
Shrubs	0.679	-0.287	0.008	1.113

Link et al. (1995) summarized information related to maximum rooting depths for a plant species that could live on barrier surfaces at Hanford. For this report, maximum rooting depths were reclassified according to plant functional groups and are presented in Table 5.11. The maximum root depths from Table 5.11 can be used with the lateral root spread from Table 5.10 in parameterization of the root-distribution model.

In addition to maximum root depth and lateral spread, information on variations of root-length density is needed to obtain the best parameters for the model. Root density (biomass/volume of soil) data have also been summarized by Link et al. (1995) based on studies conducted at several field sites at Hanford by Klepper et al. (1985) and Downs et al. (1993). These data were fitted to the Vrugt et al. (2001) root-distribution model to obtain the best-fit parameters for STOMP input. The fitted parameters for the one-dimensional root-distribution model are summarized in Table 5.12.

5.5.1 Transpiration-Reduction Function

Transpiration in shrub/grass associations on engineered covers is not yet well understood, and the few existing data are difficult to extrapolate temporally and spatially. Predicting root water uptake under water-stressed conditions requires parameterization of the transpiration-reduction function. Depending on the model, the required parameters are either four pressure head stress points, h_1, h_2, h_3, and h_4, or the matric potential at which uptake declines by 50%, h^*, and the proportionality constant, k, that determines the steepness of the curve. These parameters are typically difficult to determine, and documented values are mostly for agricultural crops (e.g., Taylor and Ashcroft 1972).

Most of the terms in the transpiration reduction functions can be computed from equations given by Norero (1969), but it is recommended that they be determined experimentally. However, owing to the limited data for shrub-steppe ecosystems, values of the critical matric potentials are estimated from those with similar growth forms with the exception of the wilting point, h_4. This is because the wilting point is typically lower than that for crop species. It is known that native shrubs are able to concentrate their cell sap with compounds that will facilitate water uptake under very dry conditions (Link et al. 1994). For example, the desert shrub *Larrea tridentata* (creosote bush) maintains photosynthesis and transpiration at -7.0 to -8.0 MPa under field conditions (Yan et al. 2000), well below the wilting point of traditional crop plants. Other desert shrubs (*Atriplex confertifolia* and *Ceratoides lanata*) can extract water from soils at -8.0 MPa (Caldwell et al. 1977). There are also reports of desert shrubs surviving at water potentials of -10.3 to -12.0 MPa (e.g., MacMahon and Schimpf 1981). Leaf-water potentials as low as -4.8 MPa have been measured on cheatgrass at Hanford (Link et al. 1990). In general, forbs that are physiologically active in the summer remain green and can extract water down to around 70 bars (-7 MPa) (Steven Link personal communication). Many desert shrubs transpire as much as 15% of total transpiration through their stems, although the model does not explicitly account for this. This phenomenon can be accounted for by increasing the leaf area index by 15%. Values of h_3 are estimated from the published values of h_3^{high} for crop species with similar growth forms, i.e., the value of h_3 at which a reduction in water uptake starts at high potential transpiration. van Genuchten (1987) proposed a value of 3500 cm for h^* and k between 1.5 and 3.0, but these recommendations are also for crop plants. Thus, k is calculated from h_1 and h_4 according to Norero (1969) and Taylor and Ashcroft (1972).

$$k = \frac{2.56}{\log\left(\frac{h_4}{h_1}\right)} \tag{5.3}$$

Table 5.11. Maximum Observed Rooting Depths of Species Proposed for Use on Engineered Barriers at the Hanford Site (after Link et al. 1995)

Growth Form	Duration	Species	Common Name	Site	Soil Type	Z (m)
Forb	Annual	*Lactuca serriola*	Prickly Lettuce	200 Area	sandy-loam to sand	0.85
Forb	Annual	*Sisymbrium altissimum*	Tumble Mustard	PUREX Pit Face	sandy-loam to sand	0.97
Forb	Annual	*Ambrosia acanthicarpa*	Bursage	PUREX Pit Face	sandy-loam to sand	1.32
Forb	Annual	*Salsola kali*	Russian Thistle	PUREX Pit Face	sandy-loam to sand	1.37
Forb	Annual	*Ambrosia acanthicarpa*	Bursage	200 Area	sandy-loam to sand	1.62
Forb	Annual	*Salsola kali*	Russian Thistle	200 Area	sandy-loam to sand	1.72
Grass	Annual	*Bromus tecorium*	Cheatgrass	300 N Grass	loamy-sand to sand	0.50
Grass	Annual	*Bromus tecorium*	Cheatgrass	Lower Snivley	silt-loam	0.60
Grass	Annual	*Bromus tecorium*	Cheatgrass	Lower Snivley	silt-loam	0.80
Forb	Perennial	*Cymopteris terebinthinus*	Turpentine Cymopterus	200 Area	sandy-loam to sand	1.45
Forb	Perennial	*Eriogonum viniveum*	Snow Buckwheat	200 Area	sandy-loam to sand	1.50
Forb	Perennial	*Balsamorhiza careyana*	Carey's Balsamroot	200 Area	sandy-loam to sand	1.50
Forb	Perennial	*Aster canescens*	Hoary Tansyaster	200 Area	sandy-loam to sand	1.55
Grass	Perennial	*Poa sandbergii*	Sandberg's Bluegrass	300 N Grass	loamy-sand to sand	0.35
Grass	Perennial	*Oryzopsis hymenoides*	Indian Rice grass	200 Area	sandy-loam to sand	1.25
Grass	Perennial	*Hesperostipa comata*	Needle-and-thread grass	200 Area	sandy-loam to sand	1.60
Shrub	Perennial	*Chrysothamnus viscidiflorus*	Yellow Rabbitbrush	200 Area	sandy-loam to sand	1.60
Shrub	Perennial	*Artemisia tridentata*	Big Sagebrush	PUREX Trench	sandy-loam to sand	1.70
Shrub	Perennial	*Chrysothamnus nauseous*	Gray Rabbitbrush	200 Area	sandy-loam to sand	1.83
Shrub	Perennial	*Grayia spinosa*	Spiny Hopsage	200 Area	sandy-loam to sand	1.95
Shrub	Perennial	*Artemisia tridentata*	Big Sagebrush	200 Area	sandy-loam to sand	2.00
Shrub	Perennial	*Artemisia tridentata*	Big Sagebrush	McGee Ranch	silt-loam	2.00
Shrub	Perennial	*Grayia spinosa*	Spiny Hopsage	McGee Ranch	silt-loam	2.00
Shrub	Perennial	*Artemisia tridentata*	Big Sagebrush	Pit 29 Trench	sandy-loam to sand	2.30
Shrub	Perennial	*Chrysothamnus nauseous*	Gray Rabbitbrush	200 Area	loamy-sand to sand	2.40
Shrub	Perennial	*Artemisia tridentata*	Big Sagebrush	Purex Trench	sandy-loam to sand	2.60
Shrub	Perennial	*Artemisia tridentata*	Big Sagebrush	200 Area	sandy-loam to sand	3.00
Shrub	Perennial	*Artemisia tridentata*	Big Sagebrush	FLTF	silt to rock at depth	3.00

Table 5.12. Fitted Model Parameters of the Vrugt et al. (2001) Root Distribution Model for Different Plant Growth Forms Expected to Grow on Engineered Barriers

Growth Form	z_m (m)	z^*	p_z	SSE
Annual Forb	1.32	0.3949	1.087	0.06568
	1.72	0.4880	2.266	0.00170
	2.00	0.5211	3.379	0.00003
Annual Grass	0.5	0.0590	0.0590	0.00523
	0.6	0.0563	0.0563	0.00415
	0.8	0.0538	0.0538	0.00355
Perennial Forb	1.55	0.5139	0.4077	0.00046
	2.00	0.4214	0.1275	0.00762
Perennial Grass				
	0.35	0.1157	3.1565	0.01436
	0.40	0.0709	2.6160	0.01032
	1.25	-0.5840	1.6504	0.01391
	1.60	-0.4509	2.7056	0.01317
Sagebrush				
	1.60	1.866	0.498	0.00536
	1.70	2.096	0.515	0.00227
	1.83	2.279	0.456	0.00080
	2.00	3.284	0.545	0.00211
	2.40	5.056	0.567	0.00004
	2.60	5.739	0.566	0.00002
	3.00	5.417	0.401	0.00037
Rabbitbrush	1.60	3.825	1.007	0.02192
	1.70	3.443	1.032	0.01393
	1.83	3.904	1.004	0.00368
	2.00	4.675	0.962	0.00298
	2.40	5.144	1.082	0.00656

The recommended values for parameterizing the transpiration-reduction functions are shown for the different plant growth forms in Table 5.13. For annual and perennial grasses, the value of h_3 is set equal to h_3^{high} for crops of small grains during ripening (-8000 cm). Annual forbs (e.g., prickly lettuce [*Lactucia serriola*]) is assigned the h_3^{high} value of cultivated forbs in their productive phase (-3000 cm). For perennial forbs, h_3 is set equal to h_3^{high} cultivated perennial forbs (-4000 cm). A cultivated plant analogous to a shrub could not be identified, so the value of h_3 for shrubs was set equal to alfalfa during ripening (-8000 cm). The value of h_2 is set equal to the air-entry pressure for the silt-loam soil as the soil will remain saturated at pressures lower than the entry pressure. The h_2 calculated as the inverse of the mean value of α (0.01 cm^{-1}) from Table 3.16 is 100 cm.

Table 5.13. Best-Fit Parameters for the Critical Values of Soil Water Pressure Heads for the Transpiration Reduction Functions

Growth Form	ψ_1 (cm)	ψ_2 (cm)	ψ_3 (cm)	ψ_w^* (cm)	ψ_4 (cm)	k
Annual Forb	-10.00	-100.00	-3000.00	-3500.00	-7.14×10^4	0.664
Annual Grass	-10.00	-100.00	-8000.00	-3500.00	-4.89×10^4	0.694
Perennial Forb	-10.00	-100.00	-4000.00	-3500.00	-7.14×10^4	0.664
Perennial Grass	-10.00	-100.00	-8000.00	-3500.00	-4.89×10^4	0.694
Shrubs	-10.00	-100.00	-8000.00	-3500.00	-8.67×10^4	0.650

5.6 Plant Growth Cycle

The plant phenology or seasonal development is an important component of barrier simulation and is captured in the parameters defining the developmental stages. Phenology is quite variable among species and growth forms. Link et al. (1995) identified native species at the McGee Ranch and the 200 Area plateau used to revegetate the prototype Hanford barrier in the 200-BP-1 operable unit. These species can be classified into five main growth forms—annual forbs, annual grasses, perennial forbs, perennial grasses, and shrubs—all with different phenologies. The generalized phenology of these species is used to derive the input parameters for the STOMP simulator.

5.6.1 Forbs

Forbs are herbaceous broad-leaved flowering plants that are not grasses. Forbs are generally of low importance in the semi-arid shrub-steppe ecosystem. Annual forbs tend occur in the short understory layer whereas perennial forbs constitute the tall understory layer. Forbs are particularly important because their growing points are located below the soil surface and are therefore insulated from heat injury. The degree of damage sustained by forbs is proportional to the intensity and duration of the fire that affects these growing points. The ability of these plants to survive fire and their post-fire regrowth from subsurface surface tissue make them attractive for revegetation of engineered barriers. Studies of prescribed burns in big sagebrush communities have reported that forbs increase rapidly and exceed pre-burn production by post-burn year 3 (FEIS). The generalized phenology of annual and perennial forbs is presented below.

5.6.1.1 Annual Forbs

Tumble mustard (*Sisymbrium altissimum*) is chosen to represent annual forbs. Tumble mustard is a broad-leaved annual occurring in disturbed plant communities and in sagebrush communities. Tumble mustard is a winter annual or biennial and reaches a height of 1.5 m (4.9 feet) or more in height. Tumble mustard has a thick taproot, and the maximum root depth observed at Hanford is 0.97 m (38 inches). Tumble mustard germinates in winter or early spring, before most associated herbaceous species have started. Tumble mustard seeds germinate at temperatures from 0 to 20°C (32 to 68°F).

The flowering period is lengthy, and a single plant typically bears numerous stalked flowers. The flowers mature quickly with relatively few in bloom at once. The lower leaves usually dry out around flowering time without affecting flower production. The generalized phenology is described in Table 5.14.

Table 5.14. Phenology of Tumble Mustard

Approximate Date	Day of Year	Phenology Event
March 1	60	Germination
March 21	80	Shoot growth starts
April 27	117	Flower stalks appear
May 15	135	Flower heads fully out
June 5	156	Flowers in bloom
June 26	177	Seeds ripe
June 30	181	Seed Dissemination Starts
July 9	190	Senescence

Tumble mustard may be top-killed by fire, but if the root crown is not damaged, the plant can sprout new basal leaves from the root crown. As an annual with a single stem, tumble mustard lacks adaptations for re-growth once it has bolted, and plants burned after the rosette stage are killed. Tumble mustard establishes from soil-stored seed after fire. Fire also tends to create conditions favorable for establishment, i.e., bare soil, open canopy, and reduced growth interference (FEIS).

5.6.1.2 Perennial Forbs

Leafy spurge (*Euphorbia esula*) is not typically found at Hanford but was chosen as a representative for perennial forbs, mainly because of the amount of available information. Leafy spurge is a perennial forb that generally grows in clumps. Stems are tough and woody with variable degrees of branching and typically grow to about 0.9 m (3 feet) tall. Leafy spurge has an extensive underground rhizome and root system. Roots can penetrate into the soil as deep as 4.6 to 9 m (15 to 30 feet). Deep rooting and thick, the corky root bark helps establish drought resistance (FEIS).

Spring growth begins as early as March 20 with the production of adventitious shoots arising from the seedling root system and continues until the middle of June. Flowering shoots appear in late April to May and occurs throughout the growing season with obvious inflorescences by June. By July, an increase in the production of flowering shoots leads to a decrease in vegetative growth. Fruit matures after 4 to 6 weeks, usually late June or early July, with dispersal occurring from July to August. Late-season flowering shoots may form in August, with fruit maturing from September to October. Senescence occurs in the late fall (FEIS). A generalized phenology is described in Table 5.15.

Table 5.15. Phenology of Leafy Spurge

Approximate Date	Day of Year	Phenology Event
February 24	55	Dormancy ends
March 20	79	Leaf growth starts
April 24	114	Flower buds
June 1	152	Flowers in bloom
July 1	182	Seeds filled
July 15	196	Seeds ripe
October 31	304	Seed dissemination
November 24	328	Senescence

After fire that kills the above-ground portions, leafy spurge can sprout from the roots, rhizomes, and root crown. Fire may increase leafy-spurge density by promoting the sprouting of previously dormant buds along the extensive rhizome and root system. Leafy spurge also establishes through seed after fire, although fire may reduce germination.

5.6.2 Grasses

By definition, shrub steppe consists of a discontinuous layer of shrubs and one or more layers of perennial grasses. At Hanford, the common association is sagebrush-wheatgrass and sagebrush bluegrasses with a component of broad-leaved forbs. In addition, there are areas with widespread intrusion of non-native annual grasses such as cheatgrass (*Bromus tectorum*). Annual and perennial grasses are therefore important to the revegetation process and model parameterization. Representative species are chosen from grasses of each duration for model parameterization. These include Indian Ricegrass, thickspike wheatgrass, needle-and-thread grasses, Sandberg bluegrass, and cheatgrass. The generalized phenology of these species is presented below.

5.6.2.1 Indian Ricegrass

Indian ricegrass (*Oryzopsis hymenoides*) is a native, cool-season perennial bunchgrass. It is densely tufted and grows from 10 to 61 cm (4 to 24 inches) in height. The canopy spread is typically 20 to 30 cm (8 to 12 inches). Indian ricegrass has deep, fibrous, extensive roots that reach depths of 150 cm and is one of the most drought tolerant of the native range grasses (FEIS). The plant can produce green shoots in fall and generally stays dry until late winter or early spring when new growth begins. It is short-lived with growth usually declining by the fifth year with a maximum age of 30 years (FEIS). Growth starts in early spring with flowers forming in May. Studies performed by Pearson (1979) found that growth in the spring begins when soil temperatures at the 15-cm depth have warmed up to 4°C and remain at or above that temperature for at least 3 or 4 days. Flowering can continue through the spring and summer if growing conditions are favorable. In the Upper Snake Plains of southern Idaho, seed dissemination begins in early July and is complete by late July. By early August, the plant has dried but may still produce new growth again in the fall. The plant will stay dry through the winter until new growth begins in the spring. A generalized phenology for Indian ricegrass based on data collected in the Upper Snake River Plain of southern Idaho (Blaisdell 1958) is shown in Table 5.16.

Table 5.16. Phenology of Indian Ricegrass

Approximate Date	Day of Year	Phenology Event
March 31	90	Dormancy ends
April 8	98	Growth starts
May 22	142	Flower stalks appear
June 17	168	Flower heads fully out
June 20	171	Flowers in bloom
July 3	184	Seeds ripe
July 6	187	Seed Dissemination Starts
August 6	218	Senescence

Indian ricegrass is only moderately damaged by fire and may regenerate from seed or the surviving perennial crown following fire. In western and central Utah, Indian ricegrass is reported to represent important cover on burned areas and often exhibits good growth characteristics. A low density of culms

(stems) reduces the charring of crowns below soil, thereby protecting growing points. Wildfires in Utah and Nevada reduced the basal area of Indian ricegrass, but little mortality was observed (FEIS). These rapid postfire responses suggest that Indian ricegrass may also sprout from tillers.

5.6.2.2 Thickspike Wheatgrass

Thickspike wheatgrass (*Elymus lanceolatus*) is a long-lived, cool-season, native perennial grass. Culms are erect and grow 15 to 130 cm (6 to 50 inches) tall. Thickspike wheatgrass is a sod-forming grass with a broad rhizome system and few deep roots. Growth typically begins in early spring with flowering occurring from May through July. Seeds mature from July to early August. Seed dispersal occurs through August with the plant becoming dormant sometime soon after. A generalized phenology based on data collected by (Blaisdell 1958) in study in the Snake River Plains of Idaho is presented in Table 5.17.

Table 5.17. Phenology of Thickspike Wheatgrass

Approximate Date	Day of Year	Phenology Event
March 21	80	Dormancy ends
April 1	91	Growth starts
May 21	141	Flower stalks appear
June 16	167	Flower heads fully out
June 27	178	Flowers in bloom
July 27	208	Seeds ripe
August 8	220	Seed Dissemination Starts
August 11	223	Senescence

Thickspike wheatgrass is initially injured by fire but because its roots can survive fire and the plant produces new above-ground growth each year, it can recover within 1 to 5 years. Compared to pre-fire conditions, production may increase 2 to 3 times or more within a 3 to 4 year period after fire (FEIS). After planned fires in big sagebrush-grass habitat, thickspike wheatgrass spreads quickly and may dominate the ground cover.

5.6.2.3 Needle-and-Thread Grass

Needle-and-thread grass (*Hesperostipa comata*) is a medium-sized, cool-season, native, perennial bunchgrass. Bunches are widely spaced and range in size from 2.5 to 7.6 cm (1 to 3 inches) in diameter. Seed stalks can reach 10 to 100 cm (12 to 36 inches) in height, but the leaves are mostly basal. Needle-and-thread grass begins to grow in early spring with flowering beginning in mid-May. Seeds ripen by early July, and dissemination occurs from early to mid-July. By early August, complete drying of the plant has occurred, but it will green up again in the fall given sufficient precipitation. Blaisdell (1958) measured seasonal development on Idaho's Upper Snake River Plain. These results were used as the basis of the generalized phenology, which is shown in Table 5.18.

Needle-and-thread grass is top-killed by fire and may suffer slight damage. The plant becomes more resistant to burning from spring through summer as tissues dry out and root storage of carbohydrates increases (FEIS). Needle-and-thread sprouts from the underground stem following fire. Post-fire productivity and coverage have been reported to decrease for 1 season and then increase in the following year.

Table 5.18. Phenology of Needle-and-Thread Grass

Approximate Date	Day of Year	Phenology Event
March 21	80	Dormancy ends
April 4	94	Growth starts
May 21	141	Flower stalks appear
June 18	169	Flower heads fully out
June 22	173	Flowers in bloom
July 1	182	Seeds ripe
July 4	185	Seed Dissemination Starts
August 1	213	Senescence

5.6.2.4 Sandberg Bluegrass

Sandberg bluegrass (*Poa secunda*) is a relatively short-lived, shallow-rooted, cool-season perennial bunchgrass. It is senescent and dormant during the dry hot summer and becomes green and active after fall rains. As temperatures drop in the winter, Sandberg bluegrass maintains green leaves but remains quiescent. The plant completes spring growth earlier than many other perennial grasses. Because it is a shallow-rooted species, it must complete growth and seed production before available soil moisture has been depleted on summer-dry soils. In eastern Washington, Sandberg bluegrass has two periods of maximum leaf height: midwinter and May (Daubenmire 1972). Leaves begin growing in the fall as soon as rains begin, although soaking rains are not necessary to initiate growth. There is a decline in growth after midwinter that can be attributed to the senescence of fall leaves. Cessation of growth coincides with the depletion of soil moisture in the top 10 cm (4 inches) of soil. Data collected from 1941 to 1947 on the Upper Snake River Plain of Idaho by Blaisdell (1958) suggest a generalized sequence as in Table 5.19.

Table 5.19. Phenology of Sandberg Bluegrass

Approximate Date	Day of Year	Phenology Event
February 25	55	Dormancy ends
March 30	94	Growth starts
April 27	117	Flower stalks appear
May 15	135	Flower heads fully out
June 5	156	Flowers in bloom
June 26	177	Seeds ripe
June 30	181	Seed Dissemination Starts
July 9	190	Senescence

Sandberg bluegrass is generally unharmed by fire. Because of the small bunch size and sparse litter production, the amount of heat transferred to subsurface buds is small and secures its survival. Rapid maturation in the spring and the fact that it is dormant when most fires occur also reduces fire damage. Groundcover of Sandberg bluegrass generally increases after fire (FEIS). Measurements in southeastern Oregon show that 4 years after an August wildfire in a big sagebrush-bunchgrass community, Sandberg bluegrass and other bunchgrasses dominated burned sites.

5.6.2.5 Cheatgrass

Cheatgrass (*Bromus tectorum*) is highly adapted to a regime of frequent fires and is successful at invading and dominating natural communities. Cheatgrass is a non-native winter annual that germinates in the fall, if climatic conditions are favorable, or in the following spring, securing annual recruitment. Cheatgrass reproduces by seed that germinates in the fall with the first effective rain. After fall germination, cheatgrass plants grow rapidly until cold temperatures arrive after which it over winters as a seedling. In southern Idaho, about 50 mm (2 inches) of concentrated early fall precipitation is required to stimulate about 5 to 10 cm (2 to 4 inches) of fall growth (FEIS). Cheatgrass roots continue to develop during winter, while aboveground growth is minimal. Rapid elongation of roots provides cheatgrass with a competitive advantage over native perennial species. Cheatgrass is a more an efficient user of soil water in the upper 0.5 m of soil than native bunchgrasses. However, the bunchgrasses extract water from deeper in the soil profile. Cheatgrass is more successful that native species at mining water and nutrients in the early spring since cheatgrass is actively growing when the native species are just initiating growth.

Shoot growth typically occurs in late winter or early spring and continues until soil moisture is exhausted. Where moisture, fertility, or light intensity are non-limiting, cheatgrass plants may produce 12 to 15 stalks that grow 50 to 75 cm (20 to 30 inches) tall. Cheatgrass also completes its reproductive process and becomes senescent before most native plants. In mild winter weather, cheatgrass plants can tiller and produce many adventitious roots. As a winter annual, cheatgrass usually flowers in spring, from mid-April through June, and flower heads open over about an 11-day period. Seeds ripen in June or July and dispersal starts within a week of maturity. Plants die and become dry after seeds are ripe, or after early summer drought. In the Columbia basin, senesce typically occurs by mid-May to early June. A generalized phenology is summarized in Table 5.20.

Table 5.20. Phenology of Cheatgrass

Approximate Date	Day of Year	Phenology Event
September 30	273	Germination
December 15	349	Root elongation
March 15	74	Shoot growth starts
April 15	105	Flower stalks appear
April 25	115	Flower heads fully out
April 30	120	Flowers in bloom
May 12	132	Seeds ripe
June 15	135	Seed Dissemination Starts
May 31	151	Senescence

Corresponding stages are about 6 weeks later in bluebunch wheatgrass. In hot weather, cheatgrass roots are unable to supply enough moisture to prevent a drop of leaf-water potential, resulting in desiccation and death of the plant. The short growth period of cheatgrass relative to native plants also increases the likelihood of wildfire starts and spread.

5.6.3 Desert Shrubs

Native shrubs found within the Hanford Reservation that potentially could grow on barrier surfaces include the shrubs *Artemisia tridentata* (big sagebrush), *Purshia tridentata* (bitterbrush), *Chrysothamnus nauseosus* (gray rabbitbrush) and *Grayia spinosa* (spiny hopsage). These three species are used to

represent the phenology of shrubs and to obtain the input parameters for simulation of barrier performance.

5.6.3.1 Big Sagebrush

Sagebrush is a perennial shrub common to the McGee Ranch and 200 Area Plateau and critical to revegetation efforts on engineered covers. Big sagebrush is an erect, rounded evergreen shrub that normally grows 1 to 2 m (3 to 10 feet) in height (FEIS). It commonly reaches 40 to 50 years of age, and some plants may exceed 100 years. Slow-growing individuals on unfavorable sites attain the greatest age. The root systems are well adapted to extract moisture from both shallow and deep portions of the soil profile, making sagebrush highly competitive in grass and forb associations (FEIS)

Vegetation starts in late February to early March. As growth continues, new short lateral branches form from the existing stem and support smaller leaves that persist throughout the next winter, long after the initial leaves are shed. In Washington, accentuated stem growth begins in late May with maximum longitudinal stem growth occurring in early June. By the end of June, vegetative stem growth begins to decline as reproductive buds and shoots begin expansion (FEIS). Big sagebrush flowers from July to October, and reproductive shoots reach maximum size; flower buds first appear in late July. Seed production occurs from October to December. Most seed is shed in the fall, although some may remain on the plant through the winter. Seeds germinate in the spring, as early as April. Seasonal development in the valley of Alpowa Creek near Clarkston, Washington, as reported by DePuit and Caldwell (1973), is presented as a generalized phenological sequence in Table 5.21.

Table 5.21. Phenology of Big Sagebrush

Approximate Date	Day of Year	Phenology Event
March 1	60	Dormancy ends
March 15	74	Leaf growth starts
April 30	120	Twig growth starts
September 1	244	Flower buds
July 8	189	Flowers in bloom
October 31	304	Seeds filled
November 15	319	Seeds ripe
November 30	327	Seed dissemination

Big sagebrush is readily killed when aboveground plant parts are charred by fire. Exposure to temperatures above 195 degrees Fahrenheit (90^{o}C) for longer than 30 seconds will kill the plant. In some areas, particularly those where the soil is thin and rocky, the sparse biomass typical of bunchgrasses may limit the spread of fire, resulting in scattered survivors. Big sagebrush does not resprout after fire, and because of the time needed to produce seed, it can be eliminated by frequent fires. The rate of recovery depends on the season of burn, as this affects seed availability, postfire precipitation patterns, and the degree of competition from other plant species.

5.6.3.2 Rabbitbrush

Gray rabbitbrush (*Chrysothamnus nauseosus*) is a perennial shrub that is typically associated with big sagebrush. Rabbitbrush is also common to the McGee Ranch and is expected to thrive on engineered barriers. It is an erect round or pyramidal native shrub that typically reaches 31 to 229 cm (12 to

90 inches) in height, although certain populations have been reported to reach 3.3 to 3.6 m (10 to 12 feet) in height (FEIS). Rabbitbrush exhibits a number of adaptations for surviving in an arid environment. Leaves and stems are covered with a felt-like layer of hair-like outgrowths that insulate the plant and reduce transpiration.

Germination occurs from March through June, and bud burst on dormant plants may occur as early as late February, but usually occurs in late March or early April (FEIS). Restricted growth continues until May, and accelerated growth occurs from May until early or mid-August. Photosynthesis continues through the summer drought period. Flower bud initiation takes place in early- to mid-summer with flowering from mid-summer to fall. Populations from cold deserts typically flower in July. Seed ripens from late fall to early winter, and seed set occurs in late September at higher elevations and in late November at low-elevation Mojave Desert sites. Seed dissemination starts before all flowers are fully mature (FEIS). Based on a study at Hot Creek Valley, Nevada, a generalized phenological sequence may be described as in Table 5.22 (Everett et al. 1980).

Table 5.22. Generalized Phenology of Rabbitbrush

Approximate Date	Day of Year	Phenology Event
February 24	48	Dormancy ends
March 1	60	Leaf growth starts
March 31	90	Twig growth starts
May 31	151	Flower buds
July 8	189	Flowers in bloom
August 18	230	Seeds filled
September 11	254	Seeds ripe
October 5	278	Seed dissemination

Because of the relatively high resin content, both foliage and stems of rabbitbrush may be consumed by fire, even at fairly high moisture content, and the plant is often top-killed (FEIS). Mortality after fire is variable but is often very low. Nonetheless, rabbitbrush is a fire-adapted species that is typically unharmed or enhanced by fire (FEIS). After a fire, rabbitbrush can regenerate either by sprouting from adventitious buds located on the stem and root crown or from or from offsite seed. Fires with high intensities or long residence time may kill buds located at or near the root crown, limiting the ability to resprout (FEIS).

5.6.3.3 Spiny Hopsage

Spiny hopsage (*Grayia spinosa*) is a relatively long-lived perennial shrub that is well adapted to sagebrush deserts. It commonly occurs in fairly pure stands or in large extensive tracts with big sagebrush and is common to the McGee Ranch and 200 Area. It is a woody, erect, diffusely branched native shrub that reaches heights of 0.3 to 1.5 m (1 to 5 feet). The root system is shallow and spreading. In the Pacific Northwest, it is deciduous in the summer. Fall rains and/or periods of low temperatures ranging from 41 degrees Fahrenheit (5^{o}C) to below 32 degrees Fahrenheit (0^{o}C) usually breaks dormancy (FEIS). The first date of fruiting ranges from early March to mid April with a mean date of April 2. Fruit maturity typically occurs by mid-July, just before leaf fall. Bud formation, leaf fall, and the onset of summer dormancy usually occur after seed dispersal. Dormancy in spiny hopsage is one of the longest of desert shrubs. The plant remains dormant throughout the hot, dry summer months. In southern Nevada, Ackerman et al. (1980) found that spiny hopsage became dormant when daytime air temperatures

exceeded 104°F (40°C), and summer rains failed to reinitiate new leaf growth. A generalized phenological sequence may be described as in Table 5.23.

Spiny hopsage is considered to be somewhat fire tolerant and may survive fires that typically kill sagebrush (FEIS). The plant regenerates by sprouting after top-killing disturbances such as fire. Sprouting may occur when mature plants are burned off at the soil surface. Even plants that appeared dead have been reported to re-sprout several years after a wildfire near the Snake River (FEIS). Observations at Hanford suggest that it is completely killed by wildfires and there is no regeneration unless the burn severity is very low. Spiny hopsage also regenerates from wind or gravity-dispersed winged seed, which is produced annually.

Table 5.23. Generalized Phenology of Spiny Hopsage

Approximate Date	Day of Year	Phenology Event
February 24	55	Dormancy ends
February 28	59	Leaf growth starts
March 1	60	Twig growth starts
April 7	97	Flower buds
April 10	100	Flowers in bloom
April 30	120	Seeds filled
June 1	152	Seeds ripe
June 15	166	Seed dissemination
June 18	169	Senescence

5.7 Transpiration Coefficient

Seasonal development is handled by coupling plant phenology with the temporal distribution of the transpiration coefficient, K_c (Figure 2.5). Values of K_c must then be assigned to the different phases of the developmental cycle. The temporal distribution of the transpiration coefficient dictates when transpiration begins and when it ends whereas the transpiration coefficient is the ratio of actual transpiration to potential transpiration. Based on the generalized phenologies described above, the growth cycle is assumed to begin at the end of dormancy or in the case of annuals, with germination, at which point K_c is assigned the initial value. Development starts with the onset of leaf growth, and K_c increases linearly from the initial value to the mid-season value. For STOMP input, the mid-season value of K_c is assumed to occur when flower stalks appear in annuals and when twig growth starts in perennials. The late season stage of development is assumed to start when flowers bloom, after which K_c declines linearly to the initial value.

A transpiration coefficient conversion table is shown in Table 5.24. No data on transpiration coefficients were available for the species of interest at the Hanford Site. The concept of the transpiration coefficient, as designed for crop plants, is based on the assumption that plants are growing under conditions of non-limiting soil water and nutrients and full canopies. This is typically not the case with plants in arid and semi-arid environments, and some adjustment is needed for the typical K_c values. Generally, in the horticultural literature, native plants from arid zones are assigned a K_c of 0.25 to 0.35; evergreen shrubs range from 0.25 to 0.50; whereas grasses range from 0.40 to 0.60. Since water will be limiting

Table 5.24. Estimated Transpiration Coefficients for Different Plant-Growth Forms

Growth Form	Initial K_c	Mid-Season K_c	Late-Season K_c
Annual Forb	0.25	0.85	0.25
Annual Grass	0.25	0.85	0.25
Perennial Forb	0.25	0.85	0.40
Perennial Grass	0.25	0.85	0.40
Shrubs	0.25	0.85	0.35

under typical site conditions, these ranges are used to define the transpiration coefficient in the initial and late developmental stages. Wight and Hanks (1981) determined actual transpiration from lysimeters planted with native vegetation growing under non-limiting soil water conditions and reported K_c ranging from 0.7 in the spring to 0.9 during mid-season. Thus, the growing season K_c average of 0.85 used in their calculations is adopted here for the mid-development stage.

In addition to the underlying assumption of non-limiting soil water and nutrients for the transpiration coefficient in crop plants, it is also assumed that plants are growing under conditions of full canopies. This is typically not the case, and failure to correct for these difference can lead to an over estimation of transpiration. For example, Wight et al. (1986) found that the K_c method estimated evapotranspiration values that represented from 25% to 52% of those obtained in lysimeters in years when the available water for soil water was lowest and 75% of those of lysimeters in wet years. The K_c method typically overestimates water use when plants encounter suboptimal conditions of soil water because it does not consider stomatal regulation and plant adaptations to drought (Mata-González et al. 2005). Further controls on water lost are needed, and in STOMP, these are applied through stomatal regulation.

5.8 Bulk Stomatal Resistance

Transpiration by shrub-steppe species is not well understood, and the few existing data are difficult to extrapolate spatially and temporally. This is partly due to the difficulty in applying the transpiration coefficient method to determining evapotranspiration of vegetation adapted to arid conditions (Mata-González et al. 2005). The transpiration coefficient approach also assumes that plants have a high leaf-area index and little stomatal resistance to water loss, an invalid assumption for the species and conditions of interest. Required input parameters for the stomatal conductance model (Eq. 2.40 and Eq. 2.42) are summarized in Table 5.25.

Table 5.25. Stomatal Conductance Parameters for Different Plant Growth Forms.

Growth Form	Minimum Stomatal Resistance ($s\ m^{-1}$)	Light Response Coefficient ($W\ m^{-2}$)	Optimal Temperature ^oC	Maximum Temperature ^oC	Minimum Temperature ^oC
Annual Forb	50	20	25	45	5
Annual Grass	50	20	25	45	5
Perennial Forb	100	20	25	45	5
Perennial Grass	50	20	25	45	5
Shrubs	200	55	25	45	5

These are all species-dependent, and no data have been identified for the Hanford site. These parameters represent best estimates and are derived from databases developed in the air pollution and meteorology literature. Therefore, even with a well developed canopy, water loss can be controlled as these parameters allow the model to simulate stomatal regulation.

5.9 Plant Albedo

Absorbed solar energy provides most of the energy for evapotranspiration, convection, and soil heating. The amount absorbed is dependent upon the percentage reflected, or albedo. Albedo is a function of solar angle and the physical structure and spectral properties of the reflecting surface. Seasonal trends in the albedo of visible light reported by Baldocchi et al. (2004) are illustrated in Figure 5.5 for a grassland and woodland.

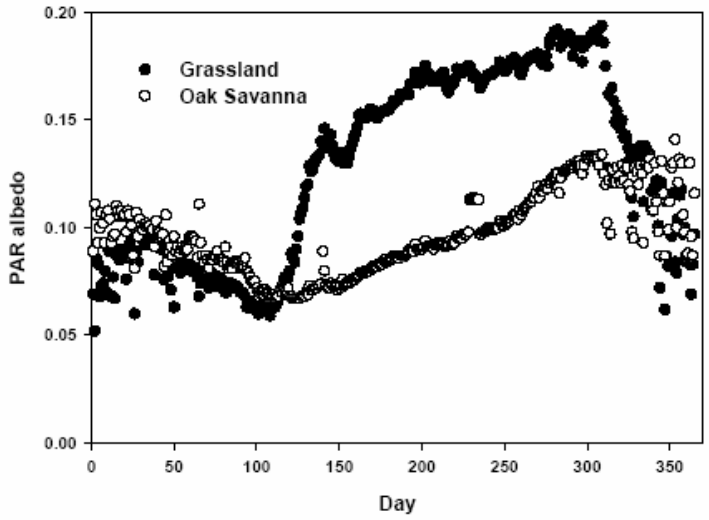

Figure 5.5. Seasonal Variation in Daily Averaged Albedo of Photosynthetically Active Radiation (after Baldocchi et al. 2004)

Starting in January, the albedo decreased as the grass canopy greened up to obscure litter and bare soil. The albedo of the woodland was slightly higher than that of open grassland as the leafless trees were more reflective. The trend changed sharply around day 100, which coincided with the period of minimum albedo for both the woodland and grassland. This switch was attributed to the onset of flowering in the grasses and subsequent senescence (Baldocchi et al. 2004). The golden color of the dried grass during the summer months led to increased albedo and greater reflection of radiation. In the woodland, the change in the trend at day 100 coincided with the onset of leaf expansion. During the summer months, the albedo was lower than that in the grassland because the multi-layered canopy was very effective at trapping sunlight even with a highly reflective grass understory.

STOMP input includes plant albedo at the start of the simulation, α_1; the minimum albedo that typically occurs between the initial and developmental stages (≅ day 100 in Figure 5.5), α_2; the albedo at the end of the developmental stage, or the start of the mid-season (≅ day 150 in Figure 5.5), α_3; the albedo at the start of the late-season stage, α_4 (≅ day 300 in Figure 5.5); and the albedo at the end of the late-season stage (≅ day 365 in Figure 5.5). A similar temporal trend is assumed for sagebrush-dominated rangelands

with absolute values of albedo being derived from the literature (e.g., Dirmhirn and Belt, 1971; Hanson 2001).

Data were available, mostly for sagebrush sites in Idaho and Montana. Using data from three sites, Dirmhirn and Belt (1971) found that the average albedo during midday under clear skies was 0.14 during the growing season. The albedo varied from a low of 0.11 during June at the Mountain big sagebrush site to a high of 0.17 at the low-elevation big sagebrush site. During the day, the albedo varied little between about 2 hr after sunrise and 2 hr before sunset. Albedo values were 0.13 from a low-sagebrush site, 0.134 from a big sagebrush site, and 0.18 from a big-sagebrush–cheatgrass site. Measurements of vegetation distribution also correlated well with albedo differences. The unexpected uniformity in albedo on these sites suggested that although the albedo of the sites varied with time of day (solar angle), soil type, and vegetation type, the site differences between each component were relatively small. The uniformity of values suggests that the range of albedo values should be applicable to a wide range of cold desert sites. Hanson (2001) reported average values over the period 1988 to 1993 of 0.15 in April, 0.13 in May and June, 0.14 in July and August, and 0.13 in September. Hanson also reported that the albedo increased 7 to 14% during the spring and summer followed by a slight decrease in the fall. The albedo measured by Aase and Idso (1975) on mixed prairie in northeastern Montana was about 0.28 higher than those reported by Hanson (2001). Nonetheless, the average values were very close to those reported by Dirmhirn and Belt (1971). Owing to the similarity in albedo reported for sagebrush-rangeland associations and those reported by Baldocchi et al. (2004) for the same measurement times, the high-resolution temporal data of Baldocchi et al. (2004) were used to estimate the values for the specific times. Estimated values of albedo for the different developmental stages are summarized in Table 5.26.

Table 5.26. Variation in Albedo of Different Plant Forms for the Duration of the Growth Cycle

Growth Form	α_1	α_2	α_3	α_4
Annual Forb	0.0625	0.1466	0.1890	0.0802
Annual Grass	0.0625	0.1466	0.1890	0.0802
Perennial Forb	0.0656	0.0727	0.1337	0.0857
Perennial Grass	0.0625	0.1466	0.1890	0.0802
Shrubs	0.0656	0.0727	0.1337	0.0857

The times at which these values are applicable are determined by the generalized phenology of the different growth forms discussed in Section 5.6.

5.10 Summary

Plants play an important role in the function of engineered barriers, and accounting for the effects of plants on barrier performance requires a variety of input parameters. The preceding sections provide a summary of the required input parameters identified in Section 2. Because of the need for species diversity on engineered covers, the number of species that may be used in revegetation and that ultimately coexist on an engineered barrier may be quite large. The STOMP model allows for simulations with multiple plant species, all of which can be expected to have different physiological and phenological characteristics. However, it is beyond the scope of this report to document these characteristics for every possible species. The preceding section provides a summary of the required parameters on the basis of plant growth forms, e.g., forbs, grasses, and shrubs, and provides parameters for each growth form based

on duration (i.e., annuals versus perennials). For each growth form, a representative species from the Hanford Site that is expected to grow on barrier surfaces is used to generate best-estimate parameters. The range of input parameters provided should be adequate to permit an evaluation of the effects canopy structure and color, rooting depth, and growth cycle on energy and water balance and ultimately barrier performance.

6.0 References

Aase JK, and SB Isdo. 1975. "Solar radiation interactions with mixed prairie rangeland in natural and denuded conditions." *Archives for Meteorology, Geophysics, and Bioclimatology*, Series B, 23:255-264.

Ackerman TL, EM Romney, A Wallace, JE Kinnear. 1980. "Phenology of desert shrubs in southern Nye County, Nevada." In *The Great Basin Naturalist Memoirs No. 4. Nevada desert ecology*. Brigham Young University, Provo, Utah, 4-23.

Arya LM and JF Paris. 1981. "A Physicoempirical Model to Predict the Soil Moisture Characteristic from Particle-Size Distribution and Bulk Density Data." *Soil Sci. Soc. Am. J.*, 45:1023-1030.

ASTM D422-63. 2006. *Standard Test Method for Particle-Size Analysis of Soils*. American Society of Testing and Materials, Philadelphia, Pennsylvania.

ASTM D698-00. 2006. *Laboratory Compaction Characteristics of Soil Using Standard Effort*. American Society of Testing and Materials, Philadelphia, Pennsylvania.

ASTM D2325-68. 2006. *Standard Test Method for Capillary-Moisture Relationships for Coarse- and Medium-Textured Soils by Porous-Plate Apparatus*. American Society of Testing and Materials, Philadelphia, Pennsylvania.

ASTM D2434-68. 2006. *Standard Test Method for Permeability of Granular Soils (Constant Head)*. American Society of Testing and Materials, Philadelphia, Pennsylvania.

ASTM D2434-68. 2006. *Standard Test Method for Permeability of Granular Soils (Constant Head)*. American Society of Testing and Materials, Philadelphia, Pennsylvania.

ASTM D2487-00. 2006. *Standard Practice for Classification of Soils for Engineering Purposes (Unified Soil Classification System)*. American Society of Testing and Materials, Philadelphia, Pennsylvania.

ASTM D6836-02. 2006. *Standard Test Methods for Determination of the Soil Water Characteristic Curve for Desorption Using a Hanging Column, Pressure Extractor, Chilled Mirror Hygrometer, and/or Centrifuge*. American Society of Testing and Materials, Philadelphia, Pennsylvania.

Aston AR. 1979. "Rainfall interception by eight small trees." *J. Hydrol.* 42:383–396.

Baldocchi DD, L Xu and N Kiang. 2004. "How plant functional-type, weather, seasonal drought, and soil physical properties alter water and energy fluxes of an oak–grass savanna and an annual grassland." *Agric. and Forest Meteor*. 123(1-2):13-39.

Barbour MG. 1977. *Terrestrial Vegetation of California*. 1002 pp., Wiley Intersci., New York.

Battye W and R Barrows. 2004. *Review of Ammonia Emission Modeling Techniques for Natural Landscapes and Fertilized Soils*. EC/R Project No. PRD-209, EC/R Incorporated, Chapel Hill, North Carolina.

Blaisdell JP. 1958. *Seasonal Development and Yield of Native Plants on the Upper Snake River Plains and Their Relation to Certain Climatic Factors*. Tech. Bull. 1190, U.S. Department of Agriculture, Washington, D.C. 68 p.

Blake GR and KH Hartge. 1986a. "Bulk Density." In *Methods of Soil Analysis, Part 1, Physical and Mineralogical Methods*. A. Klute (ed.), pp. 363-375, American Society of Agronomy, Madison, Wisconsin.

Blake GR and KH Hartge. 1986b. "Particle Density." In *Methods of Soil Analysis, Part 1, Physical and Mineralogical Methods*. A. Klute (ed.), pp. 377-382, American Society of Agronomy, Madison, Wisconsin.

Bouwer H and RC Rice. 1983. "Effect of stones on hydraulic properties of vadose zones." In *Proceedings of the Characterization and Monitoring of the Vadose (unsaturated) Zone*, National Water Well Association, Worthington, Ohio.

Bowers SA and RJ Hanks. 1965. "Reflection of radiant energy from soil." *Soil Sci.* 2:130–138.

Briegleb BP, P Minnis, V Ramanathan, and E Harrison. 1986. "Comparison of regional clear sky albedos inferred from satellite observations and model calculations." *J. Clim. Appl. Meteorol*. 25:214–226.

Brooks RH and AT Corey. 1964. *Hydraulic Properties of Porous Media*. Hydrol. Paper 3. Colorado State University, Fort Collins, Colorado.

Buckman HO and NC Brady. 1969. *The Nature and Properties of Soils*. MacMillan, 653 pp.

Calder IR. 1977. "The model of transpiration and interception loss from a spruce forest in Plynlimon, central Wales." *J. Hydrol.* 33:247–265.

Caldwell LL. 1979. "Physiology of Sagebrush." In: *The Sagebrush Ecosystem: A Symposium*, April 1978. College of Natural Resources, Utah State University, Logan, Utah.

Caldwell MM, CB Osmond, and DL Nott. 1977. "Pathway photosynthesis at low-temperature in cold-tolerant atriplex species." *Plant Physiology* 60 (1):157-164.

Cass A, GS Campbell, TL Jones. 1981. *Hydraulic and Thermal Properties of Soil Samples from the Buried Waste Test Facility*. PNL-4015, Pacific Northwest National Laboratory, Richland, Washington.

Cass A, GS Campbell, and TL Jones. 1984. "Enhancement of thermal water vapor diffusion in soil." *Soil Sci. Soc. Am. J.*, 48:25–32.

Chow VT. 1964. *Handbook of Applied Hydrology*. McGraw-Hill Book Company, New York.

Danielson RE and PL Sutherland. 1986. "Porosity." In *Methods of Soil Analysis, Part 1, Physical and Mineralogical Methods*. A. Klute (ed.), pp. 443-461, American Society of Agronomy, Madison, Wisconsin.

Daubenmire R. 1972. "Annual cycles of soil moisture and temperature as related to grass development in the steppe of eastern Washington." *Ecology* 53(3):419-424.

DePuit EJ and MM Caldwell. 1973. "Seasonal pattern of new photosynthesis of *Artemisia tridentata*." *Am. J. Bot*. 60(5):426-435.

Depuit EJ and MM Caldwell. 1975. "Gas exchange of three cool semi-desert species in relation to temperature and water stress." *J. Ecol*. 63:835–858.

Dickinson RE, A Henderson-Sellers, and PJ Kennedy. 1993. *Biosphere-Atmosphere Transfer Scheme (BATS) Version 1E as Coupled to the NCAR Community Climate Model*. National Center for Atmospheric Research Technical Note (NCAR TN-387+STR), Boulder, Colorado.

Dirmhirn I and GH Belt. 1971. "Variation of albedo of selected sagebrush range in the intermountain region." *Agr. Meteorol*. 951-961.

Downs JL and FO Khan. 1999. "Vegetation Data Summary for Supporting Recharge Estimates – FY 1998 and FY 1999." In Appendix F, *Recharge Data Package for the Immobilized Low-Activity Waste 2001 Performance Assessment*. MJ Fayer, FO Khan, EM Murphy CW Lindenmeier, JL Downs, and BN Bjornstad, (eds.), PNNL-13033, Pacific Northwest National Laboratory, Richland, Washington.

Downs JL, LL Cadwell, and SO Link. 1993. "Root Intrusion, Root Distribution Studies." In *Hanford Site Protective Barrier Development Program: Fiscal Year 1993 Highlights*. LL Cadwell, SO Link, and GW Gee (eds.), PNL-8471, pp. 2.7-2.29, Pacific Northwest National Laboratory, Richland, Washington.

Everett, RL, PT Tueller, JB Davis, and AD Brunner. 1980. "Plant phenology in Galleta-Shadscale and Galleta-Sagebrush Associations." *J. Range Manage*. 33(6):446-450.

Farouki O. 1981. *Thermal Properties of Soils*. CRREL Monograph 81-1, U.S. Army Corps of Engineers, Hanover, New Hampshire.

Feddes RA and PAC Raats. 2004. *Parameterizing the soil–water–plant root system*. In: R.A. Feddes, G.H. de Rooij and J.C. van Dam, Editors, Unsaturated-zone Modeling: Progress, Challenges, Applications vol. 6, Wageningen UR Frontis Series (2004), pp. 95–141 (xxii+p. 364, Chapter 4 in http://library.wur.nl/frontis/unsaturated/toc_unsaturated.html).

Feddes RA, P Kowalik, and H Zarandy. 1978. *Simulation of Field Water Use and Crop Yield*. Pudoc. Wageningen, The Netherlands.

Fire Effects Information Service (FEIS). 2007. *Fire Effects Information*. U.S. Department of Agriculture Forest Service. Available at: http://www.fs.fed.us/database/feis/plants/index.html/. Accessed October 2007.

Folk RL. 1980. "Petrology of Sedimentary Rocks." Hemphill Publishing Company, Austin, Texas.

Franklin JF and CT Dyrness. 1988. *Natural Vegetation of Oregon and Washington*. Oregon State University Press, Corvallis, Oregon, 452 pp.

Fredlund MD. 1999. *Estimation of Soil Properties for Thermal Modeling*. SoilVision Systems Ltd., Saskatoon, Saskatchewan, Canada.

Gee GW and JW Bauder. 1986. "Particle-Size Analysis." In *Methods of Soil Analysis, Part 1*, A Klute (ed.), pp. 383-409. American Society of Agronomy, Madison, Wisconsin.

Goudriann J. 1988. "The bare bones of leaf-angle distribution in radiation models for canopy photosynthesis and energy exchange." *Agricultural and Forest Meteorology* 43:155-169.

Graser EA and CHM van Bavel. 1982. "The effect of soil moisture upon soil albedo." *Agric. Meteorol* 27:17-26.

Gurr CG, TJ Marshall, and JT Hutton. 1952. "Movement of water in soil due to a temperature gradient." *Soil Sci.* 74:335-345.

Hanson CL. 2001. "Clear-sky albedo measured at seven rangeland sites in southwest Idaho." *J. Hydrologic Eng.* 6(6): 532-534.

Hansen J, G Russell, D Rind, P Stone, A Lacis, S Lebedeff, R Reudy, and L Travis. 1983. "Efficient three-dimensional global models for climate studies: Models I and II." *Mon. Weather. Rev*. 111, 609-662.

Hicks BB, DD Baldocchi, TP Meyers, RP Hosker Jr., and DR Matt. 1987. "A preliminary multiple resistance routine for deriving dry deposition velocities from measured quantities." *Water, Air, Soil Pollut.* 36:311–330.

Hull AC Jr. 1972. "Rainfall and snowfall interception of big sagebrush." *Utah Acad. Sci. Arts and Letters*. 49:64.

Hull AC Jr. and GI Klomp. 1974. "Yield of crested wheatgrass under four densities of big sagebrush in southern Idaho." *U.S. Dep. Agr. Tech. Bull. 1483*, 38 p.

Idso SB, RD Jackson, RJ Reginato, BA Kimball, and FS Nakayama. 1975. "The dependence of bare soil albedo on soil water content." *J. Appl. Meteorol*., 14:109–113.

International Biological Program. 1974. "Reports of 1973 Progress." Vol. 2, *Validation Studies*, 332 pp., Utah State University, Logan, Utah.

Iryo T and K Rowe. 2003. "On the hydraulic behavior of unsaturated nonwoven geotextiles." *Geotextiles and Geomembranes* 21:381-404.

Jarvis P. 1976. "The interpretation of leaf water potential and stomatal conductance found in canopies in the field." *Philos. Trans. Roy. Soc. London,* 273B:593-610.

Johansen O. 1975. *Thermal Conductivity of Soils*. Ph.D. Thesis (CRREL Draft Translation 637, 1977), Trondheim, Norway.

Jury WA, WR Gardner, and WH Gardner. 1991. *Soil Physics*. John Wiley and Sons, New York.

Khaleel R and EJ Freeman. 1995. *Variability and Scaling of Hydraulic Properties for 200 Area Soils, Hanford Site*. WHC-EP-0883, Westinghouse Hanford Company, Richland, Washington.

Klepper B, LE Rogers, JD Hedlund, RG Schreckhise, and KR Price. 1978. "Radiocesium Movement in a Gray Rabbit Brush Community." In *Environmental Chemistry and Cycling Processes, Proceedings of Mineral Cycling Symp*, DC Adriano and IL Brisbin (eds.), pp. 725-737.

Klepper EL, KA Gano, and LL Cadwell. 1985. *Rooting Depth and Distributions of Deep Rooted Plants in the 200 Area Control Zone of the Hanford Site*. PNL-5247, Pacific Northwest National Laboratory, Richland, Washington.

Klute A. 1986. "Water Retention: Laboratory Methods." In *Methods of Soil Analysis, Part 1*, AL Page, RH Miller, DR Keeney (eds.), American Society of Agronomy-Soil Science of America, Madison, Wisconsin, pp. 635-662.

Kremer RG, ER Hunt, SW Running, and JC Coughlan. 1996. "Simulating vegetational and hydrologic responses to natural climatic variation and GCM-predicted climate change in a semi-arid ecosystem in Washington, USA." *J. Arid Environ*. 33(1):23-38.

Link, SO, GW Gee, and JL Downs. 1990. "The effect of water stress on phenological and ecophysiological characteristics of cheatgrass and Sandberg's bluegrass." *J. Range Manage*. 43(6):506-513.

Link SO, WJ Waugh, JL Downs, ME Thiede, JC Chatters, and GW Gee. 1994. "Effects of coppice dune topography and vegetation on soil water dynamics in a cold-desert ecosystem." *J. Arid Environments* 27:265-278.

Link SO, LL Cadwell, KL Petersen, MR Sackschewsky, and DS Landeen. 1995. *The Role of Plants and Animals in Isolation Barriers at Hanford, Washington*. PNL-10788, Pacific Northwest National Laboratory, Richland, Washington.

Lobell DB and GP Asner. 2002. "Moisture effects on soil reflectance." *Soil Sci. Soc. Am. J.* 66:722–727.

Ludwig JA, JF Reynolds, and PD Whitson. 1975. "Size-biomass relations of several Chihuahuan Desert shrubs." *Am. Midland Nat*. 94:451–461.

MacMahon JA and DJ Schimpf. 1981. "Water as a Factor in the Biology of North American Desert Plants." In *Water in Desert Ecosystems*, DD Evans and JL Thames (eds.), pp. 114–171, Dowden, Hutchinson & Ross, Inc., Stroudsburg, Pennsylvania.

Massman WJ. 1980. "Water storage on forest foliage: A general model." *Water Resour. Res.* 16:210–216.

Mata-González R, T McLendon, and D Martin. 2005. "The inappropriate use of crop transpiration coefficients (K_c) to estimate evapotranspiration in arid ecosystems: A review." *Arid Land Res. and Manage.* 19:285-295.

Mbonimpa M, M Aubertin, RP Chapuis, and B Bussiere. 2002. "Practical pedotransfer functions for estimating the saturated hydraulic conductivity." *Geotechnical and Geological Engineering* 20:235-259.

Meyer PD and RJ Serne. 1999. *Near-Field Hydrology Data Package for the Immobilized Low-Activity Waste 2001 Performance Assessment*. PNNL-13035, Pacific Northwest National Laboratory, Richland, Washington.

Monteith JL. 1998. "Evaporation Models." In *Agricultural Systems and Modeling and Simulation*, RM Peart and RB Curry (eds.), p. 197–234, Marcel Dekker, New York.

Mualem Y. 1976. "A new model for predicting the hydraulic conductivity of unsaturated porous media." *Water Resour. Res.* 12:513–522.

Murray CJ, AL Ward, and JL Wilson, III. 2003. Influence of Clastic Dikes on Vertical Migration of Contaminants in the Vadose Zone at Hanford. PNNL-14224, Pacific Northwest National Laboratory, Richland, WA.

Norero AL. 1969. *A Formula to Express Evapotranspiration as a Function of Soil Moisture and Evaporative Demands of the Atmosphere*. Ph.D. Dissertation, Utah State University, Logan, Utah, and University Microfilms, Inc., Ann Arbor, Michigan.

Ochsner TE, R Horton, and T Ren. 2001. "A new perspective on soil thermal properties." *Soil Sci. Soc. Am. J.* 65:1641-1647.

Oguntunde PG, AE Ayodele, N van de Giesen. 2006. "Tillage and surface moisture effects on bare-soil albedo of a tropical loamy sand." *Soil Till. Res.* 85(1-2):107-114.

Pearson LC. 1979. "Effects of temperature and moisture on phenology and productivity of Indian ricegrass." *Journal of Range Management* 32(2):127-133.

Perryman, BL and RA Olson. 2000. "Age-stem diameter relationships of big sagebrush and their management implications." *J. Range Manage.* 53:342–346.

Petersen SW. 2003. *Sampling and Analysis Plan for the Characterization of Fine-Grained Sediments at Area C*. WMP-18320, Rev. 0. Fluor Hanford, Inc., Richland, Washington.

Peters-Lidard, CD, E Blackburn, X Liang, and E F Wood. 1998. "The effect of soil thermal conductivity parameterization on surface energy fluxes and temperatures." *J. Atmos. Sci*. 55(7):1209-1224.

Philip JR and DA de Vries. 1957. "Moisture movement in porous materials under temperature gradients." *Transactions, American Geophysical Union* 38:222-232.

Pleim JE and A Xiu. 1995. "Development and testing of a surface flux and planetary boundary layer model for application in mesoscale models." *J. App. Meteorol*. 34:16-32.

Post, DF, A Fimbres, AD Matthias, EE Sano, L Accioly, AK Batchily and LG Ferreira. 2000. "Predicting soil albedo from soil color and spectral reflectance data." *Soil Sci. Soc. Am. J.* 64:1027-1034.

Raats PAC, ZF Zhang, AL Ward, and GW Gee. 2004. "The relative connectivity-tortuosity tensor for conduction of water in anisotropic unsaturated soils." *Vadose Zone J.* 3(4):1471-1478.

Ramirez JA and S Senarath. 2000. "A statistical–dynamical parameterization of interception and land surface–atmosphere interactions." *J. Climate* 13:4050-4063.

Rawls WJ, LR Ahuja, and DL Brakensiek. 1992. "Estimating Soil Hydraulic Properties from Soils Data." In *Proc. Indirect Methods for Estimating the Hydraulic Properties of Unsaturated Soils*, MT van Genuchten, FJ Leij, and LJ Lund (eds.), Riverside, California.

Rockhold ML, MJ Fayer, and PR Heller. 1993. *Physical and Hydraulic Properties of Sediments and Engineered Materials Associated with Grouted Double-Shell Tank Waste Disposal at Hanford*. PNL-8813, Pacific Northwest Laboratory, Richland, Washington.

Schaap MG, FJ Leij, and MT van Genuchten. 1997. "A Bootstrap-Neural Network Approach to Predict Soil Hydraulic Parameters." In: *Proc. Characterization and Measurement of the Hydraulic Properties of Unsaturated Porous Media*. MT van Genuchten, FJ Leij, and L Wu (eds.), Riverside, California.

Schaap MG and FJ Leij. 1998. "Database-related accuracy and uncertainty of pedotransfer functions." *Soil Sci*. 163:765–779.

Schenk HJ and RB Jackson. 2002. "Rooting depths, lateral root spreads and below-ground/above-ground allometries of plants in water-limited ecosystems." *Journal of Ecology*, 90: 480–49.

Schuh WM and RL Cline. 1990. Effect of soil properties on unsaturated hydraulic conductivity pore-interaction factors." *Soil Sci. Soc. Am. J*. 54:1509–1519.

Shannon and Wilson Inc. 1994. "Geotechnical Investigation KEH W-236A Multi Function Waste Tank Facility, Hanford Site, Richland Washington." H-1070-50, Shannon and Wilson Inc., Kennewick, Washington.

SoilVision. 2001. *SoilVision User's Guide*, Version 3.0. SoilVision Systems Ltd, Saskatoon, Saskathewan, Canada, 185 pp.

Steinwand AL, RF Harrington, and DP Groeneveld. 2001. "Transpiration coefficients for three Great Basin shrubs." *J. Arid Environ*., 49:555–567 doi:10.1006/jare.2001.0794.

Stormont JC, KS Henry, and TM Evans. 1997. "Water retention functions of four nonwoven polypropylene geotextiles." *Geosynthetics International* 4(6):661-672.

Szeicz G, G Endrodi, and S Tajchman. 1969. "Aerodynamic and surface factors in evaporation." *Water Resour. Res.* 5:380-394.

Taylor SA and GL Ashcroft. 1972. *Physical Edaphology, The Physics of Irrigated and Nonirrigated Soils*. WH Freeman and Company, San Francisco, California.

Taylor SA and L Cavazza. 1954. "The movement of soil moisture in response to temperature gradients." *Soil Sci. Soc. Am. Proc*. 18:351-358.

van Asch T. 2001. "FORGAP: A Model for Solar Radiation, Evapotranspiration and Soil Water Dynamics in Tropical Rain Forest Gaps." In *Forest Filled with Gaps. Effects of Gap Size on Water and Nutrient Cycling in Tropical Rain Forest. A Study in Guyana*, O van Dam (ed.), Tropenbos-Guyana Series 10 Tropenbos-Guyana Programme, Georgetown, Guyana. ISBN 90-5113-046-5.

van Genuchten M Th. 1987. *A Numerical Model for Water and Solute Movement in and Below the Root Zone*. Unpublished Research Report, United States Department of Agriculture, Agricultural Research Service, U.S. Salinity Laboratory, Riverside, California.

van Genuchten M Th. 1980. "A closed-form equation for predicting the hydraulic conductivity of unsaturated soils." *Soil Sci. Soc. Am. J.* 44:892-898.

Vrugt JA, MT van Wijk, JW Hopmans, and J Simunek. 2001. "One-, two-, and three-dimensional root water uptake functions for transient modeling." *Water Resources Research* 37(10):2457-2470.

Wang Z, M Barlage, X Zeng, RE Dickinson, and CB Schaaf. 2005. :The solar zenith angle dependence of desert albedo." *Geophys. Res. Lett.* 32(5): Art. No. L05403 MAR 8 2005.

Ward AL and GW Gee. 1997. ''Performance evaluation of a field-scale surface barrier.'' *J. Envir. Quality* 26:694-705.

Ward AL, GW Gee, and SO Link. 1997. *Hanford Prototype Barrier Status Report: FY 1997*, PNNL 11789, Pacific Northwest National Laboratory, Richland, Washington.

Ward AL, JM Keller, and KS Waters-Husted. 2005a. *Hydrology and Vegetation Data Package for 200-UW-1 Waste Site Engineered Surface Barrier Design*. PNNL-15464, Pacific Northwest National Laboratory, Richland, Washington.

Ward AL, JK Linville, and CD Wittreich. 2005b. *200-BP-1 Prototype Hanford Barrier Annual Monitoring Report for Fiscal Year 2003*. CP-18187, Fluor Hanford, Inc., Richland, Washington

Ward AL, JK Linville, JM Keller, and GH Seedahmed. 2005c. *200-BP-1 Prototype Hanford Barrier Annual Monitoring Report for Fiscal Year 2004*. PNNL-14960, Pacific Northwest National Laboratory, Richland, Washington.

Ward AL, MD White, EJ Freeman, and ZF Zhang. 2005d. *STOMP Subsurface Transport Over Multiple Phases Version 1.0 Addendum: Sparse Vegetation Evapotranspiration Model for the Water-Air-Energy Operational Mode*. PNNL-15465, Pacific Northwest National Laboratory, Richland, Washington.

Ward AL, ZF Zhang, and GW Gee. 2006. "Upscaling unsaturated hydraulic parameters for flow through heterogeneous anisotropic sediments." *Adv. in Water Resour*. 29:268-280.

Ward AL, SO Link, CE Strickland, KE Draper, and RE Clayton. 2007. *200-BP-1 Prototype Hanford Barrier Annual Monitoring Report for Fiscal Year 2007*. PNNL-xxxxx, Pacific Northwest National Laboratory, Richland, Washington (*In Press*).

Washington State Department of Transportation (WDOT). 2006. *Standard Specifications for Road, Bridge, and Municipal Construction- M41-10.*
http://www.wsdot.wa.gov/publications/manuals/fulltext/M41-10/SS2004.pdf

Wells LP and GJ Blake. 1972. "Interception characteristics of some central North Island vegetation and their geographical significance." *Proc. Seventh New Zealand Geogr. Conf.*, July 3-7, Hamilton, New Zealand, p. 217–224.

Werk KS, J Ehleringer, IN Forseth, and CS Cook. 1983. "Photosynthetic characteristics of Sonoran Desert winter annuals." *Oecologia* 59:101–105.

West NE and GF Gifford. 1976. "Rainfall interception by cool-desert shrubs." *J. Range Manag*. 29:171–172.

White MD and AL Ward. 2005. "Numerical simulation of surface barriers for shrub-steppe ecoregions." *Hydrology Days* 25:224-236.

Wight JR and RJ Hanks. 1981. "A water-balance, climate model for range forage production." *J. Range Mangement*, 34:307-311

Wight JR, CL Hanson, and KR Cooley. 1986. "Modeling evapotranspiration from sagebrush-grass rangeland." *J. Range Management*, 39: 81–85.

Wilcox BP, DD Breshears, MS Seyfried. 2003. "Water balance on rangelands." *Encyclopedia of Water Science* 791-794.

Williamson SC, JK Detling, JL Dood, and MI Dyer. 1987. "Nondestructive estimation of shortgrass aerial biomass." *J. Range Manage*. 40:254–256.

Yan SG, CG Wan, RE Sosebee, DB Wester, EB Fish, and RE Zartman. 2000. "Responses of photosynthesis and water relations to rainfall in the desert shrub creosote bush (*Larrea tridentata*) as influenced by municipal biosolids. *J. Arid Environ*., 46: 397–412.

Yates SR, M Th van Genuchten, AW Warrick, and FJ Leij. 1992. "Analysis of measured, predicted, and estimated hydraulic conductivity using the RETC computer program." *Soil Sci. Soc. Am. J*. 56:347–354.

Zhang ZF, AL Ward, and GW Gee. 2003. "A tensorial connectivity-tortuosity concept to describe the unsaturated hydraulic properties of anisotropic soils." *Vadose Zone J.* 2:313–321.

Zhang, ZF, AL Ward, and GW Gee. 2004. A parameter scaling concept for estimating filed-scale hydraulic functions of layered soils. *J. Hydraulic Research* 42:93-103.

Appendix A: ERDF Spoil Pile Sampling on August 5, 2004

Table A1. Sample Locations at the ERDF Spoil Pile

Sample interval (inches BGS)	Location on ERDF Spoil Pile	Soil Type	Other Field Notes of Sample Hole
12 to 24 in. bgs	West sideslope near north end; 15 ft downslope from top of slope	Medium sand with gravel	Moist first 2 to 3 in., dry next 6 to 8 in., moist from 12 in.+
12 to 24 in. bgs	West sideslope near south end; 15 ft upslope from toe of slope	Medium sand with gravel; some small clumps of fine-grained soil	Moist first 2 to 3 in., dry next 6 to 8 in., moist from 12 in.+
12 to 24 in. bgs	South sideslope near west end; 25 ft upslope from toe of slope	Medium sand with gravel	Moist first 2 to 3 in., dry next 6 to 8 in., moist from 15 in.+
12 to 24 in. bgs	South sideslope near slope center; 75 ft upslope from toe of slope and just below top of slope.	Medium sand with gravel	Moist first 2 to 3 in., dry next 6 to 8 in., moist from 12 in.+
12 to 30 in. bgs	South sideslope near east end; 50 ft upslope from toe of slope and below bench	Medium sand with gravel	Moist first 2 to 3 in., dry next 6 to 8 in., moist from 12 in.+
12 to 24 in. bgs	South sideslope near east side above bench mid- upper slope	Medium sand with gravel with black colored sand starting at 12" bgs	Moist first 2 to 3 in., dry next 6 to 8 in., moist from 12 in.+
12 to 24 in. bgs	North sideslope near west end; 40 ft upslope from toe of slope	Medium sand with gravel	Moist first 2 to 3 in., dry next 6 to 8 in., moist from 12 in.+
12 to 24 in. bgs	North sideslope near east end above bench mid-upper slope	Medium sand with gravel	Moist first 2 to 3 in., dry next 6 to 8 in., moist from 12 in.+
12 to 24 in. bgs	North sideslope near east end; 50 ft upslope from toe of slope	Medium sand with gravel	Moist first 2 to 3 in., dry next 6 to 8 in., moist from 12 in.+
12 to 36 in. bgs	East sideslope near center about 2/3 upslope or about 100 feet downslope from top plateau	Medium sand with gravel	Moist throughout. Hard digging. Used shovel from 0 to ~24 in. and then hand auger ~24 in. to 36 in. bgs. Very dense first 18 to 24 in. and then dense below 18 in..

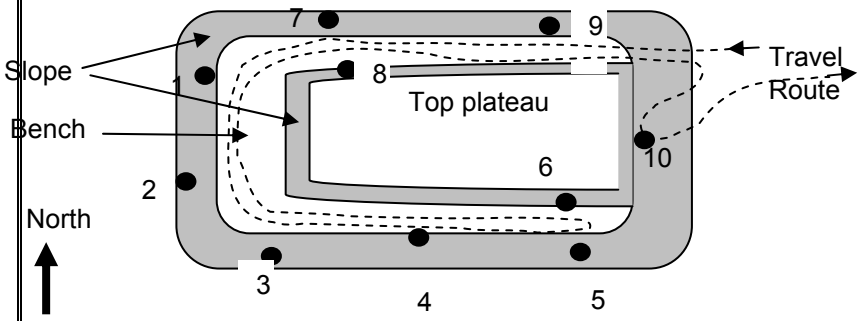

Summary: soil type consistent throughout spoil pile as brown medium sand with some gravel with minor exceptions (fine-grained clumps @ #2 and black sand @ # 6). Gravel portion ranges from pea gravel to 3 in. dia in general. Sideslopes loose to somewhat dense except east slope which was dense to very dense. Rained earlier which result in first 2 to 3 in. of soil being moist. Generally appears dry from 3 to 12 in. bgs, then moist again below 12 in. Bench on N, W and S sides creates stepped sideslopes. Samples by Curt Wittreich and Ray Clayton on 8/5/04 from ~ 10:15am to 12:15 pm. Used hand shovel to collect bulk samples in 5 gal buckets except #1 and # 10 where a hand auger was also used.

Appendix B: Hydraulic and Thermal Properties for Barrier Materials

Table B1. Summary of Particle Size Characteristics for Silt Loam Borrow Site Soils (DBS 2005)

Sample Number	d_{10} (mm)	d_{50} (mm)	d_{60} (mm)	C_u	C_c	Method	ASTM Classification	USDA Classification
B18DD3/B18DD2 Composite	0.0057	0.072	0.092	16	3.2	WS/H	Sandy silt	Sandy Loam
B18DD4/B18DF7 Composite	0.0035	0.051	0.064	18	2.6	WS/H	Sandy silt	Loam
B18DF8	0.0047	0.072	0.088	19	3.7	WS/H	Requires Atterberg test	Sandy Loam
B18DF6	0.019	0.18	0.23	12	2.3	WS/H	Requires Atterberg test	Loamy Sand
B18DF9	0.0024	0.022	0.033	14	1.3	WS/H	Requires Atterberg test	Silt Loam
B18DD5	0.00071	0.015	0.021	30	3.4	WS/H	Silt	Silt Loam
B18DD6	0.0053	0.042	0.051	9.6	2.1	WS/H	Requires Atterberg test	Silt Loam
B18DF2	0.00019	0.019	0.027	142	13	WS/H	Requires Atterberg test	Silt Loam
B18DF4	0.0024	0.041	0.056	23	1.7	WS/H	Requires Atterberg test	Loam
B18DF5	0.0051	0.031	0.048	9.4	1.5	WS/H	Silt with sand	Silt Loam

Table B2. Summary of Initial Moisture Content, Dry Bulk Density, Wet Bulk Density, Particle Density, and Calculated Porosity for the Silt Loam Borrow Site Soils (DBS 2005)

Sample Number	Initial Moisture Content		Dry Bulk Density	Wet Bulk Density	Particle Density	Calculated Porosity
	Gravimetric (%, g/g)	Volumetric (%, cm^3/cm^3)	(g/cm^3)	(g/cm^3)	(g/cm^3)	(%)
B18DD3/B18DD2 Composite	13.3	20.0	1.50	1.70	2.51	40.5
B18DD4/B18DF7 Composite	11.9	18.0	1.51	1.69	2.53	40.4
B18DF8	13.6	20.2	1.49	1.69	2.56	41.7
B18DF6	17.6	25.6	1.45	1.71	2.68	45.9
B18DF9	13.6	20.2	1.49	1.69	2.58	42.2
B18DD5	13.6	20.4	1.49	1.70	2.48	39.7
B18DD6	13.8	20.6	1.49	1.69	2.57	42.2
B18DF2	14.9	22.0	1.48	1.70	2.56	42.3
B18DF4	14.4	21.3	1.48	1.69	2.59	42.9
B18DF5	14.5	21.4	1.48	1.69	2.63	43.9

Table B3. Summary of Atterberg Tests for Silt Loam Borrow Site Sample B18DD5 (DBS 2005)

Sample Number	Liquid Limit	Plastic Limit	Plasticity Index	Classification
B18DD3/B18DD2 Composite	---	---	---	ML
B18DD4/B18DF7 Composite	---	---	---	ML
B18DD5	30	26	4	ML
B18DF5	---	---	---	ML

Table B4. Summary of Proctor Compaction Tests for Composite Silt Loam Borrow Site Samples B18DD3/B18DD2 and B18DD4/B18DF7 (DBS 2005)

Sample Number	Optimum Moisture Content (% g/g)	Maximum Dry Bulk Density (g/cm^3)
B18DD3/B18DD2 Composite	14.5	1.74
B18DD4/B18DF7 Composite	14.8	1.74

Table B5. Summary of Moisture Characteristics of the Initial Drainage Curve For Silt Loam Borrow Site Soils (3 pages) (DBS 2005)

Sample Number	Pressure Head (-cm water)	Moisture Content (%, cm^3/cm^3)
B18DD3/B18DD2 Composite	0	40.9
	20	37.2
	53	34.5
	151	25.9
	510	19.9
	13257	5.6
	851293	2.3
B18DD4/B18DF7 Composite	0	43.6
	26	39.8
	53	38.8
	154	27.5
	510	18.0
	7649	8.5
	851293	1.8
B18DF8	0	45.9
	21	43.3
	51	42.3
	144	26.8
	510	18.9
	18968	5.9
	851293	2.1

Table B5. Summary of Moisture Characteristics of the Initial Drainage Curve For Silt Loam Borrow Site Soils (3 pages) (DBS 2005)

Sample Number	Pressure Head (-cm water)	Moisture Content (%, cm^3/cm^3)
B18DF6	0	31.8
	11	29.5
	40	28.1
	73	24.6
	255	11.2
	14787	4.9
	851293	0.9
B18DF9	0	46.1
	29	44.0
	129	42.1
	510	36.6
	7037	12.5
	17235	9.3
	851293	4.7
B18DD5	0	43.4
	28	43.0
	128	41.4
	510	27.4
	7139	10.1
	14787	7.0
	851293	2.3
B18DD6	0	43.9
	22	41.3
	54	40.2
	154	37.9
	510	22.4
	4589	11.0
	851293	2.5
B18DF2	0	48.1
	24	46.6
	53	45.8
	154	43.9
	510	33.3
	8770	10.2
	851293	2.6

Table B5. Summary of Moisture Characteristics of the Initial Drainage Curve For Silt Loam Borrow Site Soils (3 pages) (DBS 2005)

Sample Number	Pressure Head (-cm water)	Moisture Content (%, cm^3/cm^3)
B18DF4	0	42.4
	25	39.7
	124	36.9
	510	32.0
	7852	9.1
	12442	7.6
	851293	2.4
B18DF5	0	44.7
	19	41.6
	53	39.1
	155	36.4
	510	26.5
	18356	4.8
	851293	2.1

Table B6. van Genuchten Model Parameters for the Silt Loam Borrow Site Soils

Sample ID	Van Genuchten Model Parameters				K_s (cm/s)
	α (cm^{-1})	n ( )	θ_r ($m^3\ m^{-3}$)	θ_s ($m^3\ m^{-3}$)	
B18DD3/B18DD2[(a)]	0.0197	1.3324	0.0027	0.4048	3.964E-05
B18DD4/B18DF7 [(a)]	0.0161	1.4253	0.0173	0.4374	4.812E-05
B18DF8	0.0152	1.5060	0.0259	0.4640	3.916E-05
B18DF6	0.0113	2.0593	0.0281	0.3073	1.123E-03
B18DF9	0.0018	1.6090	0.0415	0.4465	3.028E-06
B18DD5	0.0039	1.5284	0.0214	0.4388	1.796E-06
B18DD6	0.0055	1.5408	0.0259	0.4298	2.547E-05
B18DF2	0.0030	1.5157	0.0178	0.4739	3.903E-05
B18DF4	0.0021	1.5794	0.0171	0.4039	1.019E-05
B18DF5	0.0049	1.4763	0.0074	0.4266	1.588E-05
(a) Composite samples					

Table B7. Best-Estimate Parameter Values for Silt Loam-Pea Gravel Admixture

Sample ID	Van Genuchten Model Parameters				K_s (cm/s)
	α (cm^{-1})	n (-)	θ_r ($m^3\ m^{-3}$)	θ_s ($m^3\ m^{-3}$)	
B18DD3/B18DD2[(a)]	0.0197	1.3324	0.0025	0.3690	3.409E-05
B18DD4/B18DF7 [(a)]	0.0161	1.4255	0.0158	0.3983	4.132E-05
B18DF8	0.0152	1.5061	0.0236	0.4230	3.358E-05
B18DF6	0.0113	2.0603	0.0256	0.2808	9.564E-04
B18DF9	0.0018	1.609	0.0378	0.4072	2.594E-06
B18DD5	0.0039	1.528	0.0195	0.4003	1.547E-06
B18DD6	0.0055	1.5406	0.0236	0.3919	2.182E-05
B18DF2	0.0030	1.5159	0.0162	0.4324	3.347E-05
B18DF4	0.0021	1.5796	0.0156	0.3685	8.727E-06
B18DF5	0.0049	1.4762	0.0067	0.3893	1.356E-05
(a) Composite samples					

Table B8. Particle Densities, Loose Dry Bulk Density, and Initial Water Contents for ERDF Spoil Pile Samples

Sample ID	Particle Density (g/cm3)	Loose Dry Bulk Density (g/cm^3)	Initial Moisture (g/g)
B1B380		1.15	0.0743
B1B381		1.22	0.0989
B1B382	2.70	1.10	0.0701
B1B383		1.26	0.0423
B1B384		1.21	0.0538
B1B385	2.72	1.28	0.0429
B1B386		1.14	0.0502
B1B387		1.22	0.0341
B1B388	2.61	1.09	0.0856
B1B389		1.23	0.0359
Composite	2.68		
Mean	2.68	1.20	0.0571
Std.	0.06	0.07	0.0222

Table B9. Measured water retention for ERDF sample B1B394 at 90 percent maximum dry density (1.55 g cm^{-3})

Method	Matric Potential ψ (cm)	Water Content θ_v
Hanging Water Column	1.0	0.379
	4.9	0.370
	9.8	0.358
	18.5	0.346
	29.3	0.305
	37.2	0.269
	45.0	0.246
	54.2	0.225
	72.4	0.177
	97.7	0.139
	120.4	0.127
Pressure Plate	146.7	0.052
	195.6	0.044
	488.9	0.042
	977.8	0.035
Water Activity Meter	2693313.3	0.009

Table B10. Measured Water Retention for ERDF Sample B1B394 at 95 Percent Maximum Dry Density (1.64 g cm^{-3})

Method	Matric Potential ψ (cm)	Water Content θ_v
Hanging Water Column	1.0	0.407
	4.9	0.395
	9.8	0.386
	18.5	0.374
	29.5	0.345
	36.7	0.315
	45.2	0.285
	54.6	0.261
	77.8	0.199
	98.6	0.166
	102.4	0.160
Pressure Plate	146.7	0.052
	195.6	0.049
	488.9	0.046
	977.8	0.039
Water Activity Meter	2693313.3	0.010

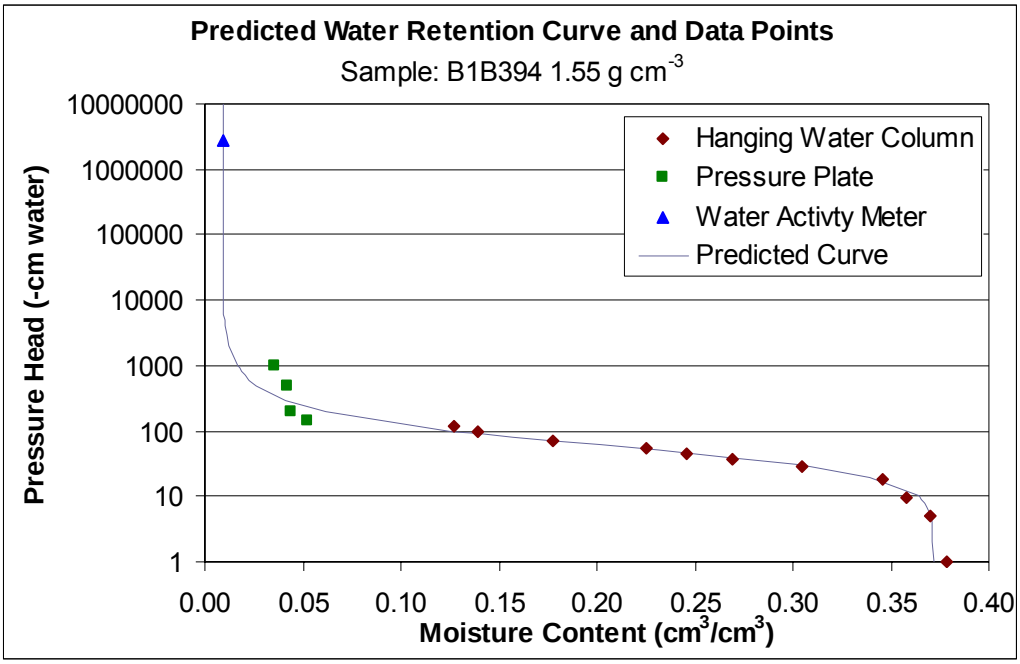

Figure B1. Measured and Fitted Water Retention for ERDF Sample B1B394 at 90 Percent Maximum Dry Density (1.55 g cm^{-3})

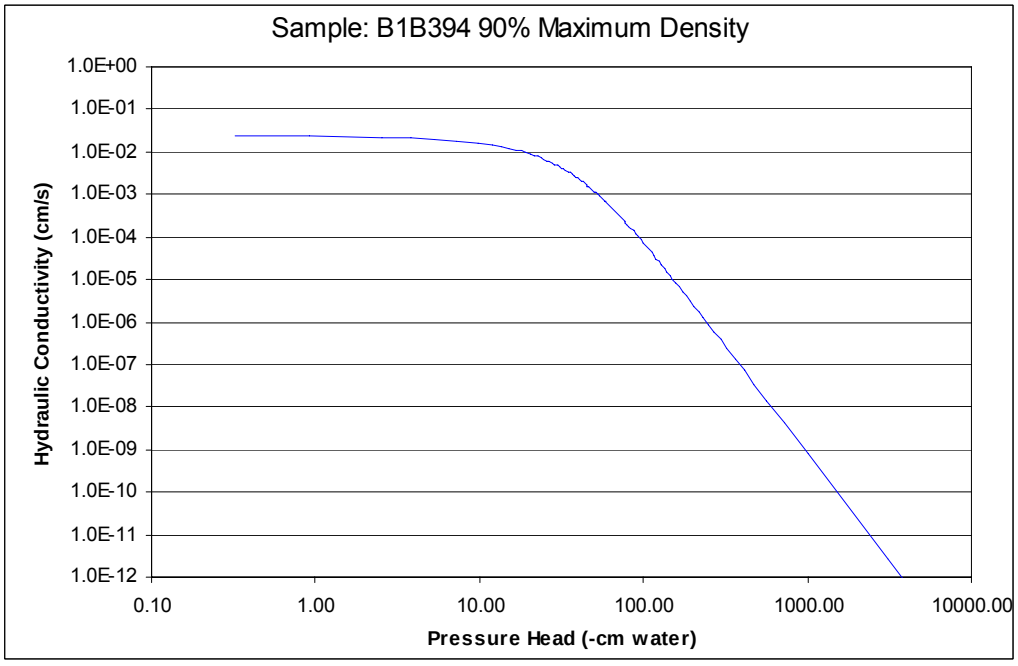

Figure B2. Predicted Hydraulic Conductivity for ERDF Sample B1B394 at 90 Percent Maximum Dry Density (1.55 g cm^{-3})

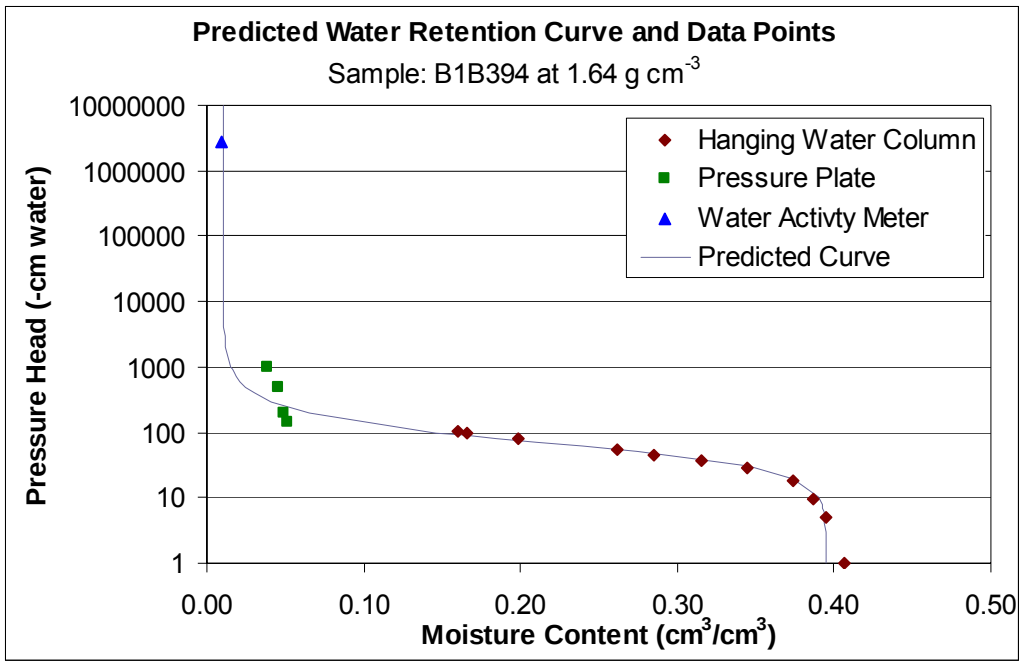

Figure B3. Measured and Fitted Water Retention for ERDF Sample B1B394 at 95 Percent Maximum Dry Density (1.64 g cm^{-3})

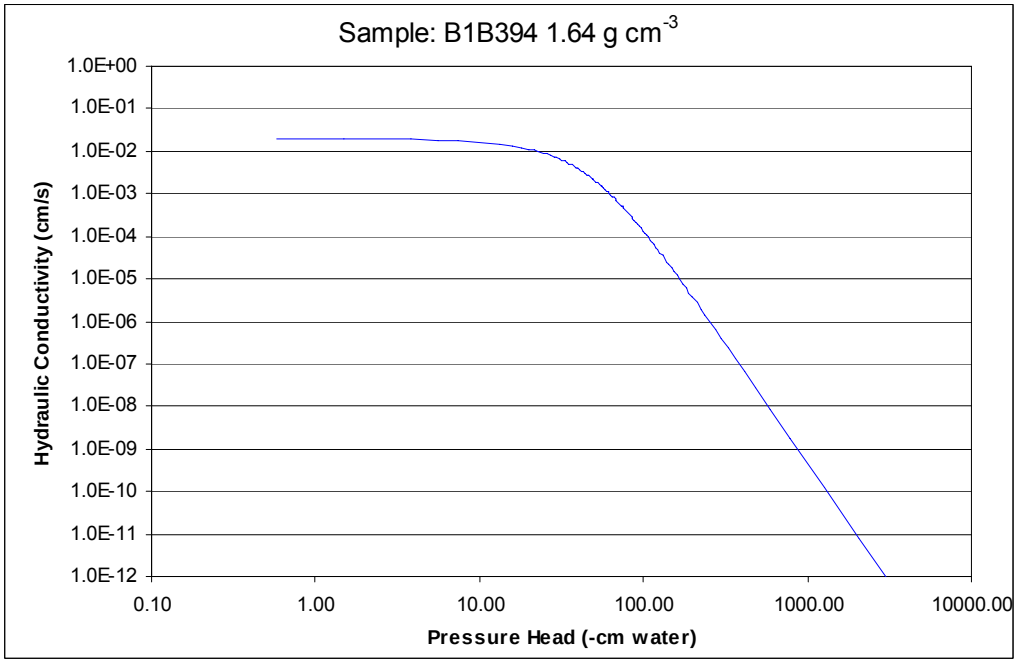

Figure B4. Predicted Hydraulic Conductivity for ERDF Sample B1B394 at 95 Percent Maximum Dry Density (1.64 g cm^{-3})

Table B11. Measured Water Retention for ERDF Sample B1BRD4 at 90 Percent Maximum Dry Density (1.57 g cm^{-3})

Method	Matric Potential ψ (cm)	Water Content θ_v
Hanging Water Column	1.0	0.363
	8.3	0.363
	17.8	0.319
	36.0	0.304
	53.9	0.254
	71.3	0.197
	91.0	0.156
Pressure Plate	146.7	0.050
	195.6	0.038
	488.9	0.036
	977.8	0.028
Water Activity Meter	2480672.7	0.011

Table B12. Measured Water Retention for ERDF Sample B1BRD4 at 95 Percent Maximum Dry Density (1.66 g cm^{-3})

Method	Matric Potential ψ (cm)	Water Content θ_v
Hanging Water Column	1.0	0.386
	9.0	0.356
	18.0	0.338
	36.2	0.270
	53.5	0.214
	72.0	0.175
	90.8	0.145
	108.7	0.130
Pressure Plate	146.7	0.055
	195.6	0.044
	488.9	0.037
	977.8	0.030
Water Activity Meter	2480672.7	0.011

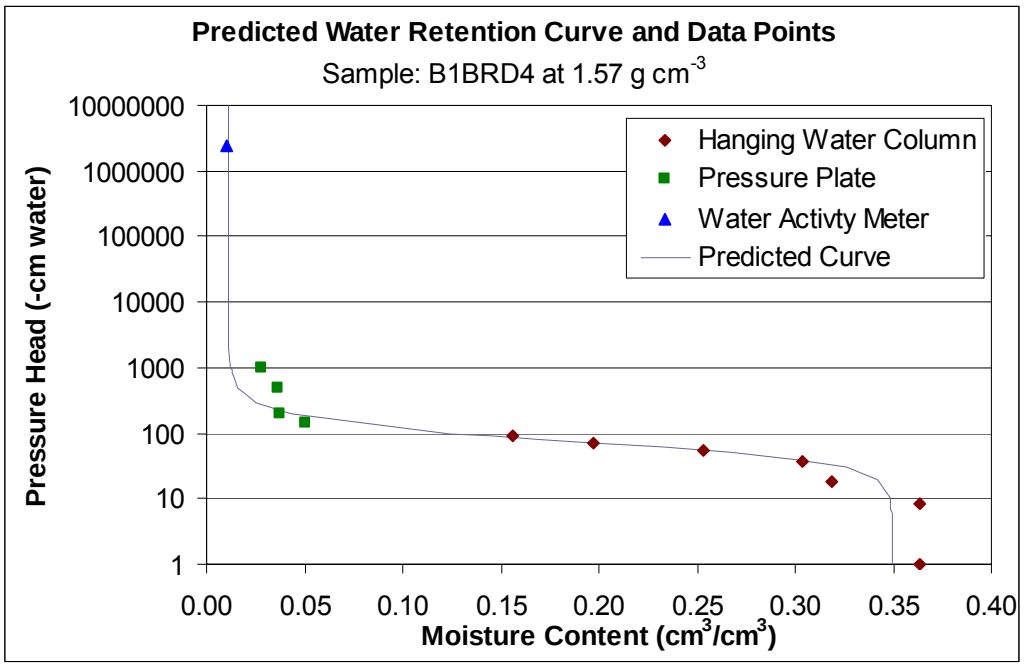

Figure B5. Measured and Fitted Water Retention for ERDF Sample B1BRD4 at 90 Percent Maximum Dry Density (1.57 g cm^{-3})

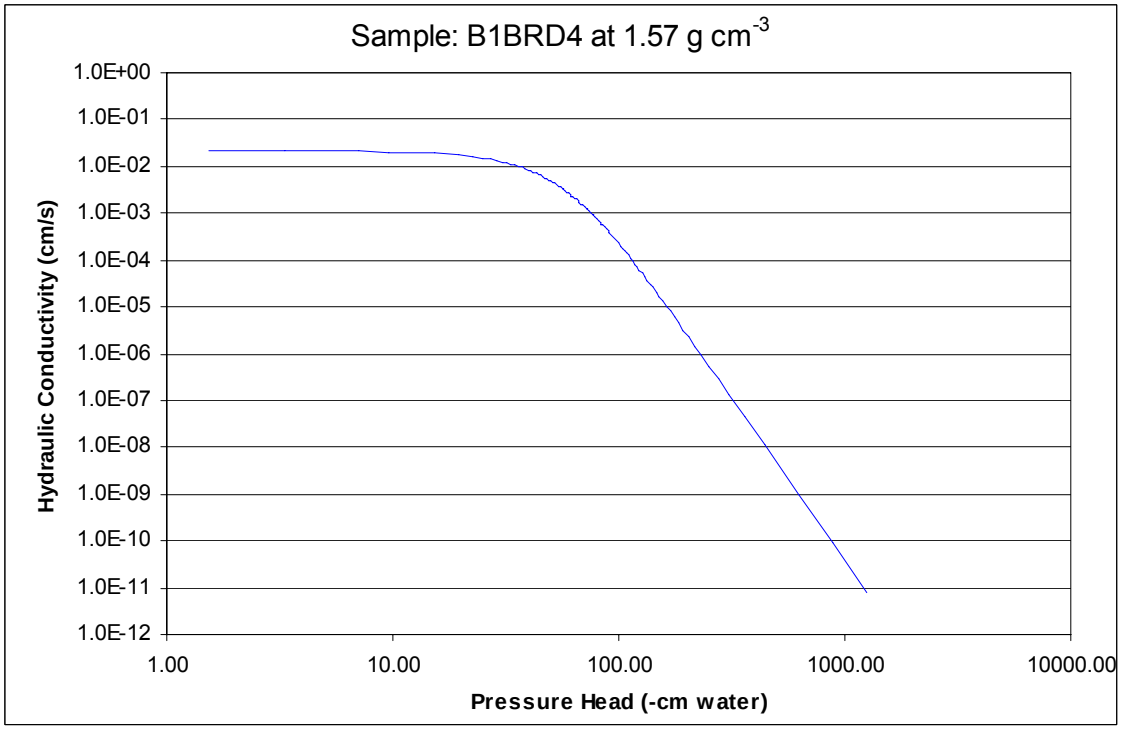

Figure B6. Predicted Hydraulic Conductivity for ERDF Sample B1BRD4 at 90 Percent Maximum Dry Density (1.57 g cm^{-3})

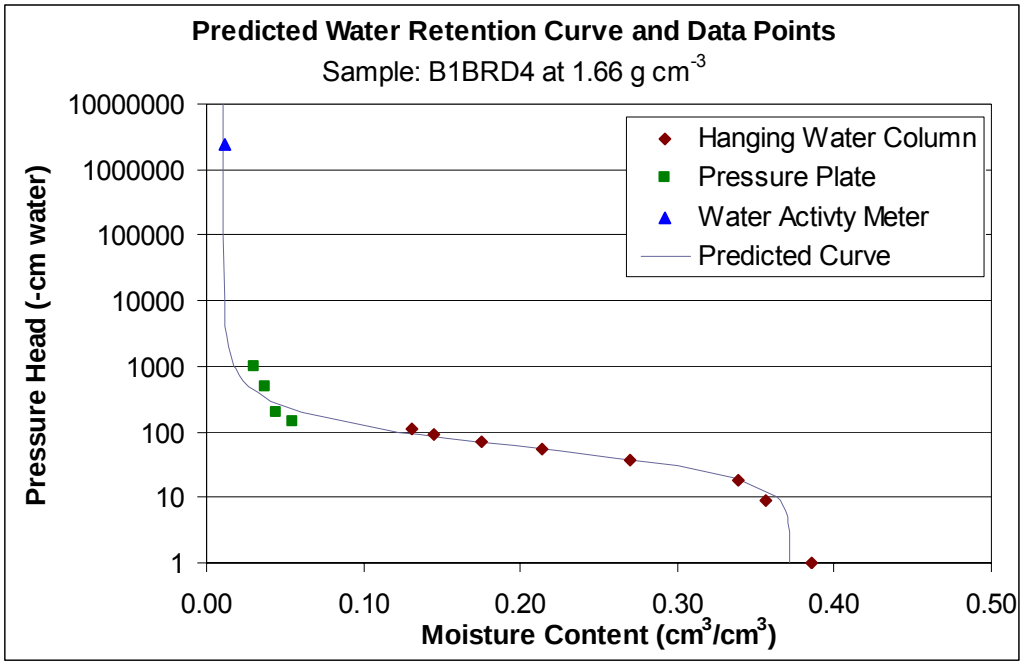

Figure B7. Measured and Fitted Water Retention for ERDF Sample B1BRD4 at 95 Percent Maximum Dry Density (1.66 g cm^{-3})

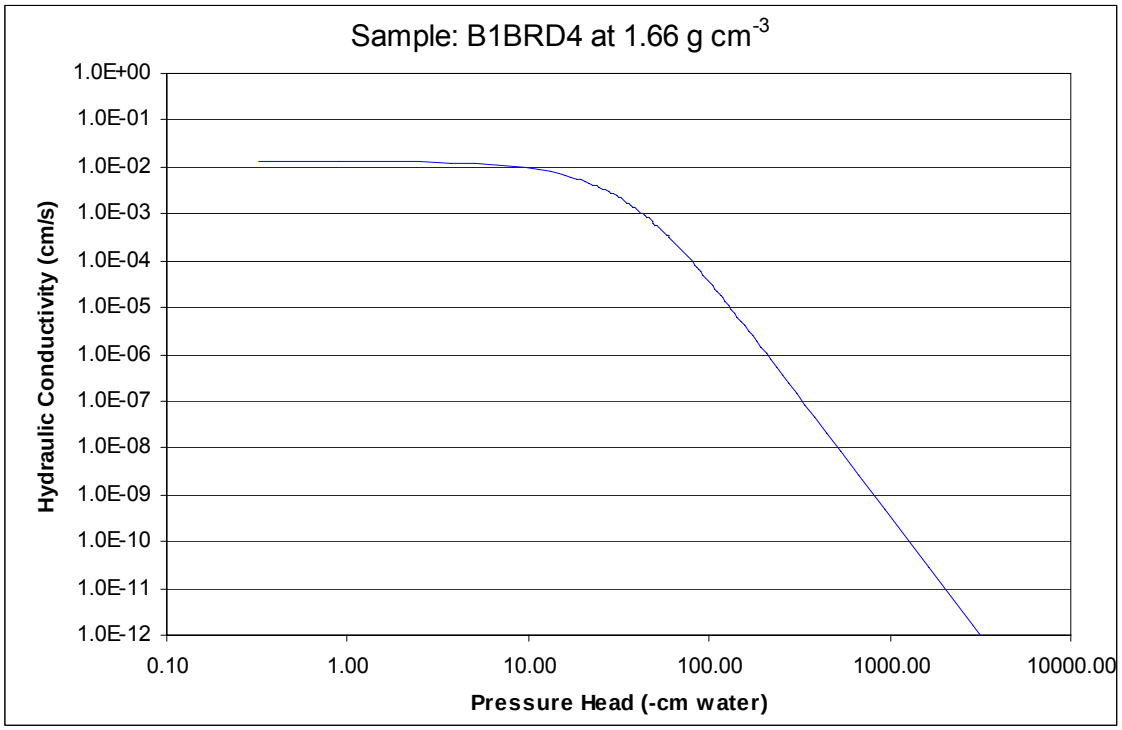

Figure B8. Predicted Hydraulic Conductivity for ERDF Sample B1BRD4 at 95 Percent Maximum Dry Density (1.66 g cm^{-3})